1-1-2011

A novel integrated platform combining atomic force microscopy and fluorescence correlation spectroscopy

Venkatesh Subba Rao
Wayne State University,

A NOVEL INTEGRATED PLATFORM COMBINING ATOMIC FORCE MICROSCOPY AND FLUORESCENCE CORRELATION SPECTROSCOPY

by

VENKATESH SUBBA RAO

DISSERTATION

Submitted to the Graduate School

of Wayne State University,

Detroit, Michigan

in partial fulfillment of the requirements

for the degree of

DOCTOR OF PHILOSOPHY

2011

MAJOR: PHYSICS

Approved by:

_____

Advisor Date

_____

_____

_____

DEDICATION

With humility I wish to dedicate my PhD research, and this thesis to my family, my teachers, my friends, and my country.

ACKNOWLEDGMENTS

I would like to thank my advisor Prof. Peter Hoffmann for all his help and guidance in my research work, and in addition, to the innumerable, fruitful, thought provoking and entertaining discussions on a wide spectrum of topics including but not limited to physics. In my humble opinion, and with my experience of working under different PhD advisors, I would like to mention that he is an ideal advisor, and I consider myself to be fortunate to have had him as my PhD advisor. With humility, I appreciate him for all his support, and encouragement throughout my stay at WSU. I also would like to thank Mrs. Hoffmann, and him for hosting many parties, and for treating my wife and myself as a part of their family.

I would like to thank Prof. Ashis Mukhopadhyay for being more than just a committee member; practically, he was my second advisor. He treated me like his own student, and gave me all the freedom to use his laboratory. I learnt a great deal from him (both on theory and experimentation) through the several interactions. He was available to talk to me whenever I wished. Even when he was on sabbatical out of the country he was kind enough to be in constant touch with me through email and video-chatting, and thus I did not feel his physical absence.

I would like to thank Prof. Ratna Naik, and Prof. Guangzhao Mao (Chemical Engineering and Material Science) to have graciously agreed to be a part of my PhD committee. In my personal experience, Prof. Naik is the best department head I have ever come across in my entire life. She was always helpful, considerate, and supportive - thus made my stay in WSU Physics stress-less, and enjoyable. I thank her and Prof. Vaman Naik for hosting us many times at their home and for all the interesting discussions and thoughtful entertainment.

I would like to thank Prof. Paul Keyes, Prof. Jhy-Jiun Chang, Prof. Segei Voloshin and Prof. Gavin Lawes, from whom I have taken different courses during my stay here. I would like to thank Prof. Voloshin for making me enjoy & like statistical mechanics through his fantastic teaching, and Prof. Chang for making me to see issues/situations (both science and non-science) in different angles through his amazingly insightful and unique teaching methods. Words are not sufficient to describe how much I enjoyed learning from Prof. Keyes' lectures, and innumerable conversations. He was also open, and willing to talk to me any time in his office. Many a times when I got stuck with experimental issues or was waiting for data acquisition, I would go to his office and listen to him. Such encounters were always refreshing. I will surely miss visiting his office, and listening to him once I leave Detroit. I appreciate Prof. Lawes for the Materials and Device characterization course; and also for many discussions on various topics, and for patiently listening to me.

I would like to extend my sincere appreciation to Prof. Boris Nadgorny, Prof. Zhixian Zhou, and Prof. Takeshi Sakamoto for their generosity in allowing me to use their labs freely; and for trusting me and my experimental skills. It made my research life less taxing.

Without the help and assistance of Dr. Mircea Pantea, Dr. George Matei, Dr. Raghava Panguluri and Dr. Sudakar Chandran my research would not have been very smooth or completed on time. Words cannot describe my indebtedness to all of them. I learnt a great deal about instrumentation and materials for them and in addition, I had a wonderful and enjoyable time during the countless social interactions with each one of them, and as a result my perception about life in general has changed. In this regard, I wish to convey my special thanks to Dr. Mircea Pantea for the many illuminating and enjoyable discussions; and for increasing my love

and appetite for reading; and also for gifting many books to me. I will miss talking to him and also miss visiting book stores with him.

I wish to acknowledge the following list of people from WSU community for their timely help, assistance, and interactions during the course of my research and stay, which greatly enhanced my over-all understanding, facilitated smooth going of my graduate life, and made my stay here at WSU, wonderful and enjoyable:

Prof. Giovanni Bonvicini and his family; Prof. Steve Rehse, Dr. Scott Payson, Dr. Alan Sebastian, Mr. Alfredo Gutierrez, Prof. Jagdish Thakur, Prof. Karur Padmanabhan, Prof. Jogindra Wadehra, Dr. Punya Talagala, Dr. Christopher Grabowski, Dr. 'Thambi' Ambesh Dixit, Dr. Sahana Moodakare, Dr. Monica Sharma, Dr. Nagesh Kulkarni, Dr. Anupam Kumar, Prof. Sandro da Rocha (Chemical Engineering), Dr. Elayaraja Muthuswamy (Chemistry), Mr. Fred Pompei, Mr. Alexander Dubrish, Mr. James Barlow, Dr. Adam Lincoln, Mr. Rami Omari, Mrs. Indermeet Kohli, Ms. Laura Gunther, Mr. Andrew Aneese, Dr. Shah Khan (for interesting conversations NWFP and Pakistan), Mr. Jason Esmacher, Mr. Nick Davis (for taking wonderful photos and poster printing), Prof. Sara Tipton (English), Prof. Karen Beningo (Biology) many friends in different WSU departments and all the staff of Physics office.

Finally, I acknowledge the financial support through fellowship and assistantship from Wayne State University – I consider myself privileged to have received them.

INVOCATION

वागर्थाविव संपृक्तौ वागर्थाप्रतिपत्तये
जगतः पितरौ वन्दे पार्वतीपरमेश्वरौ

Vagarthaviva samprktau vagartha pratipattaye
jagatah pitarU vandE pArvatI paramEswaraU

So that I might attain right knowledge, and understanding, of words and their meanings, I worship the parents of the universe, Parvati and Parameswara, who are inseparable like words and their meanings.

- *Raghuvamsa*

எப்பொருள் யார்யார்வாய்க் கேட்பினும் அப்பொருள்
மெய்ப்பொருள் காண்பது அறிவு

EpporuL yaar yaar vaai ketpinum apporuL
meipporuL kaaNbadhaRivu

Whosoever says whatsoever, discerning the truth in them is intelligence/wisdom *(science)*.

- *Thirukural*

असतो मा सद्गमय तमसो मा ज्योतिर्गमय

मृत्योर मा अमृतं गमय ॐ शान्ति शान्ति शान्तिः

Asato maa sad gamaya: Tamaso maa jyotir gamaya:
Mṛityor maa amṛitan gamaya: Om shaanti shaanti shaanti:

Lead me from untruth to truth: Lead me from darkness to light:
Lead me from mortality to immortality: OM peace peace peace:

- *Brihadaranyaka Upanisad*

TABLE OF CONTENTS

LIST OF TABLES

LIST OF FIGURES

Chapter 1

INTRODUCTION

1.1 BACKGROUND

The visible world around us is made of atoms, which in turn combine to make molecules. Thus any system is comprised of discrete entities, and the seemingly continuous nature of systems is only an approximation, which is only valid in the micrometer scale and above. The significance of the discrete nature of any fluid or solid systems is well illustrated by Richard Feynman in "Atoms in Motion"[2]: "If, in some cataclysm, all of scientific knowledge were to be destroyed, and only one sentence passed on to the next generations of creatures, what statement would contain the most information in the fewest words? I believe it is the *atomic hypothesis* (or the atomic fact, or whatever you wish to call it) that *all things are made of atoms — little particles that move around in perpetual motion, attracting each other when they ore a little distance apart, but repelling upon being squeezed into one another*. In that one sentence, you will see, there is an enormous amount of information about the world, if just a little imagination and thinking are applied.*"* Thus it is imperative to realize that for any system the continuum approximation will fail at the molecular or atomic scale. Experimentally, in the case of liquid systems, one way to understand the properties arising from the discrete nature is to study a liquid-solid interface. At the nanoscale near the interface, the discrete nature of the liquid is expected to influence various properties, such as density, viscosity or diffusion constants. Understanding the interfacial properties of liquids is important for the development of nanotechnology, especially for the fields of nano-rheology and nano-tribology, and also for

understanding various mechanisms in biological systems at the molecular level, such as protein folding or the self-assembly of lipid vesicles, which invariably involve liquids. From a technological perspective as well, it is imperative to have a thorough understanding of the properties of liquids at the molecular level. New devices, such as nanofluidic channels or lab-on-a-chip devices involve the transport of small amounts of liquids through nanosized structures. Liquids at the nanoscale can be studied by various types of instruments, such as surface force apparatus (SFA)[3], atomic force microscope (AFM) and fluorescence correlation spectroscope (FCS). SFA and AFM are force based instruments which can be employed to measure forces between two surfaces in close proximity, as well as rheological and tribological properties of thin liquid films of molecular dimension[4]. FCS is a fluorescence based technique that measures the dynamics of a small ensemble of molecules by extracting information from the tiny fluctuations in the fluorescent emissions[5,6].

Atomic Force Microscopy (AFM) and Fluorescence Correlation Spectroscopy (FCS) are complementary techniques. While the former provides high resolution topographical information or force vs. separation measurements (even under the native environment of biological systems), it provides only limited chemical, functional or temporal information. To obtain both spatial and temporal information, an integrated platform of AFM and FCS would be advantageous. A number of groups[7-12] have used combined AFM and FCS systems to investigate various systems. Burns et al. used FCS to investigate the dynamics of domains in a model membrane and correlated them with the AFM topography measurements. Chiantia et al. have reported several studies on the mobility and organization of domains in liquid membranes. Several research groups have used Surface Force Apparatus, AFM, FCS and other optical techniques to investigate the behavior of various liquids confined down to the molecular level [13-17].

In our research group at Wayne State University, we have used a home-built AFM to investigate the nano-mechanics of octamethylcyclotetrasiloxane (OMCTS) [18,19], which is a low-viscosity liquid (~0.02 Poise). OMCTS crystallizes near the room temperature (T_m=17 ^{o}C). Diffusion studies on OMCTS films were performed by Mukhopadhyay et al using FCS [17,20]. Those studies have shown that such liquids layer themselves parallel to the substrates when confined, and their properties (diffusing, viscosity) are very different from those of the liquid in the bulk. Recently our group, in collaboration with Mukhopadhyay et al, has published a paper [4] on the investigation of confined films of liquid tetrakis-2 ethylhexoxy-silane (TEHOS), using combined AFM and FCS measurements. The results from FCS experiments showed the slowing down of diffusion due to confinement and presence of heterogeneous dynamics. AFM results showed oscillation in the mechanical properties of the liquid film, indicating the presence of layering in the confined liquid film.

One problem of this field of research is that different techniques are used to study liquids at the nanoscale. This complicates the comparison of the results to arrive at a uniform understanding of liquid properties at the molecular level. In addition, there are some significant experimental limitations in the earlier studies. For example, Mukhopadhyay et al [16] have studied diffusion of a fluorophore in a confined liquid using SFA, which is used for confining the liquid between two crossed cylinders. In these studies they could not systematically vary the thickness of the confinement, in addition there were stability issues arising from large forces due the large contact area of the confining surfaces.

AFM is now commonly used to study the mechanics of liquid molecules under confinement. AFM can be used to obtain viscoelastic mechanical properties such as the stiffness

and damping coefficient. Such studies are performed to understand the dynamics of the system at the nano scale. However, the AFM measurements are performed on a relatively large number of molecules ($>10^3$-10^5) and with low temporal resolution (~ 1 ms). FCS, on the other hand, has single molecular sensitivity and can be used to study the behavior of single molecules with very high temporal resolution. On the other hand, FCS has low spatial resolution, as the resolution is limited by the size of the laser focus, which is a few micrometers large. Thus FCS, with its ability to probe the fast dynamics of a single molecule, is complimentary to AFM. In this thesis, the successful integration of a newly built AFM with an existing custom-made FCS setup is presented.

1.2 PROJECT DETAILS

As mentioned in the previous section considerable work has been done on confined liquids using SFS, AFM and optical spectroscopy. Although the results are meaningful, the measurements are performed independently and correlations between them are rather difficult. This motivated us to design and build a combined AFM/FCS platform that can serve well the further investigations of nanoconfined liquids.

The thesis research was undertaken with two major goals. The foremost goal was to design and construct a new high sensitive AFM, and to integrate it with an existing inverted microscope based FCS setup, which is available in our collaborator's group (Prof. Mukhopadhyay, Department of Physics and Astronomy, WSU). The second goal was to perform various experiments on confined liquids and selected biological systems. Specific objectives are as follows:

1. Understand the dynamics of the confined liquids as a function of the layer thickness.

2. Investigate the response of the confined liquid for various stimuli, like oscillatory normal load and shear.

In order to achieve the specific goals, using this combined SFM/FCS instrument, it was originally proposed to undertake an experimental study of the dynamics of confined liquids. For this purpose two model liquids OMCTS and TEHOS were to be employed since there has been considerable experiments performed on these two systems. However, due to some instrumental challenges and limitations (§ 4.5) we performed initial experiments on a colloidal system rather than the two model liquids, and hope that the originally proposed studies can be performed in future work after overcoming experimental challenges.

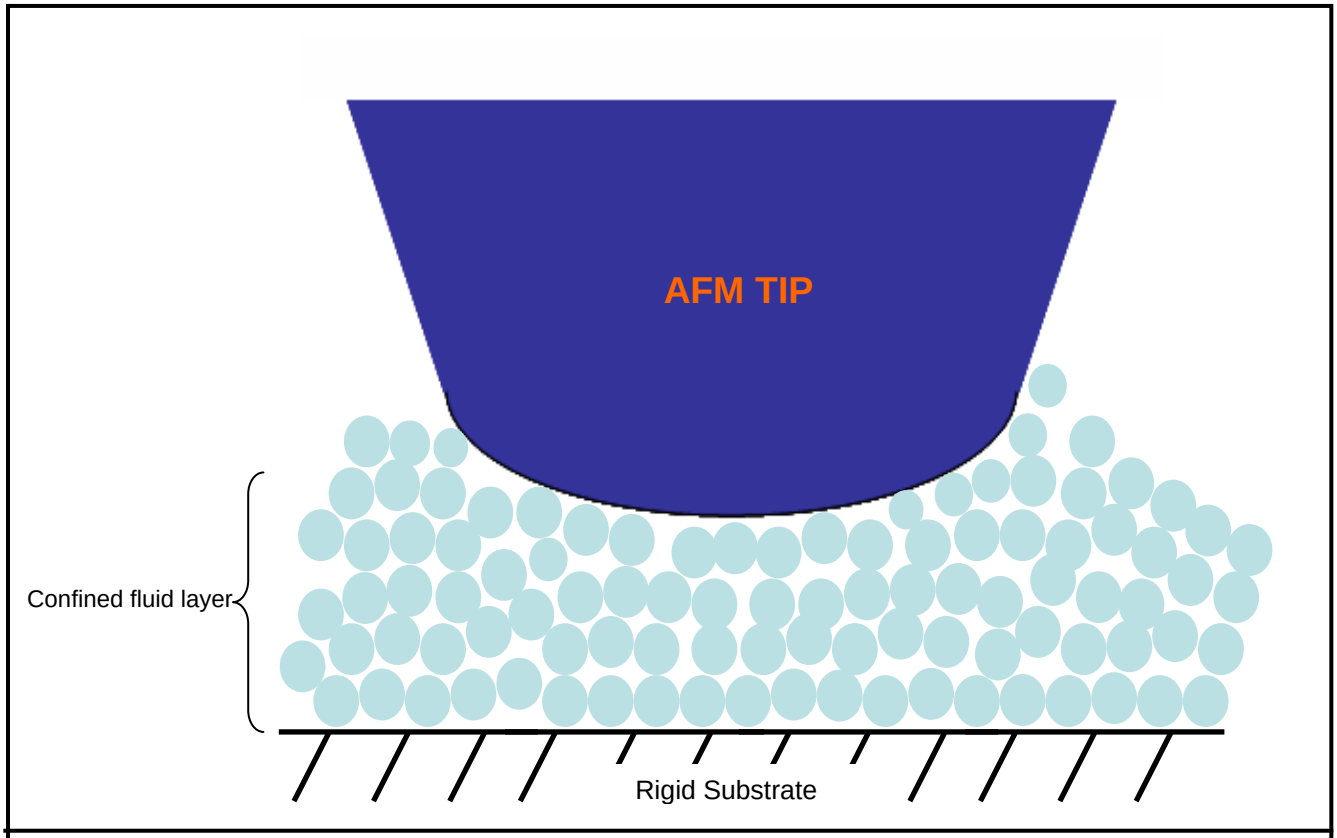

Figure 1.2.1: Schematic of the confined fluid geometry

One of the draw backs of the previous fluorescence spectroscopy experiments on confined liquids, which employed SFA[16,21], is that there was no means to vary the film thickness systematically. In those experiments the fluid layer was obtained by spin-coating technique or by sandwiching the fluid between two cylindrical surfaces (SFA). In the case of spin coating there is no way of precisely controlling the thickness of the confined fluid. In the case of SFA the issue is the large contact area. Large contact area leads to large forces. If these forces are attractive then the system becomes unstable. With our new combined AFM/FCS both these issues are taken care of, as the AFM tip itself forms the top surface (Figure 1.2.1) of the confined fluid. Thus the thickness of the layer can be controlled and the contact area is also not as large as in the case of SFA. This allows us to probe the system in the attractive regime.

Previous FCS work[16,21] performed on OMTCS has shown that the translational diffusion coefficient decreased by 2 orders upon confinement, indicating the formation of structure in the liquid upon confinement. Furthermore, well defined heterogeneity was observed in the autocorrelation function, indicating the presence of multiple diffusion processes. This lead to the hypothesis that there could be different diffusion rates in different layers of the structure. With our combined SFM-FCS setup this hypothesis could be tested by systematically varying the thickness of the confined liquid and measuring diffusion coefficient with FCS.

SA-AFM experiments undertaken previously on confined fluid have clearly shown that there is ordering in the confined fluid (see Fig.11) [4,18,19]. Furthermore it was found that the rate of confinement was the most important parameter controlling the dynamics of the confined liquid[4]. For OMTCS it was found that the confined liquid behaved ‘liquid like’ for approach speeds lower than a critical speed, while the system behaved ‘solid like’ at higher approach speed. Here

the distinction between solid like and liquid was based on whether the system is able to retain or dissipate stress[18]. Based on these experiments it was concluded that the solidification of liquids under confinement is a kinetically induced transformation.

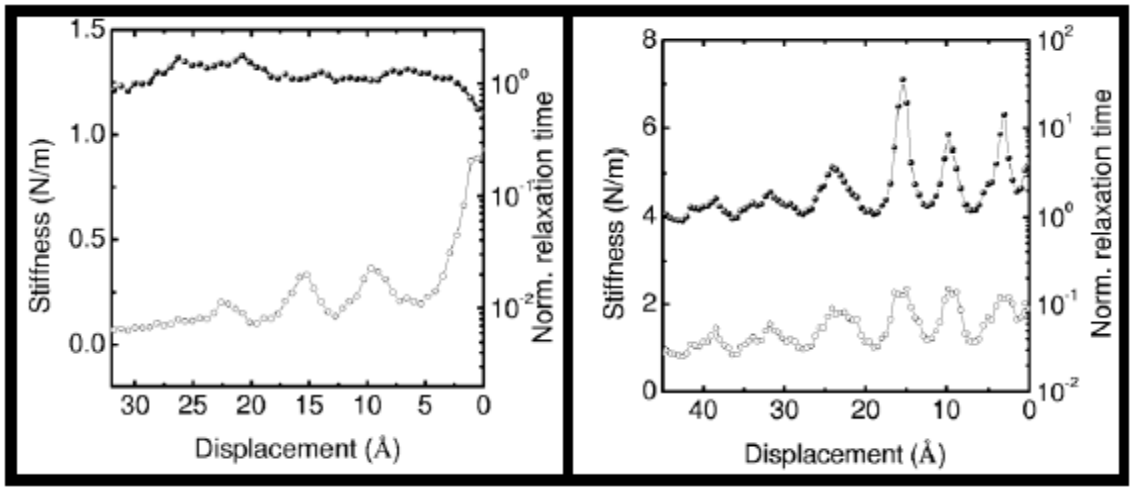

Figure 1.2.2: Stiffness and relaxation measurements using SA-SFM measurements on confined OMTCS[18] for different approach speeds. Left: Speed 3Å/s .Right: Speed 6Å/s.

Similarly the confined liquid has been subjected to an external shear in previous studies in our group[22]. These studies showed that the shear stiffness of the liquid also oscillates commensurate with the molecular layering of the liquid. However, the effect of shear on the diffusion in the confined liquid is unknown. This could be studied by measuring the diffusion coefficient of fluorophores using FCS, while simultaneously shearing the liquid. With this experiment we could understand how shear force changes the dynamical structure and diffusion in the confined fluid. Moreover, with our setup these two stimuli could be applied independently to both the top (AFM tip) and bottom (closed loop scanning stage) surfaces.

In summary, by integrating SFM and FCS into a single experimental platform we are able to perform experiments to correlate the nanomechanical measurements with single molecule diffusional behavior in confined liquids and biological systems.

1.3 THESIS DETAILS

The thesis is organized into five different chapters following this chapter. Chapters two and three are devoted to explaining the two complimentary techniques, AFM and FCS. In chapter two, I describe the various aspects about AFM starting with a brief history. The chapter is divided into three sections, each of which details with the history, working principle, and applications, respectively.

FCS technique is covered in chapter three. In this chapter, I present the details of FCS, a technique that provides information that compliments AFM measurements. This chapter is divided into two sections. In the first a brief background on FCS is presented, which is followed by a discussion on the theory and implementation of FCS technique.

Instrumentation aspects are presented in chapter four. In this chapter, I describe the various pertaining to the design and construction of the combined AFM/FCS platform. The chapter is divided into six sections. In the first section, discussion on the rationale behind integrating AFM with FCS is presented. The second section gives the details of design, construction and implementation of the newly built AFM, which was successfully integrated with an existing custom made FCS setup. In the next section, I elucidate a novel method to coat the end of an optical fiber, which was developed as part of my research[23]. In the fourth section the details of calibration of the various parts of the new AFM are presented. In the penultimate

section, the details of experimental procedures and some of the major challenges are presented. In the final section, I present the limitations of the new integrated platform.

In the penultimate chapter, I describe the different experiments that were performed, and their respective results. This chapter is divided into three sections. The first two sections pertain to nanofluid properties, in bulk and under confinement. The last section describes preliminary experiments and results for an antigen-antibody system.

And in this final chapter, I present a brief summary of my thesis work, and describe directions for future research with the novel integrated platform constructed during this thesis work. Some of the proposed future experiments need to be performed to fully understand and explain the intriguing results presented in the previous chapter.

Chapter 2

ATOMIC FORCE MICROSCOPE

In this chapter, I describe the various aspects of AFM starting with a brief history, followed by the working principle, and applications of AFM.

2.1 A BRIEF HISTORY

The complexities and heterogeneities of surfaces are very aptly illustrated by a famous quote by the Austrian Nobel-prize winning physicist Wolfgang Pauli: "God made the bulk, but surfaces were invented by the devil". Surfaces are complicated and to study them sophisticated instruments are needed. AFM belongs to a family of microscopes called Scanning Probe Microscopes (SPM), which are now widely employed to study surfaces at nanoscale, at which heterogeneity of the surfaces may have significant influence on various properties. In this family, Scanning Tunneling Microscope (STM) was the first instrument to be invented, in 1981, by Gerd Binnig and Heinrich Rohrer[24]; for which they received the Noble prize in 1986. Prior to the invention of STM, two different kinds of instruments, namely stylus profilometer and field-emission microscope, were employed to study the local surface properties [Rohrer Noble lecture]. However, such instruments had limitations. Profilometers are unable to provide information at the nano or atomic scale. Field emission microscope gives atomic resolution. However, it is restricted to study sharp tips of clean samples under ultra high vacuum (UHV) condition. STM was the first instrument to 'visualize' the 3D topography of surfaces of many different materials at the atomic scale in real space. In addition, different properties, for example electrical conductivity, of surfaces can also be obtained at the atomic scale. STM utilizes the

principle of quantum tunneling to perform topographical imaging at the nanoscale of conducting surfaces.

Early on, the significant role played by the forces between the probe and the sample during STM operation was realized by the inventors. This motivated a few years later, in 1985, the invention of the AFM by Binnig, Quate and Gerber[25]. A photo of the first AFM, which is at the London Science Museum, is shown in Figure 2.1.1 In AFM the inventors combined the principles of STM and stylus profilometer[25,26]. Unlike its predecessor STM, AFM can be employed to study insulators. This is possible because AFM measures forces, which are present at any surface, conducting or non-conducting. The force is measured through the bending of a cantilever spring to which a sharp tip is attached, which interacts with the surface.

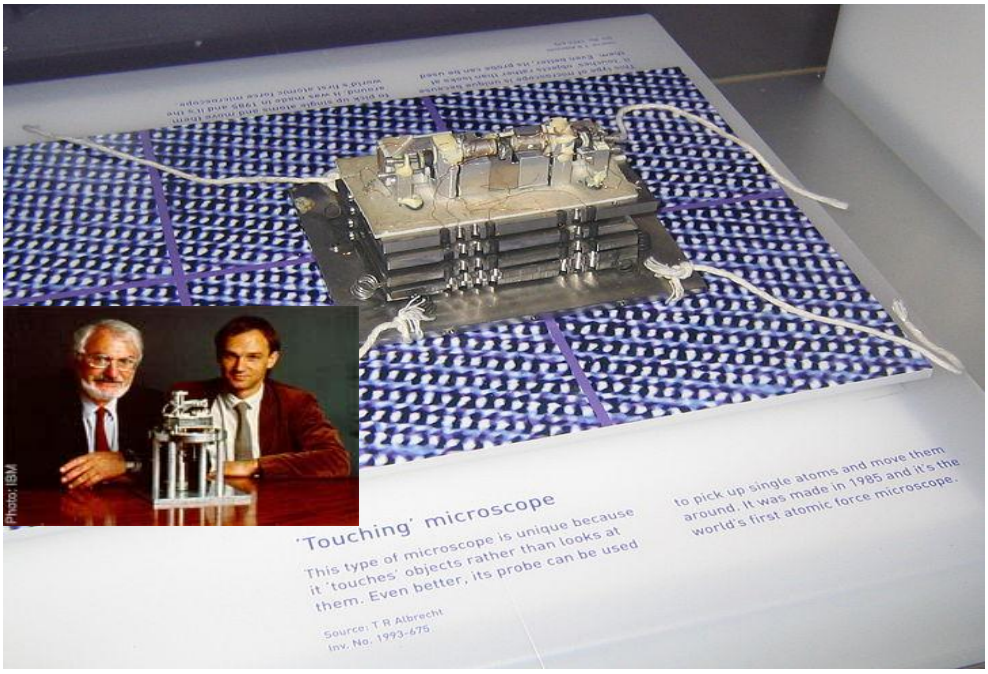

Figure 2.1.1: World's first AFM on display in London Science Museum [Courtesy of Wikipedia reproduced with permission]. Inset: STM with its investors Heinrich Rohrer (left) and Gerd Binnig [Courtesy of IBM Research- Zurich. Unauthorized use not permitted]

2.2 FUNDAMENTALS AND WORKING PRINCIPLES

The basic principle of operation of AFM is schematically shown below in Figure 2.2.1. Shown in this schematic is an AFM that utilizes a laser detection system, which is commonly employed in commercially available AFM.

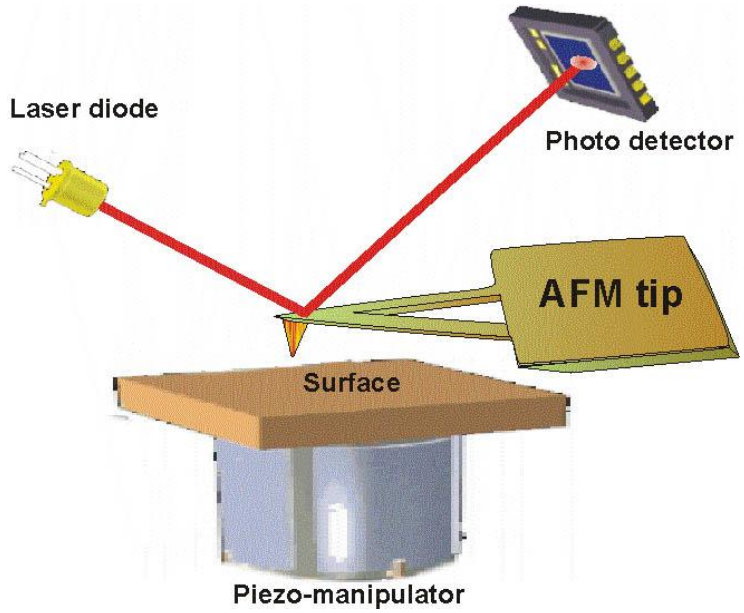

Figure 2.2.1: Schematic illustration of AFM working principle (courtesy of Dr. Sokolov, Clarkson University, Potsdam, NY)

The heart of the AFM is a sharp tip which is integrated with a flexible cantilever. As the distance between the tip and sample is reduced, the tip interacts with the sample due to intermolecular, interfacial or surface forces. As a result of this interaction, the flexible cantilever bends. Thus the cantilever acts as a "force transducer". In the above setup, the cantilever bending is measured by reflecting a laser beam off its top side (that is coated with a high reflectivity film), onto a photo detector. The cantilever bending is determined from a shift in the position of the deflected laser spot on the photodiode.

In order to enhance measurement sensitivity, other detecting techniques[26] have also been employed, in addition to the above mentioned optical detection scheme. One such technique uses an optical interferometer[27]. The working principle is schematically shown in Fig.2.2.2. This is the method we are using in the proposed study.

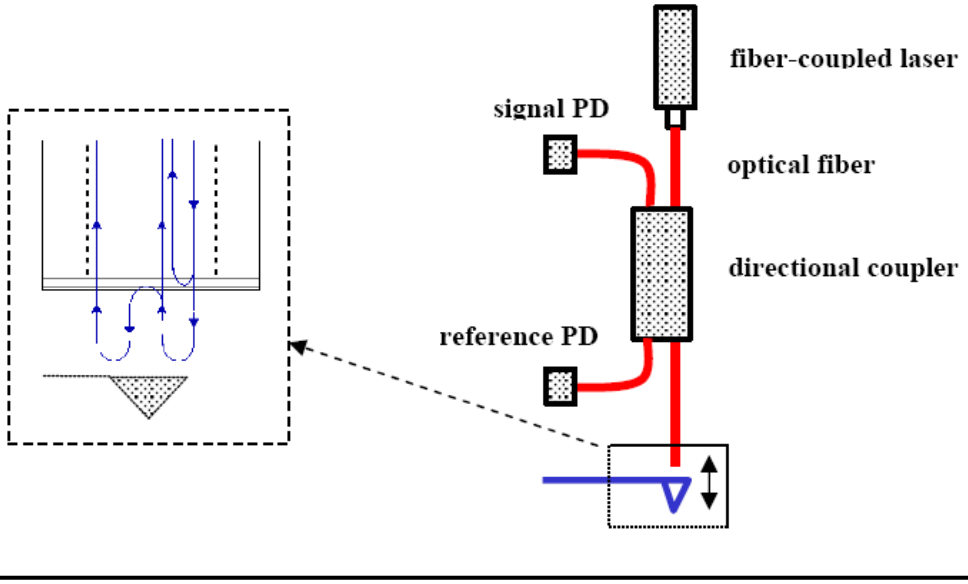

Figure 2.2.2: Interferometric detection system

2.2.1 AFM OPERATIONAL MODES

AFM can be fundamentally operated in two different modes, namely static mode and dynamic mode. The modes are explained in detail in two different sections, which are presented below.

2.2.1.1 Static (DC) or "contact" mode

In this mode the tip is moved vertically towards the sample and the corresponding deflection of the cantilever is measured. During this vertical motion at each point the equilibrium deflection (response of the cantilever to the tip-sample interaction) of the cantilever is recorded.

Similarly, the deflection is recorded while retracting the tip. Treating the cantilever as a Hookian spring, we can trivially obtain the tip–sample interaction force by multiplying the cantilever (equilibrium) deflection with its spring constant. This way force-distance curves can be obtained.

The topographical image of a sample is obtained by monitoring the deflection of the cantilever as tip scans the sample. The topographical data can be obtained in two ways, namely constant- force mode or constant-height mode. In the former the deflection (hence the force) of the cantilever is set to a fixed value while in the latter the extension of the piezo is fixed. In the case of constant–force mode a feedback circuit moves the sample (or tip) up and down according to the sample features, in order to keep the deflection and hence the tip-sample force constant. The topographical data is generated from the voltage which the feedback circuit applies to the piezo that moves the sample (or tip), which can be calibrated to give the topography in terms of suitable units of distance (typically nanometers). In the case of constant-height mode the topographical data is generated from changes in the cantilever's deflection as the tip is moved in a straight line above the sample. Due to the fact that the tip is in "contact" with the sample, high frictional forces (drag) can be detrimental to both the tip and the sample (especially soft ones), which can ultimately be damaged during scanning.

2.2.1.2 Dynamic (AC) or "Intermittent Contact" mode

In this mode the cantilever is vibrated vertically by applying a sinusoidal voltage to the (dither) piezo attached the cantilever. The response of the cantilever (amplitude, phase or frequency of oscillation) as a result of the tip–sample interaction is measured. Unlike the contact mode, the tip-sample interaction is not trivially obtained (see the next section). The topographical data is generated from monitoring the amplitude of oscillations. In this case the

feedback circuits moves the sample (or tip) up or down in order to fix the amplitude at a constant value as specified by the user. Since the tip is in "contact" with the sample only for a small fraction of time during the vibration, the issue of large force (as encountered in DC mode) may be reduced. As a result, this method may be less damaging to softer samples. In the next section a special type of AFM, namely small amplitude AFM, which is operated in a AC mode is present. In this research we have employed this type of AFM.

2.2.2 SMALL AMPLITUDE ATOMIC FORCE MICROSCOPE:

Typically during the AC mode of operation, the cantilever is oscillated near its free resonant frequency in order to enhance its sensitivity. This often results in "large" amplitudes (10-100 nm) that introduce non-linear effects in the measurements. In order to linearize the measurements, in Small Amplitude Atomic Force Microscope (SA-AFM) the cantilever is oscillated below the resonant frequency at sub-Angstrom amplitudes[28,29].

2.2.2.1 Theory of SA-AFM

Since the tip–sample interaction gradient is essentially constant over the range of sufficiently small cantilever amplitudes, the interaction can be modeled as a damped driven harmonic oscillator[1], as illustrated schematically in Figure 2.2.3.

The equation of motion for the displacement of the tip-sample system in the small amplitude limit is given below.

$$m^* \ddot{z} = -C_{ts} \dot{z} - k_{ts} z + k_L (z_0 - z) \qquad (2.2.1)$$

Here, m* denotes the effective mass of the vibrating cantilever, and C_{ts} is the total damping coefficient of cantilever and tip-sample system. z_0 and z stand for the displacements of the fixed end and the free end of the cantilever. k_L and k_{ts} stands for the spring constants of cantilever and tip-sample system.

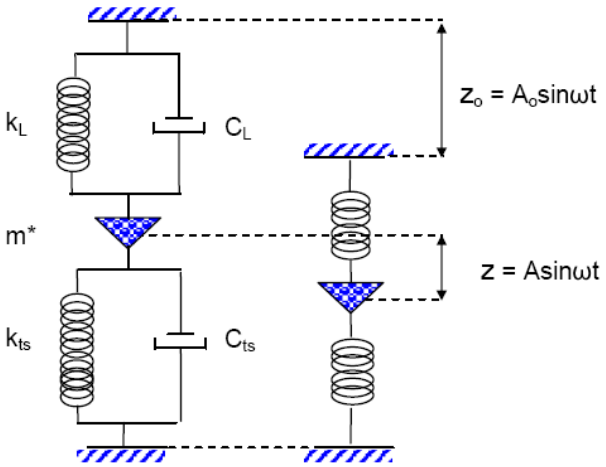

Figure 2.2.3: Model for cantilever-tip-sample system

For a sinusoidally driven cantilever (with frequency ω and amplitude A_o), we get from above

$$m^*\ddot{z} + C_{ts}\dot{z} + (k_L + k_{ts})z = k_L A_0 e^{i\omega t} \tag{2.2.2}$$

Using the harmonic solution, $z = Ae^{i\omega t}$ the magnitude and the phase of complex amplitude A are given by

$$|A| = \frac{k_L A_0}{\left[(k_L + k_{ts})^2\left(1 - \frac{\omega^2}{\omega_0^{\,2}}\right)^2 + (C_{ts}\omega)^2\right]^{1/2}} \tag{2.2.3}$$

$$\tan\phi = \frac{\omega C_{ts}}{\left(k_L + k_{ts}\right)\left(1 - \frac{\omega^2}{\omega_0{}^2}\right)} \tag{2.2.4}$$

Here, $\omega_0 \equiv \sqrt{\frac{\left(k_L + k_{ts}\right)}{m*}}$, is the 'natural' frequency of the cantilever in the tip-sample force field. Using these equations, the damping coefficient C_{ts} and interaction stiffness k_{ts}, can be, in principle, calculated from the amplitude and the phase of the cantilver, which are the experimental observables. When the cantilever is vibrated far below the resonance frequency and the oscillations are kept within the small amplitude range (<1 Å), the interaction stiffness k_{ts} is given by

$$k_{ts} = k_L\left(\frac{A_o \cos\phi}{|A|\left(1 - \frac{\omega^2}{\omega_0^2}\right)} - 1\right) \tag{2.2.5}$$

For small ϕ ($\phi \approx 0$), the damping coefficient, C_{ts}**,** and interaction stiffness, $k_{ts,}$ become,

$$k_{ts} = k_L\left(\frac{A_o}{|A|} - 1\right) \text{ and } C_{ts} = k_L\left(\frac{A_o}{|A|\omega}\sin\phi\right) \tag{2.2.6}$$

In order to avoid the so-called snap-to-contact effect, sufficiently high stiffness cantilevers are usually employed. Off-resonance operation also proved to be efficient in minimizing the thermal noise that can become significant for very small amplitude vibrations since most of it is centered

around the resonance. Off-resonance operation with small amplitude of oscillation requires a high sensitive detection mechanism, which in our AFM is provided by an interferometric detection system.

2.3 APPLICATIONS

AFM has the required sensitivity and resolution to perform 3D topological, and force spectroscopic measurements at nano and even atomic scale. Originally, AFM was employed by the physics and surface-science communities to study properties at the nano-scale. However, due to the inherent simplicity in design, operation and robustness, AFM is presently applied in various field including but not limited to biological sciences. In addition, AFM is incorporated or integrated with various other instruments, such as electron microscopes, confocal microscopes, Raman spectroscopes, and many more. It is not an exaggeration to say that AFM has become an indispensible tool in nanoscale or nanotechnology research. In the present work the first successful integration of AFM with a fluorescence correlation spectroscope is presented. In order to illustrate the versatility and power of AFM, a brief list of selected applications of AFM in three different sciences are presented. The applications presented are by no means complete or exhaustive.

2.3.1 PHYSICAL SCIENCES

AFM can be used with practically all different types of materials, such as conductors, insulators, semiconductors, composites etc. With appropriate modifications it can be used to study magnetic materials as well. AFM is used to visualize, at the nanoscale, the topography of all various types of materials including heterogeneous and anisotropic materials.

In addition to direct imaging, high sensitivity AFMs are employed to manipulate groups of atoms or even individual atoms. AFM, when used for force spectroscopy, has the capability to measure various types of inter-atomic or inter-molecular forces, including but not limited to van der Waals and electrostatic forces. From force spectroscopy, the various properties like bulk modulus, cohesion/adhesion, electrical and magnetic properties, and interfacial properties of liquids, can be studied at the nanoscale[26,30-32].

Using electric force spectroscopy, electrostatic forces at distances of less than 1nm as well as over a large tip-sample distances have been measured[33,34]. Measurement of capacitance as low as 10^{-19}F has been achieved[34,35]. Localized charges deposited on insulators with sensitivity as low as few electrons, and ferroelectric domains have been imaged[34-39]. Other electrical measurements like surface conductance of metals, contact potentials, impurity dopant concentration, and potential across junctions have been by reported various groups[40-47]. Similar to electrostatic measurements, magnetic interactions have been observed widely[48-50]. From early 1990's, surface topography with atomic resolution on different materials have been demonstrated, and in addition, measurements of atomic scale friction have been achieved[51-53]. Thus it is not an exaggeration to say that AFM has been an indispensible instrument for surface science.

2.3.2 CHEMICAL SCIENCES

AFM has the capabilities to observe, at the molecular scale and in-situ, any morphological changes that may occur due to a chemical reaction[54-60]. Ikemiya et al reported the observation of the formation of oxide film on Cu(100) and Cu (111) surfaces[58]. Using AFM, in situ direct observation of a lead electrode surface during chemical reaction with sulfuric acid was reported Yamaguchi et al[59]. AFM observations revealed that chemically formed lead sulfate was

clearly different in appearance from electrochemically formed lead sulfate. Such studies can be crucial in understanding chemical deposition that are of interest to both fundamental and applied research. In addition to deposition, other chemical processes such as corrosion, dissolution can also be monitored a using AFM[61]. With appropriate modification of the AFM probe, atoms and molecules can be manipulated, and hence local chemical reactions can be performed[62,63]. Topological imaging and or force spectroscope can be performed to monitor and quantify various process including but not limited to, self-assembly, electrochemical reactions and phase change[64-72].

2.3.3 BIOLOGICAL SCIENCES

The simple nature of the design of AFM renders it possible to be used in vacuum, ambient condition, and in liquid environment. The operation in liquid environment coupled with high resolution has made AFM a very attractive and useful tool for various applications in life science[31,73-80]. Unlike other electron microscopes, with the exception of sophisticated environmental scanning electron microscope, AFM operation in liquid or physiological condition provides information that is directly relevant to biological systems in their natural state. In addition, sample preparation in AFM is straight-forward and does not require any special sample treatment, like staining or fixing. With a signal-to-noise ratio better than any optical microscopic technique and with a spatial resolution approaching molecular dimensions, AFM is employed to visualize supra-molecular assemblies, and to characterize structure and functional conformation of cellular components in the native state[75,76,81-83]. AFM imaging of living cells has revealed specific structures, such as parts of the cytoskeleton, which were not observed by SEM[84]. In addition, membrane structures, such as ruffles, lamellipodia, microspikes and microvilli, could

be observed in the AFM images of living cells[84]. In the force spectroscopy mode, AFM detects inter-protein or inter-cell interactions at molecular resolution and from such interactions one can estimate various properties like local elasticity, chemical groups, and receptor sites of live cells[85,86]. From force spectroscopy, energy landscapes of bio-molecular reactions, kinetics, lifetimes, elasticity, and free energy can be determined[86-94]. Combining imaging with force spectroscopy modes in AFM, one can perform recognition imaging, which allows the localization of single receptors. In addition, AFM gives the user the ability for manipulation of the bio-molecules of cellular membranes[95-98].

Chapter 3

FLUORESCENCE CORRELATION SPECTROSCOPY

In this chapter, I present the details of FCS. Information obtained from FCS compliments the results of AFM measurements. This chapter is divided into two sections. First, a brief background on FCS is presented, which is followed by a discussion on the theory and implementation of the FCS technique.

3.1 BACKGROUND

As the name suggests, Fluorescence Correlation Spectroscopy (FCS) is a spectroscopy based on fluorescence phenomenon. In fluorescence spectroscopy or any other kinds of spectroscopy the average intensity is the quantity of interest, which is monitored as a function of any system variables. However, in FCS, we are not interested in average intensity, but rather in the fluctuation in the fluorescence intensity from the average. These fluctuations contain information about the dynamics of the system under study. FCS was first developed[99-101] in the early 70's to measure the diffusion and chemical dynamics of DNA-drug intercalation. Later, FCS was applied to various other processes, such as inter-molecular or intra-molecular rate constants[102].

In general, even under chemical or thermodynamic equilibrium, any fluorescence signal contains small temporal fluctuations. These fluctuations may be due to various parameters associated with the fluorophore or the fluorescently labeled system under investigation. Variations in local concentrations, mobility coefficients, rate constants of inter- or intra

molecular interactions are some of the parameters responsible for the fluctuations in the fluorescence intensity. In principle, some or all of the above mentioned parameters can be determined from analyzing the fluorescence signal. One way is to perform temporal autocorrelation (measure of self similarity) of the fluorescence signal. FCS can be considered similar to dynamic light scattering (DLS) with fluorescence emission. However, there are a few major differences and each has its own unique advantages and disadvantages. DLS involves elastic or quasi-elastic scattering, while FCS involves fluorescence emission, which is inherently an inelastic scattering process. In the case of FCS, excitation could occur with the absorption of one or more photons. In addition, unlike DLS, FCS can in principle be performed with multiple beams. The different beams could be of same or different wavelengths. In such a situation, cross-correlation with two different beams needs to be performed. However, DLS has the advantage of having the capability to perform wave vector (q) dependent measurements. From the q-dependent measurements, anisotropy and polydispersity of the colloidal suspensions could be determined. With regards to the sensitivity, FCS has the ability to detect single particles and thus allows experiments with very low concentration in the nano-molar range. DLS measurements, on the other hand, require much higher concentration. Such features of FCS render it more versatile than DLS. In the next section, the theory and implementation of FCS is presented.

3.2 THEORY AND PRACTICE

FCS is based on analyzing the fluctuations of the fluorescence emission from an open volume, which is formed by tightly focusing a laser beam by a microscope objective. In FCS, the dynamics of the system under observation is obtained from estimating the auto-

correlation of the fluctuations of the fluorescent intensity. The autocorrelation function (Equation 3.2.1) gives the measure of interdependence of values of the random signal at two instants separated by some time interval.

$$G(\tau) = \frac{\langle \delta I(t) \delta I(t+\tau) \rangle}{\langle I(t) \rangle^2} \tag{3.2.1}$$

Here, I(t) is the observed fluorescent intensity and δI(t) is the fluctuation in the fluorescent intensity, as defined by Equation 3.2.2, given below:

$$\delta I(t) \equiv I(t) - \langle I(t) \rangle \tag{3.2.2}$$

In equation (3.2.1), the autocorrelation is normalized by dividing by the square of the average intensity, which also renders it dimensionless.

The instantaneous fluorescent intensity for single photon absorption depends on various parameters, and phenomenologically is given by the equation below:

$$I(t) = \int_V \kappa \cdot I_{ex}(\vec{r}) \cdot S(\vec{r}) \cdot [\sigma(\vec{r},t) \cdot q(\vec{r},t) \cdot C(\vec{r},t)] dV \tag{3.2.3}$$

Here, V is the volume, κ is the overall detection efficiency; I_{ex} is the spatial distribution of a excitation radiation; S is the spatial distribution of the transfer function of the optical system; σ is the molecular absorption cross-section; q is the quantum yield; and C is the concentration of the fluorophore. In general, for fixed optics the last three parameters depend on time and space. Fluctuation in any one of these parameters leads to changes in the intensity.

Let us consider the simplest experimental situation where the fluctuation in fluorescent intensity is solely due to concentration fluctuations, which may occur due to chemical reaction, diffusion or mass transport. Under thermal equilibrium, concentration fluctuations in the focal volume occur due to diffusion (thermal motion). In this thesis work, we will consider such a scenario as all the experiments are performed under thermal equilibrium. In the case of diffusion, the concentration fluctuation satisfies Fick's law as given below:

$$\frac{\partial[\delta C(\vec{r},t)]}{\partial t} = D\nabla^2[\delta C(\vec{r},t)] \tag{3.2.4}$$

Here, D is the diffusion coefficient.

For the spatial distribution of the laser intensity in the focus, we assume a Gaussian model:

$$W(\vec{r}) = e^{-2\frac{x^2+y^2}{\omega_0^2}}.e^{-2\frac{z^2}{z_0^2}} \tag{3.2.5}$$

Here, ω_0 is the (half) width of the laser focus in lateral direction, Z_0 is the laser beam (half) length in the vertical (axial) direction.

In combination with Equations 3.2.1, 3.2.3, & 3.2.4, and using Green's functions, an analytical expression for the autocorrelation for different situations can be obtained [ref]. For example, the autocorrelation function for the case of free 3D diffusion is given by Equation 3.2.6.

$$G(\tau) = \frac{G(0)}{(1+4D\tau/\omega_0^2)(1+4D\tau/z_0^2)^{1/2}} \tag{3.2.6}$$

Here, τ is the lag time. The laser beam dimensions for a given optics are fixed, and they can be experimentally determined using rhodamine 6G (Rh6G), a fluorescent dye with D = 280 $\mu m^2/s$ at room temperature in aqueous solution

The absolute value of the auto-correlation at the start [G(0)] depends inversely on number (N) of fluorescent dyes in the measurement volume. From Equation 3.2.1, G(0) is given by

$$G(0) = \frac{\langle \delta I(t)^2 \rangle}{\langle I(t) \rangle^2} = \frac{\langle (I(t) - \langle I(t) \rangle)^2 \rangle}{\langle I(t) \rangle^2} \tag{3.2.7}$$

The numerator is the variance and denominator is the square of the mean of the intensity, which is directly proportional to N. Thus Equation 3.2.7 becomes:

$$G(0) \sim \frac{\langle (N - \langle N \rangle)^2 \rangle}{\langle N \rangle^2} \tag{3.2.8}$$

Since FCS employs very low concentration of dyes it is valid to assume a Poissonian distribution for its number. For Poisson distribution variance is equal to mean. Hence we get:

$$G(0) \sim \frac{1}{\langle N \rangle} \tag{3.2.9}$$

Thus from single FCS measurement we can estimate both the diffusion coefficient and concentration of the dynes.

In Figure 3.2.1, the plots of the model of autocorrelation function for various processes are shown. Analytical expressions can be derived for all the cases shown in Figure 3.2.1[103,104]. In addition, such expressions can be easily modified if more than one diffusing species is present in

the system under study, and FCS has the required specificity to distinguish the different species. The expression for autocorrelation function in Equation 3.2.6 was derived assuming single

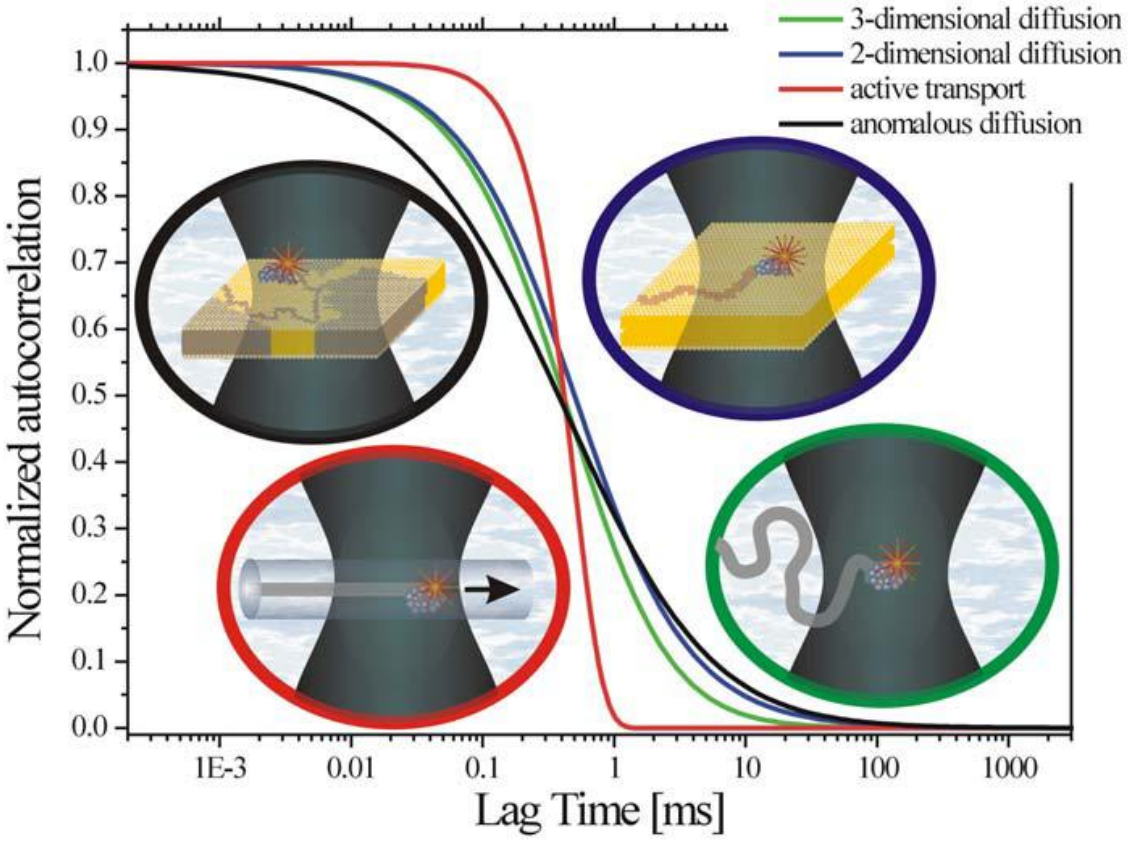

Figure 3.2.1: Model autocorrelation functions for various processes [Courtesy of Prof. Petra Schwille, Biotechnological Center of the TU Dresden, Germany]

As an example, Equation 3.2.10 gives the autocorrelation function for a 3D free diffusion for two photon excitation.

$$G(\tau) = \frac{G(0)}{(1+8D\tau/\omega_0^2)(1+8D\tau/z_0^2)^{1/2}} \qquad 3.2.10$$

In the mid 1990s, two decades after introduction of FCS, Enrico Gratton's group first demonstrated the application of two-photon excitation to FCS[105]. In that work, the authors successfully measured the translational diffusion in the cytoplasm of cells, in addition to measurements of diffusion coefficients for particles of different sizes in bulk solution. Similar to confocal microscopy, two- photon FCS has depth resolution, however it excites a very small volume (of the order of femto liter) in 3D without the presence of emission pinholes. The absorption cross-sections for two-photon process are generally very small and hence it requires intense light for such excitations. Sufficiently high intensity needed for the excitations occurs only in a small volume around the focus. Therefore in two-photon FCS the smaller excitation volume is naturally obtained without pinholes. In addition, there are other advantages of two-photon FCS over its single-photon counterpart. Absorption of the laser is localized to the focal volume, and as a result, damages, if any, would be confined to a very small volume of the sample. This feature of the technique is desirable when working with biological systems, which may be more sensitive to photo damage. Another advantage arises from the fact that the emitted photons are of lower wavelength than incident ones. For example, an 800 nm photon would excite transitions at 400 nm and emission would occur around 500nm. Thus the fluorescence emission is well separated from elastically scattered light. Because of this large separation, the back scattered light is easy to filter out. In this thesis work, two-photon FCS is employed and in the next paragraph the details of the experimental implementation are presented.

Figure 3.2.2 schematically presents the experimental realization of FCS, which is employed in this work. FCS experiments were performed by a two-photon excitation of fluorescence[106]. A femtosecond Ti-sapphire laser (Mai Tai, Spectra-Physics) generates 800 nm wavelength laser pulses of width 100fs at a repetition rate of 80 MHz. The excitation power at

the sample was kept less than 1 mW to avoid dye photo bleaching and heating of the sample. The power of laser beam was changed with neutral density filters. A Zeiss inverted microscope (Axiovert S200TV, Carl Zeiss) served as the optical platform for the experiment. The laser beam was passed through an objective lens. In order to obtain better focusing the objective needs be back-filled with an expanded beam. However, the laser beam is small (~ 3mm) and hence it needs to be expanded. This was achieved with the help of a beam expander, which is placed in the laser path before it enters the microscope. Two different objectives were employed, 63X, NA 0.75, infinity corrected or oil immersion, 100×, NA 1.2. The laser is tightly focused resulting in a small excitation volume (~ femtoliter) within the sample solution. Fluorescence emission is collected through the same objective and detected by a pair of single-photon counting modules (Hamamatsu). The output from the photo multiplier tube (PMT) is recorded and analyzed by an integrated FCS data acquisition system (ISS, IL). By employing two PMTs, cross-correlation of the signal from the two PMTs could be performed and this helps to reduce detector noise. For example, cross-correlation eliminates the effect of afterpulsing. Afterpulsing is a common problem encountered in photon counting detectors and causes a peak in the initial time period of the auto-correlation function[107,108].

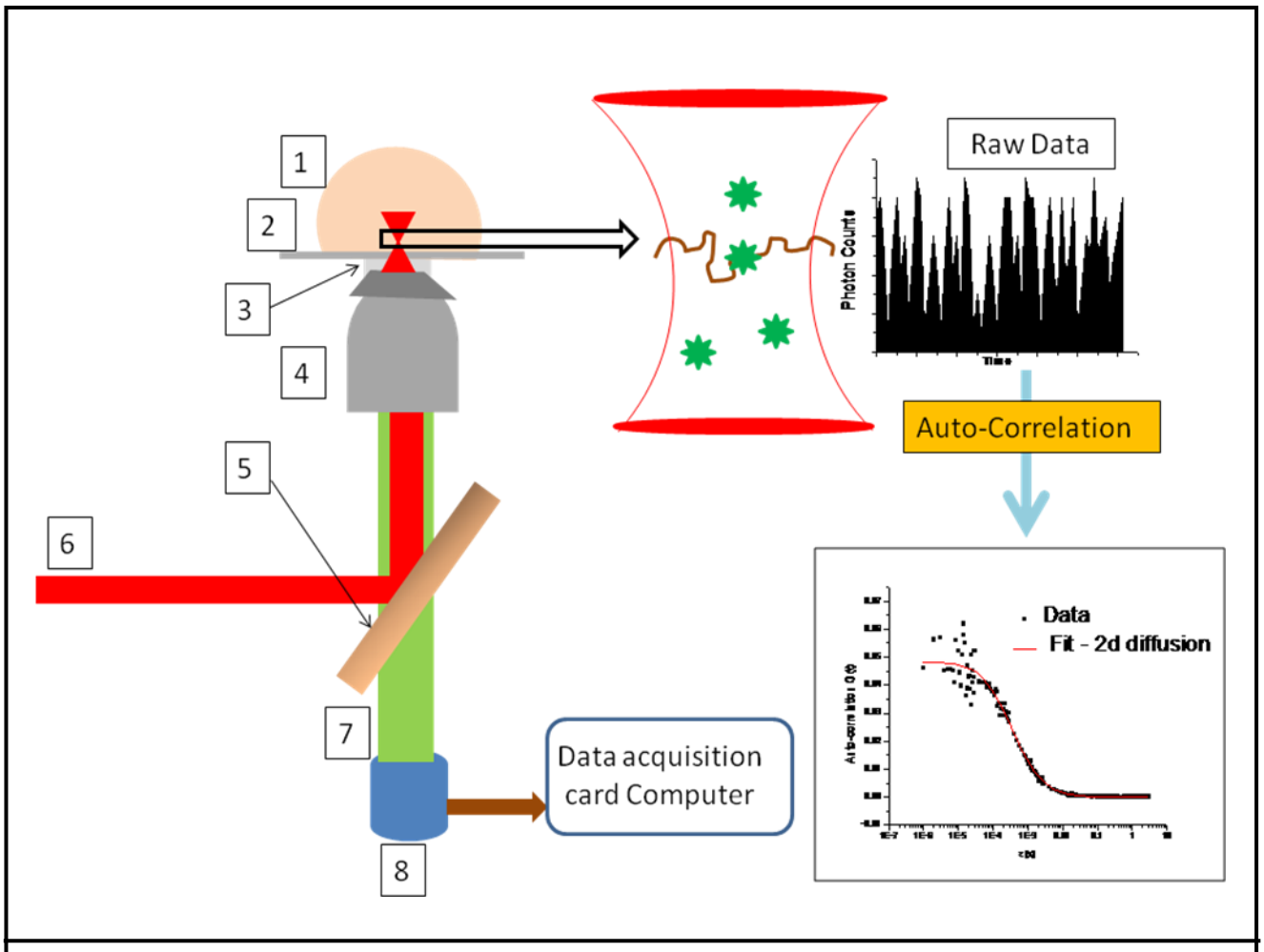

Figure 3.2.2: The schematic of our FCS set-up.1: Sample, 2: #1 microscope cover-slip,3: Index Matching liquid, 4:Objective 100X with NA 1.25, 5: Dichroic mirror that reflects incident red light but transmits green light emitted by fluorescent dyes,6: Red laser light for excitation, 7:Green light from fluorescence emission, 8:Photo multiplier tube.

Chapter 4

INSTRUMENTATION

In this chapter, I describe the design and construction of the combined AFM/FCS platform. The chapter is divided into six sections. In the first section, discussion on the rationale behind integrating AFM with FCS is presented. The second section gives the details of design, construction and implementation of the newly built AFM, which was successfully integrated with an existing custom made FCS setup. In the next section, I elucidate a novel method to coat the end of an optical fiber, which was developed as part of my research[23]. In the fourth section the details of calibration of the various parts of the new AFM are presented. In the penultimate section, the details of experimental procedures and some of the major challenges are presented. In the final section, I present the limitations of the new integrated platform.

4.1 COMBINING AFM AND FCS

AFM can be operated in ambient, liquid or vacuum environments and provides high resolution 3D topographical images. In addition, local mechanical properties can be obtained. Because of its applicability to imaging in liquids, AFM has become very popular in soft-condensed matter and biological applications. However, AFM also has its limitations: The maximum image size is limited to about 100 micrometers, it is difficult to identify different constituents of a surface apart from their topographical shape, and AFM is a surface sensitive technique and can therefore not provide images of the inside of an object such as a cell. Furthermore, the time resolution of AFM is limited to a few milliseconds. It is therefore desirable to combine AFM with other techniques, notably fluorescence microscopy to extend the

utility of AFM. Integrated platforms of AFM and inverted optical microscopes are being manufactured commercially (JPK, Asylum, and Nanosurf) and are becoming a powerful and popular tool for applications in life science research. In addition to simple optical microscopy, other optical techniques like confocal imaging, Raman spectroscopy and fluorescence spectroscopy/imaging have been integrated with AFM. A number of groups [7-11] have used combined AFM and FCS platforms to investigate various systems. Burns et al used FCS to investigate the dynamics of domains in a model membrane and correlated them with the AFM topography measurements. Chiantia et al have reported several studies on the mobility and organization of domains in liquid membranes. Recently, our group in collaboration with Dr. Mukhopadhyay's group has employed a combination of highly sensitive AFM and FCS techniques to investigate a confined fluid formed by tetrakis-2 ethylhexoxy-silane (TEHOS)[4]. Periodic oscillations of the stiffness (with a period close to TEHOS molecular dimension) and the damping coefficient were reported, which indicated ordering of TEHOS upon confinement. FCS measurements performed on thin TEHOS films (deposited by dip-coating) showed that the diffusion within the films slowed 10-fold from that of the bulk TEHOS. This observation supported the view that the liquid at the solid interface may have structure different from that in bulk. However, in this study, AFM and FCS measurements were performed independently. It should be possible, however, to integrate AFM and FCS to perform simultaneous measurements, as has been done in the case of the Surface Force Apparatus (SFA), which was successfully integrated with FCS earlier by Dr. Mukhopadhyay[16].

The integrated platform of SFA and FCS combined surface force measurements and friction studies, performed by SFA, with measurements of translational diffusion, performed by FCS. Orders of magnitude reduction in the diffusion was observed when fluid was confined by

the SFA apparatus, and the diffusion was found be heterogeneous in nature. In addition, experiments to contrast the diffusion rate of confined fluid during shear and at rest were performed[21,109,110]. Relative to the diffusion at rest, an increase (2-5 times) in the diffusion was observed under shear. However, there were limitations to the use of SFA in these measurements. First and foremost, there was instrumental instability due to the large contact area, which caused large attractive forces. This instability created difficulties in systematically varying the thickness of confinement. Due to smaller contact area, AFM has higher mechanical stability. In addition, the geometry of confinement can be varied by employing tips of different geometry since the tip will be used as one of the confining surface. Thus it is advantageous to integrate AFM with FCS for studies of the dynamics of confined fluid and soft matter systems.

4.2 DESIGN, CONSTRUCTION, AND IMPLEMENTATION

In this section, the various aspects pertaining to the construction and integration of a new AFM with an existing custom-made inverted geometry FCS are presented. The basic design principle of the new AFM follows the design of a novel high sensitive small amplitude- AFM (SA-AFM) that was previously built in our group[1,19]. The SA-AFM is a dynamic AFM technique employing amplitude modulation. In such a mode a cantilever is vibrated at a constant frequency, and the changes in amplitude and/or phase are measured with a lock-in amplifier. The SA-AFM is based on what we would like to call the four 'S': Small amplitude, stiff levers, sub-resonance and high-sensitivity. The tip-substrate measurements are linearized due to the very small amplitudes (sub-Angstrom) with which the AFM cantilever is vibrated. By employing sufficiently stiff cantilevers (at least twice interaction stiffness) the AFM has better signal to noise ratio, and simultaneously diminishes the instabilities, which are due to the fact that low stiffness levers cannot resist force regimes with attractive force gradients exceeding the tip

stiffness. Sub-resonance (less than one-eighth of resonance sufficient for best results) operation makes the measurement quasi-static and data interpretation straight-forward. In order for the AFM to satisfy the three 'S' it requires high sensitivity. A fiber based interferometric detection system is used for this purpose.

The optical cavity in the fiber interferometer is formed by a small gap (a few microns) between the end of a fiber, and the top of AFM cantilever. In order to enhance the sensitivity the fiber end is coated with partially reflective thin film. To obtain maximum sensitivity of the detector, the fiber has to be aligned as close and as perpendicular as possible to the cantilever. The alignment of the fiber is made with the help of a 5-axis (3 translations and 2 rotations) inertial slider assembly, which is the heart of the detector system. The assembly works on the inertial principle and employs stacks of shear piezos to provide motion, and screw-mounted magnets to provide the required normal/contact force. The fiber is mounted on a slider, which is the moving part of the assembly. The forward motion of the slider occurs when voltage ramp is applied to the piezo stacks. Upon reaching the peak value, the voltage is reduced to zero fast, and due to inertia the slider does not move back with the piezo. Details of the architecture, electrical connectivity and operation of the assembly of our previously built SA-AFM can be found in Dr. George Matei's PhD thesis[1].

While our previous home-built AFM was a standalone unit, our new AFM is integrated with an existing Zeiss inverted microscope. The new AFM design is modular in nature, which enables us to easily change the sample as well as the AFM cantilevers. In addition, standalone FCS experiments can be performed simply by removing the AFM module. Even though the main design of this new AFM is similar to the instrument previously built in our group, the new AFM has significant differences. These differences are necessary for the smooth integration of the

AFM onto the inverted optical microscope. For example, in the previous AFM, the tip and fiber positioned were stationary, and the sample was scanned in X, Y and Z. However, in an AFM mounted on top of an optical microscope, the fine approach has to be applied to the tip, and therefore, in our fiber-optic based system, the tip holder, as well as the fiber positioner need to be attached to a piezoelectric tube. This is a rather heavy assembly, and it is not a good idea to scan this heavy assembly in all three dimensions. It is therefore better to decouple Z from X and Y. Keeping this in mind, the following lists the differences between our previous AFM design and the new design described in this thesis:

1) The vertical and lateral scanning actuators are decoupled. It removes the 'bowing' artifact that results from bending of tube piezo that are employed in coupled systems. In addition, the design becomes relatively straightforward. The vertical scanner which consists of a tube piezo (ID 1") moves not only the AFM cantilever, but also the fiber-optical interferometer assembly, including the fiber slider. The vertical scanner is used for fine approach. Since both the cantilever and the fiber positioner are attached to the fine approach piezo, the fine approach of the tip can be achieved without loss of fiber alignment. The vertical scanner is also used to maintain a constant distance, or to move according to a programmed vertical ramp for force-distance measurements.

2) A closed loop scanning stage (from Physik Instrumente) is used for lateral (XY) motion of the sample and provides the coarse approach toward the tip.

Another difference is a new process developed for coating the end of the optical fiber (to enhance its reflectivity). Previously, the fiber was coated (by thermal evaporation or by sputtering) with Si with a thin layer protective gold coating. This was cumbersome and time-intensive, as well as expensive (use of gold). Instead, TiO_2 was tried as a new coating. A new process employing metal-oxide-decomposition (MOD) technique to obtain a thin film TiO_2 coating was developed. The novel method that was developed to coat the fiber end, and the working principle of the interferometer are presented in the next section. In addition to these

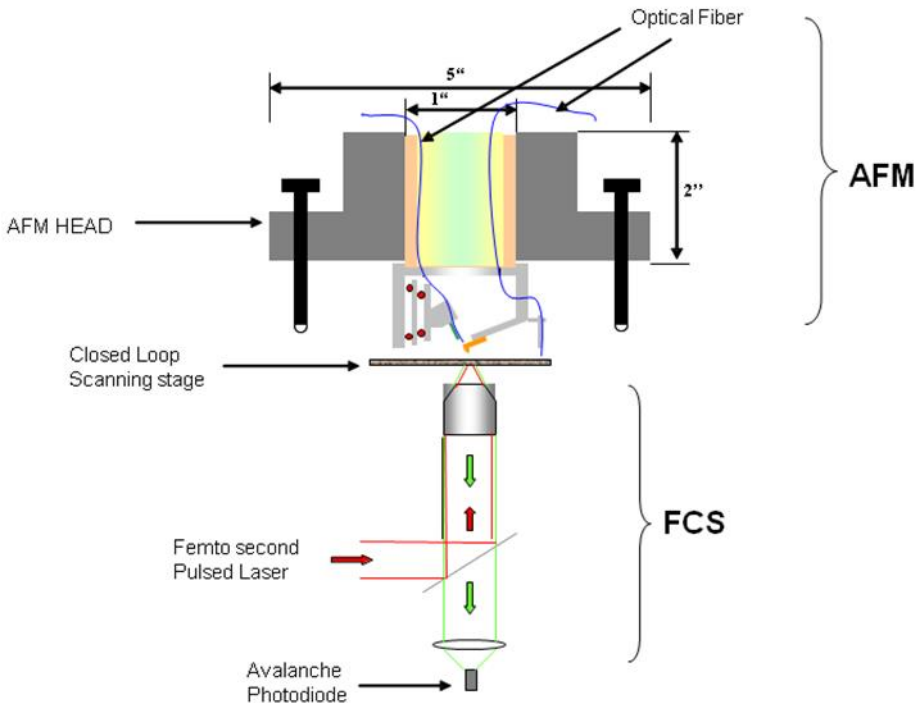

Figure 4.2.1: Combined AFM-FCS Schematics. The schematic illustrates the modular nature of our design. The AFM on the top can be easily removed to change samples and or cantilevers without disturbing the optical stage.

major differences, there are a few minor changes in the design and implementation that were made in order to facilitate the integration with FCS setup, which we will discuss in more detail below. With the exceptions of few small parts, all the machining was done by either WSU science store machine shop or by Apollo E.D.M Company, Fraser, MI.

4.2.1 COMBINING AFM WITH INVERTED MICROSCOPE

Our AFM is designed in a modular architecture so that it can be easily mounted on top of an inverted microscope. Apart from the geometry of the microscope, there are additional constrains imposed on the design due to the presence of the fiber interferometric detection system used in the AFM. Therefore, the vertical (z) motion was decoupled from the lateral motion. In addition, cantilever assembly and fiber slider assembly were integrated with the tube piezo that performs the z-scan. All the three components along with the stainless steel fixture form the head of the AFM (Figure 4.2.1.1). A heavy (~ 45 lbs) 2-axis manual translation stage forms the base of the AFM (4.2.1.2). The AFM head is placed on top of a stainless base plate, which is screwed to the base.

The close-up photographs of the AFM and the base are shown in Figure 4.2.1.2. Three micrometer screws (# 3 in Figure 4.2.1.2a), each with a spherical bottom, form the legs of the head and rest on the base-plate. Two of the screws contact the base-plate via two pairs of small parallel half- cylinders with a small spacing, rigidly pressed into the base-plate, and the third screw contacts the base-plate via a set of three hemispheres that are protruding on top of the base-plates. The sizes of the cylinders, the gaps and spheres are chosen to match with the size of the spherical bottom of the micrometer screws. The two sets of cylinders are arranged perpendicular. The weight of the AFM head provided the sufficient force to rigidly couple the

AFM to the base, and the protrusions geometry maintains mechanical stability in the lateral direction. In Figure 4.2.1.2b a photograph of the base of the AFM is presented, in which the protrusions are indicated by circular markers. Machining of the groves for cylinders and spheres were performed by wire electrical discharge machining process (Apollo E.D.M.).

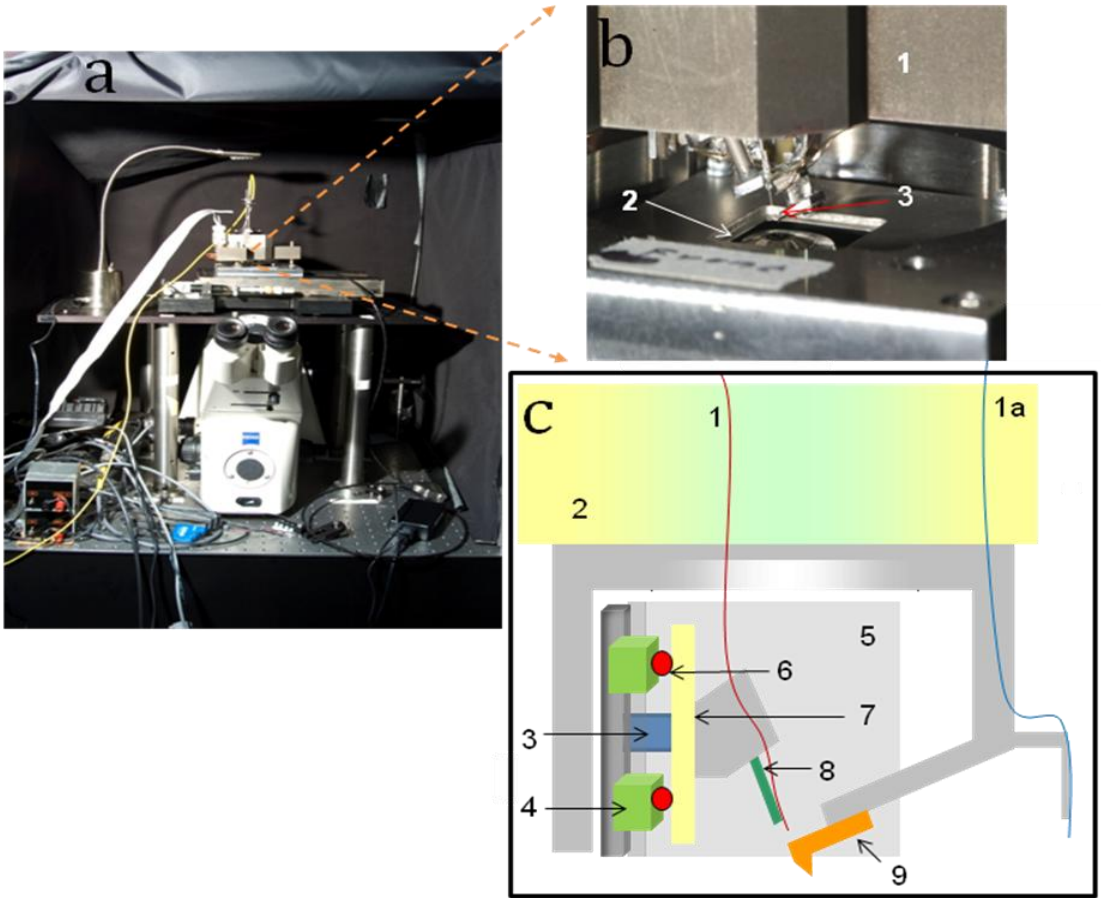

Figure 4.2.1.1: (a) Photograph of the entire AFM/FCS setup; (b) Close up of the bottom of AFM head: 1- Stainless steel body, 2- Microscope objective and 3- Cantilever holder; (c) Schematic of the various active components of the head: 1-Fiber used for AFM measurements, 1a- Additional fiber for independent tip-substrate distance monitoring (not present currently, can be incorporated in future), 2- Tube piezo for vertical motion, 3- Magnet providing the contact force for the small slider, 4- Piezo stack, and 5- L shaped large slider, 6-Ruby ball, 7- Small slider, 8- Fiber piezo and 9- Cantilever.

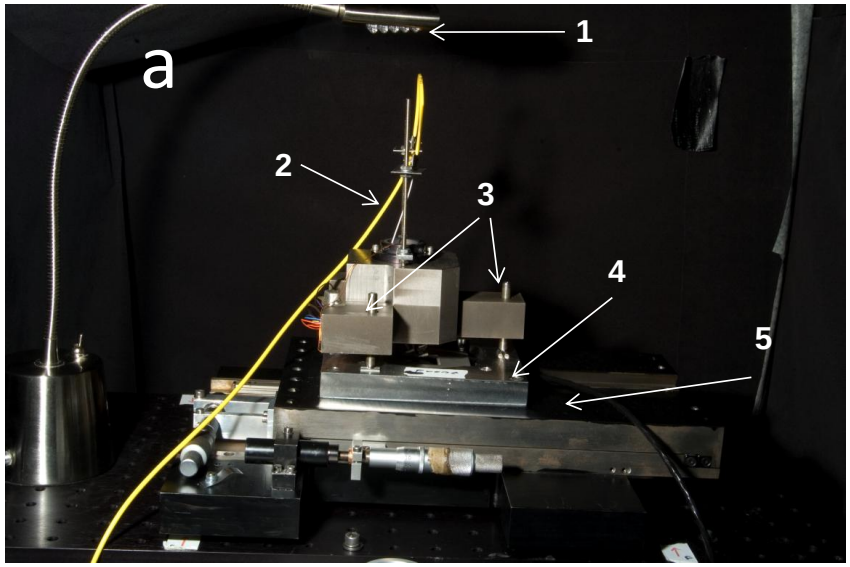

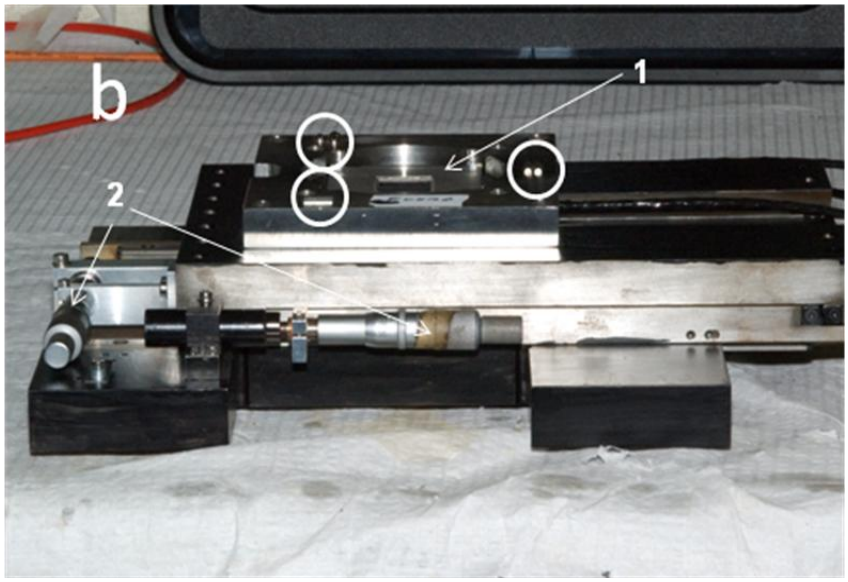

Figure 4.2.1.2: (a) Photograph of major parts of AFM mounted on the base: 1- LED lighting for microscope usage, 2- Fiber for AFM measurements, 3- Micrometer screws that forms the legs of AFM, 4- Stainless steel base-plate, and 5- Base of AF; (b) Photograph of the AFM base: 1- sample plate, 2- Micrometer calipers for translation and the circular markers indicate the protrusions.

The base plate is made up of stainless steel and serves two purposes. It is used for attaching the closed-loop scanner (Physikinstrumente) and for placing the AFM head. The closed-loop scanner holds a stainless steel sample plate, which is attached to the scanner by four screws. The entire assembly is attached to the bottom side of the plate, which has a grove that matches the dimension of the scanner. In Figure 4.2.1.3 a photograph of the scanner and the drawing of the base plate along with the sample plate are shown. The base-plate and sample plate were machined in the WSU machine shop.

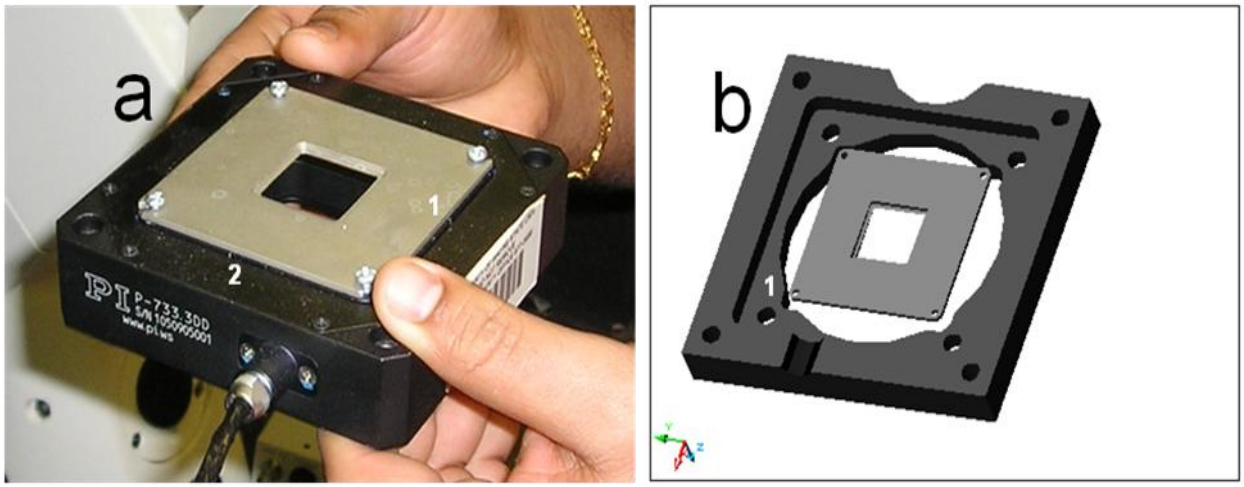

Figure 4.2.1.3: (a) Photograph of sample plate fixed to the scanner: 1- Sample plate and 2- Scanner; (b) Drawing of base-plate and sample plate: 1- Grove to fix scanner.

The AFM head is made from stainless steel; a 3D rendering is presented in Figure 4.2.1.4. It has a through hole to house the vertical piezoelectric scanner and a slot on the bottom side to house the slider and cantilever holder assemblies. In addition, three through holes are present wherein brass bushings are press fit. These bushing are tapped and hold the micrometer

screws (Thor Labs). The micrometer screws are used for fine controlled motion of the entire head in the vertical direction.

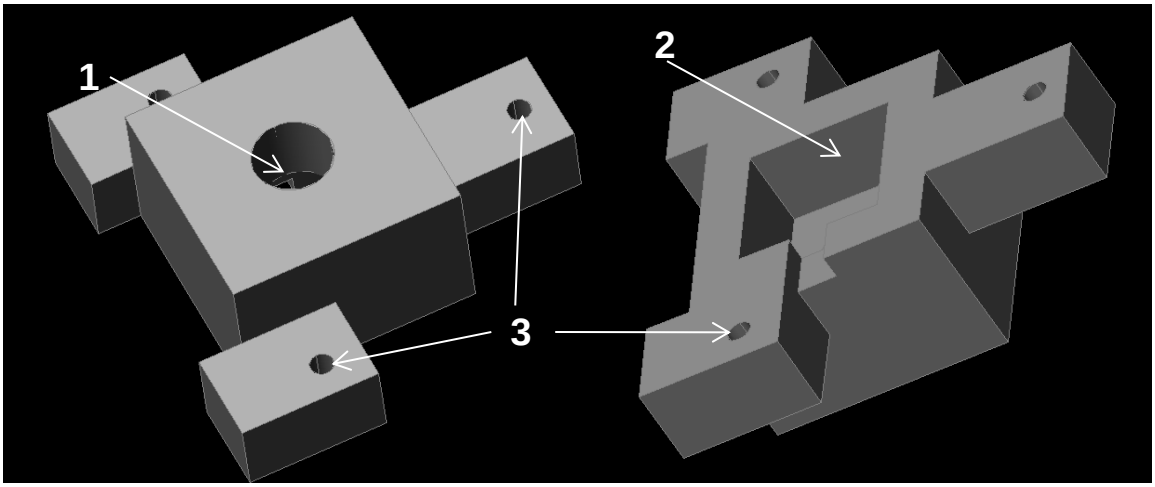

Figure 4.2.1.4: Drawing of the AFM head. Top view (left) and side bottom view (right): 1- Through hole for tube piezo, 2- Slot to house slider and cantilever assembly and 3- Holes for micrometer screws.

As mentioned earlier, in the AFM the slider and cantilever are rigidly coupled (with epoxy) to tube piezo on one end (bottom). The other end of the tube is rigidly fixed on the top AFM head. When voltage is applied to the piezo the tube expands or contracts depending on the sign of the voltage. A new cantilever holder assembly - very different from previous AFM - was designed. In the previous AFM the slider and cantilever holder were decoupled from one another and hence that design was not suitable for the new AFM, in which the cantilever and fiber need to be moved together to maintain fiber alignment. In Figure 4.2.1.5, a photograph of the bottom side of the AFM (a) and a drawing of the cantilever holder assembly (b) are presented. In addition to the geometry, insulation materials used as spacers in the holder assembly are different compared to the previous AFM. In the new cantilever holder, glass and

sapphire are used in the place of macor. A thin sheet of sapphire was used in-between the steel base and one side of the piezo element. A glass cylinder was used in-between the spring clip and other side of the piezo element (Figure 4.2.1.5a).

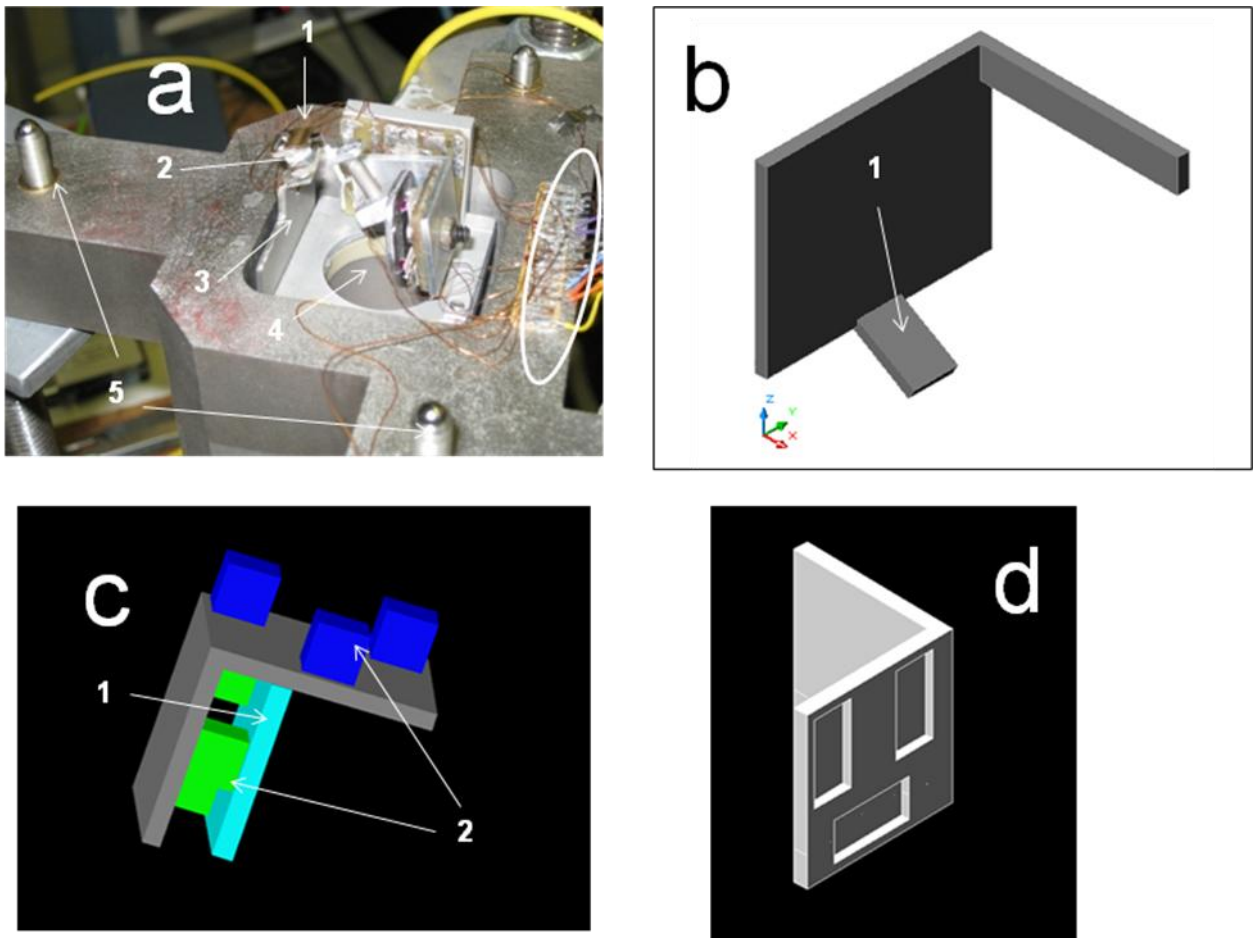

Figure 4.2.1.5: (a) Photograph of bottom of the AFM head: 1- Spring clip that holds the cantilever, 2- Glass spacer, 3- Cantilever holder assembly, 4- Tube piezo for vertical motion, 5- Micrometer screws (legs) and PCB for electrical connection is shown by the white ellipse; (b) Drawing of cantilever holder assembly: 1- Steel base where piezo stack, spacers and spring clip are glued (epoxy; (c) Drawing of fiber sliders: 1- Small slider to which the fiber piezo is attached, is made from stainless steel, 2- with piezo stacks (blue & green); (c) Drawing of large slider showing the slots that to restrict its motion.

Unlike the cantilever holder assembly, the overall design of slider assembly is similar to that of the previously built slider assembly. However, some significant improvements were made in the implementation. The slider assembly has two sliding pieces, which are shown in Figure 4.2.1.5. The sliders are held in place with help of magnets, similar to the previous assembly. However, neodymium based stronger and smaller magnets were employed in the new assembly. The magnets supply the needed contact force for slider operation. The larger 'L' shaped piece is made from aluminum, and the smaller piece (#1 in Figure 4.2.1.5c) is made from magnetic stainless piece. In the previous assembly both the sliders were made from aluminum. Using magnetic material provides a stronger magnetic field and improves the stability of the slider assembly. Due to weight consideration the large slider was made using aluminum. Another improvement was the introduction of slots in the sliders. These slots restrict the motion of the sliders, and thus the slider is prevented from falling out during alignment.

4.3 A NOVEL METHOD TO COAT AN OPTICAL FIBER END

In the new AFM, we employed an interferometric detection system, which was required in the experiments to measure very low signals. In Figure 4.3.1 the interferometer principle is schematically illustrated. In fiber based interferometers, [19,27,111] a perfectly cleaved end of the fiber serves as the reference mirror while another reflecting surface, whose displacement is to be measured, serves as the second mirror. However, the air-glass interface of a freshly cleaved fiber has only ~ 3% to 4% reflectivity. Because of this low reflectivity, most of the light exits the fiber and, if not scattered, re-enters the fiber to interfere with the very small amount of light that was reflected internally. Thus, interference is incomplete, leading to only small changes in intensity as a function of mirror spacing. As very little light is reflected again

by the fiber end, multiple reflections that would improve resolution do not occur. The reflectivity of the fiber end can be increased by coating it with a partially reflecting thin film. This way the reflectivity can be tuned to more internal reflection, such that the intensity of the light re-entering the fiber matches the intensity of the internally reflected light. This leads to better finesse of the interferometer cavity. In addition, the higher reflectivity allows for multiple reflections, which improves the finesse even further. The optimal value for the reflectivity depends on scattering and absorption in the film, and typically ranges from 15 – 30% in our experience. The improved finesse improves the distance resolution of the fiber-optic interferometer.

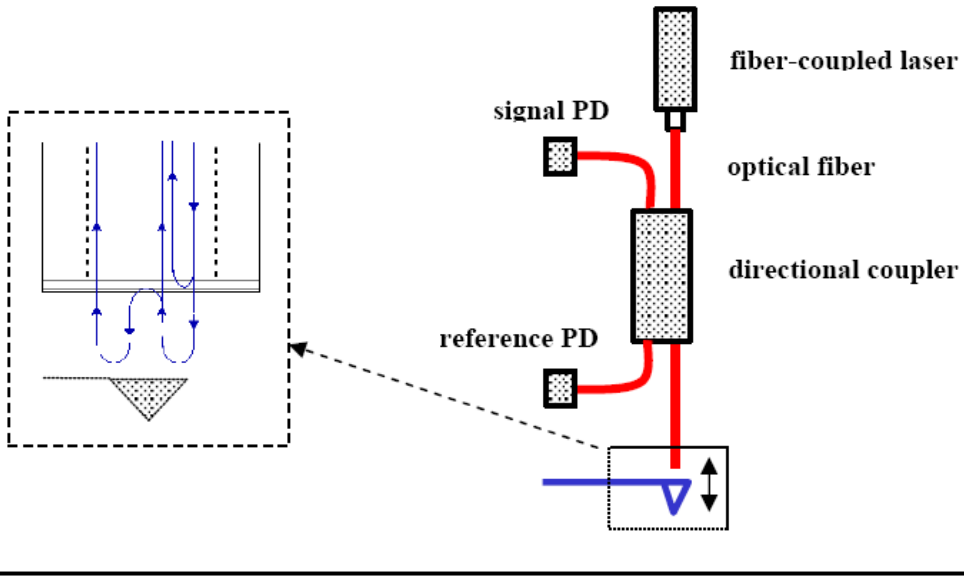

Figure 4.3.1: Interferometric detection system schematic

In the past, we have used thermally evaporated Si with a protective Au thin film[19]. With the protective Au film, which prevents oxidation of Si, the fibers coated with Si were very stable in ambient and vacuum conditions. However, for applications involving a liquid environment

one requires a robust and stable coating. In gold coated fibers, water can penetrate to the underlying silicon through fine cracks or pores in the protecting film. We found that the coating peels off after a few hours when immersed in water due to loss of adhesion. It should be noted that in order to increase the adhesion of Au on Si a thin layer of Cr could be used. However, such application of multiple layers complicates deposition procedures and introduces multiple reflections and absorption from several interfaces. Metal coatings, such as Au and Cr, absorb in the infrared (we are using a 1310 nm laser). We found that TiO_2 may provide a better choice as the optical reflectivity of TiO_2 is similar to that of Si in the wavelength range we employ, it does not absorb in the infrared, and as an oxide it is not prone to undergo further oxidation in liquids.

Liquid	H_2O	OMCTS	0.5 M NaCl	0.2 M PBS	0.1 M TRIS HCl
Reflectivity	13.5 %	13.2 %	15.3 %	15.4 %	16.5%

Table 4.3.1: List of liquids in which the fiber was immersed for 24 hours to test for it robustness. The shown reflectivities did not change during entire duration of the immersion time.

The quality and robustness of TiO_2 coated fibers were tested by immersing them in various liquids (Table 4.3.1) while their reflectivity was monitored. Unlike the Au/Si coated fibers, the TiO_2 coated fibers showed no change in the reflectivity even for prolonged immersion (24 hours). Conventional physical vapor deposition techniques such as thermal evaporation or sputter deposition techniques are typically used to deposit these thin film coatings. However, for good results, the fiber needs to be completely stripped along a significant length (more than a foot) before placing into the vacuum chamber. Otherwise, outgassing from the plastic coating

will lead to poor results. Such long sections of unprotected fiber are very fragile. In addition, high vacuum deposition techniques make the mounting (and removal) of the fiber into the deposition chamber cumbersome and time-consuming. For the TiO_2 coating described here, the fiber needs to be only stripped enough to allow for mounting into the fiber cleaver, i.e. only about 1 inch. The new technique, presented in this paper, does not require vacuum to coat the end of a single fiber. Instead by using metal-organic decomposition (MOD) technique[112,113], we can coat a fiber in just a few minutes versus hours of preparation and mounting required in the case of vacuum based techniques. Moreover, as we will show, the TiO_2 coated fiber yield excellent sensitivity for interferometric applications and are more stable in liquids than vacuum coated fibers. The stability in liquids, resulting high optical finesse and quick turnaround time make this coating method an attractive technique for high demand situations, such as measurements in aqueous systems. The experimental details are presented in the next paragraph.

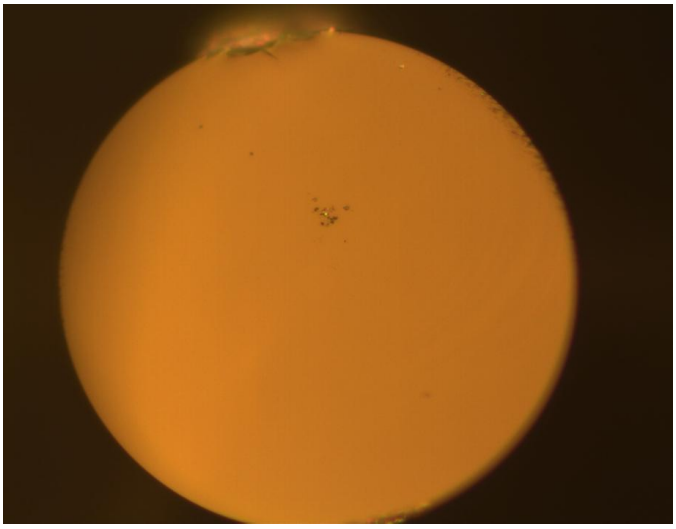

Figure 4.3.2: Optical image of a perpendicularly cleaved fiber with 3% reflectivity. The top edge of the image shows the fractured region (caused by cleaver) in the cladding (diameter 125 µm).

A single mode optical fiber (AF/AF-S01, Metrotek) with 9 μm core and 125 μm cladding was used in these studies. First the end of the fiber was stripped off the mechanical protective layers using stripping tools (Clauss Fiber Optic stripper CFS-2 and 175 μm, Metrotek). The bare fiber was then cleaved using a specialized cleaver (Fujikura CT-20 High Precision cleaver, Metrotek) which gives approximately 3% of reflectivity for 1310 nm IR. Figure 4.3.2 shows an optical microscopy image of the cleaved, clean fiber. After cleaving, a thin film of TiO_2 was coated by dip coating into a metal-organic precursor. Metal organic decomposition (MOD) is one of the commonly employed thin-film deposition technique for metal oxides[112,113]. In this method a suitable organic precursor containing the metal of interest is applied on the substrate (either by dip or spin coating) and then the substrate is baked at high temperature. During this annealing process organics decompose and the oxides of the metals form a uniform thin film on the substrate. The thickness of the film can be varied by controlling the concentration of the precursor as well by carrying out multiple coating. However, for my applications, since the thickness of the coating required is typically few tens of nanometer, I employed a single dip coating method. An optimized concentration of titanium-(IV)-2-ethylhexoxide (8.5 wt % of Ti; Alfa Aesar) diluted in Xylene was used as the precursor. Typically five times dilution of the stock solution gave consistent results. The cleaved fiber end (~ few mm) was dipped in the precursor solution and then fired to high temperature by a propane torch light. Only the very end of the fiber (~1 mm) was introduced into a flash at 700 ^{o}C for about a second and then retracted. The optimal flashing time was determined by trial and error based on subsequent characterization and optical measurements, as described below. The rapid flash annealing decomposes the organics, while also preventing any damage to the fiber due to the long exposure to high temperature. The annealing procedure is also advantageous as it leads to highly

crystalline phase of TiO_2 coating compared to the amorphous films obtained by the physical vapor deposition techniques, where deposition is carried out at ambient temperature. During the coating and annealing process the reflectivity of the fiber end was monitored using a signal photodiode. I also studied the quality and stability of the TiO_2 thin film coated fiber for its application in the interferometer employed in air and liquid environment. The surface morphology of the fiber end before and after coating was studied by optical and scanning electron microscopes. To check the crystalline quality of the coated films micro-Raman spectroscopy was performed. The details of the results obtained from various characterization techniques employed are presented in the following paragraphs.

The reflectivity of the fiber was monitored while the fiber end was dip-coated with the precursor and also during the rapid annealing process. The 3% reflectivity of the bare tip did not change significantly when dip coated with the precursor. However, as the fiber end was introduced into the flame for annealing, a rapid increase in the reflectivity was observed. The fiber was retracted as soon as the reflectivity increased to 15 to 25 %, typically no longer than 1 second. Longer exposure of the fiber in the flame led to curling or cracking, thereby damaging the fiber irreversibly (requiring re-cleaving of the fiber). Though there was no optimal control of getting a specific reflectivity for these fibers by this process, the resulting reflectivities in the range of 15 to 25% are well suited for measurements carried out in liquid or air environment. The obtained reflectivity depended on the concentration and viscosity of the precursor. For higher concentration and viscous solutions, the dip-coated fiber had a large droplet at the end of the fiber, which leads to a non-uniform film and very rough or cracked surfaces during annealing process. As an example, I show the optical microscope image of the two fiber tips with 22% and 8% reflectivity after annealing (Figure 4.3.3). The former was coated using a dilute solution, and

the latter was coated using a viscous solution. The fiber with higher reflectivity had smooth and uniform thin film coating. On the other hand, the fiber with low reflectivity had very non-uniform thick surface. The SEM micrograph of the uniformly coated tip is shown in Figure 4.3.4a. A magnified image from the center region is shown in Figure 4.3.4b showing highly crystalline grains of TiO_2.

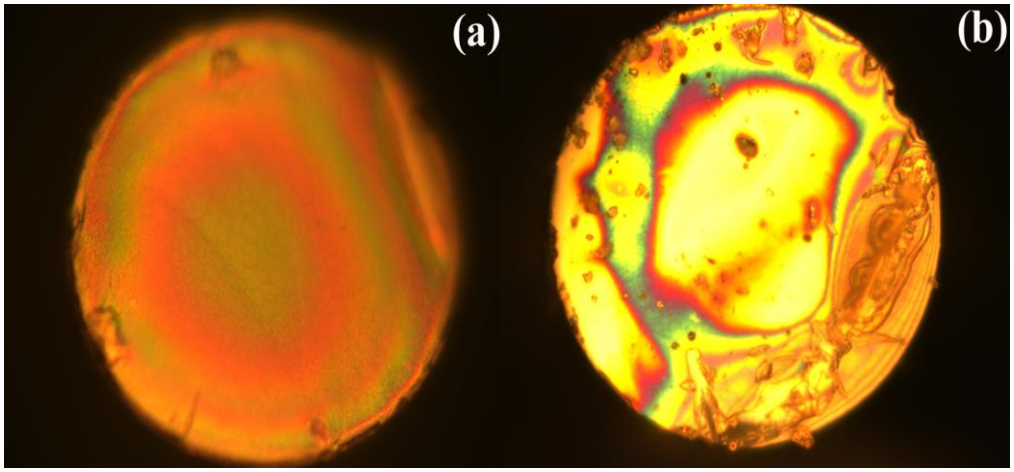

Figure 4.3.3: Optical image of a MOD coated fiber end. (a) Uniform coating resulting in R = 22% (b) Non-uniform coating resulting in R = 8%.

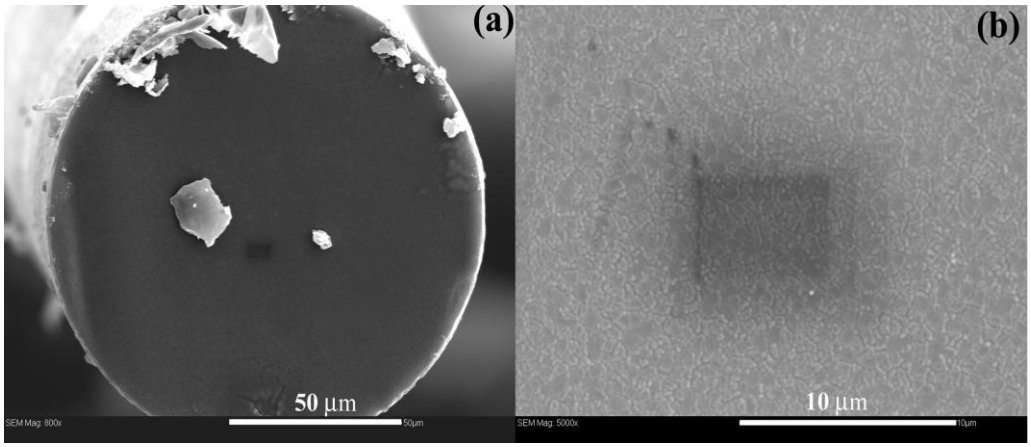

Figure 4.3.4: SEM micrograph of (a) Uniformly coated fiber end with R=22% (b) A magnified image from the center of the fiber end in (a) shows the TiO_2 grains. Note that the dark patch in the center of a & b is due to the damage from repeated scanning at higher magnification.

To understand the structural quality of the film, we carried out micro-Raman spectroscopy using 514.5 nm (2.41 eV) excitation line from an Ar^+ ion laser. Figure 4.3.5 shows Raman spectra of bare, non-uniformly coated, and uniformly coated fiber ends. The Raman spectra of non-uniformly coated films showed major anatase phase with some rutile phase in regions of heterogeneous coverage. In contrast, the uniformly coated film showed only rutile phase of TiO_2. Of the several coatings we carried out by this method, the uniformly coated tips with high reflectivity (>12%) always showed homogeneous phase of rutile TiO_2.

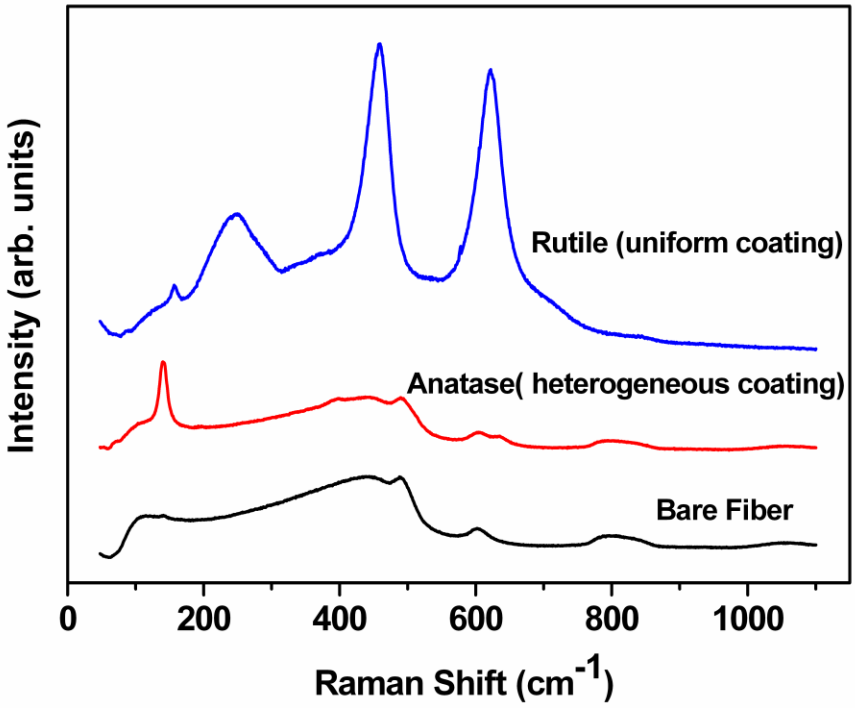

Figure 4.3.5: Raman spectrum of uncoated (black) and coated fibers (red and blue). Red: non-uniformly coated fiber showing anatase phase; Blue: uniformly coated fiber showing rutile phase. The spectra are shifted along the y-axis for clarity.

The coated fibers were then optically tested to check if they were suitable for use in the interferometer. The fiber was mounted on a home-built fiber optic based interferometric testing system[7]. The schematic of the interferometer is shown in Figure 4.3.6a. Using this setup, fibers as well as cantilevers can be tested. In this setup, the optical fiber is glued to a piezo tube, which in turn is attached rigidly to a 5-axis inertial slider (Figure 4.3.6b). The slider is used to align the

fiber perpendicular to a mirror or backside (that has a reflecting coating) of a cantilever, thereby forming an optical cavity between the two. In order to test either the fiber or the cantilever, the interference pattern formed between the light rays reflected from either side of the optical cavity is observed. During the testing, the position of the fiber end and thus the size of the optical cavity is changed periodically by applying an AC voltage to the piezo tube, which extends and contracts the piezo tube. A plot of light intensity reflected back into the signal photodiode versus fiber position (or piezo voltage) provides the continuously measured interference pattern. The photo-current generated by the photodiode is converted to voltage and then that voltage is amplified with variable gain up to a maximum of 80 times (set by the user). By observing the changes in the interference pattern due to the changes in the optical cavity size, one can ascertain the quality of the reflecting surfaces (either the fiber or the mirror). From the interference pattern the sensitivity (in V/Å) defined as the voltage (obtained after amplification) per Å change in the distance of the optical cavity, can be determined. For a perfectly cleaved fiber, which has reflectivity of about 4%, sensitivity of 15mV/Å was obtained. The MOD coated fibers gave high sensitivity (~130 mV/Å) without any increase in the noise level. In both cases the same mirror (sputter-coated Al on glass) was employed. Such high sensitivity allows us to measure dynamic displacements of less than 0.01 nm above the noise floor using lock-in detection.

Through this work we have successfully demonstrated a new application of MOD, a well-known method in solid-state thin film technology. The thin film coating at the end of an optical fiber using the MOD technique was found to be of good quality to be employed for high resolution fiber-optic interferometry. This method is fast and easy in comparison with other

physical vapor deposition methods, namely evaporation or sputter deposition, which can be cumbersome and expensive.

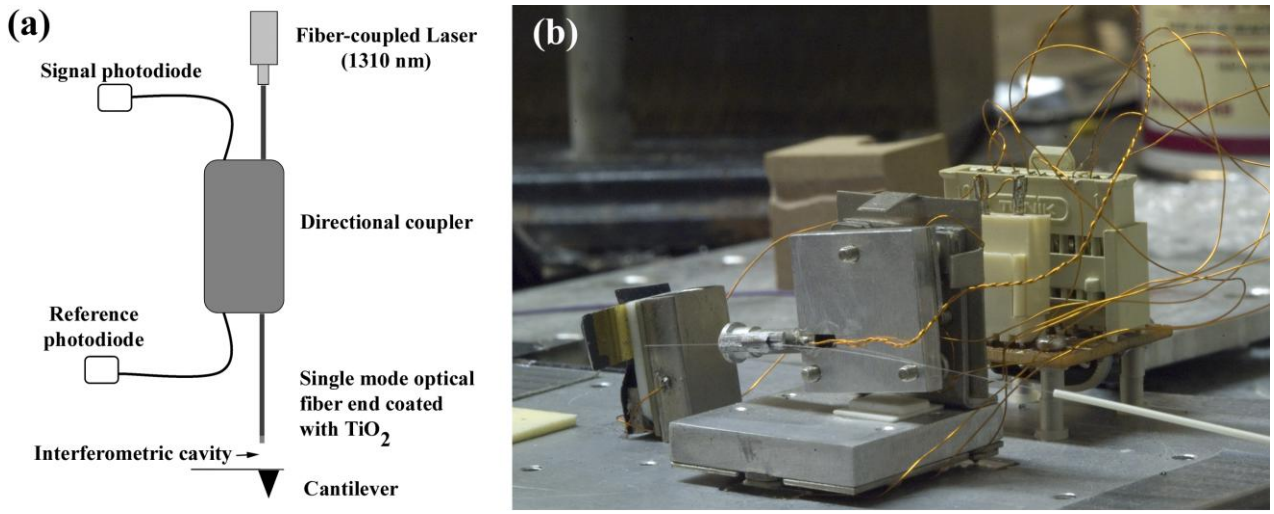

Fig. 4.3.6: Interferometric testing system. (a) Schematic (b) Actual.

4.4 CALIBRATIONS

Proper calibrations were performed for the motion generated by various piezo elements of the new AFM. In this section, the method and results of the different calibrations are presented. First, the calibration of the fiber piezo, which is needed to obtain quantitatively correct interference pattern, was performed by perpendicularly aligning the fiber to a front reflecting mirror (securely placed in the cantilever holder) made from coating a thin film of Au or Al on a piece of mica (diameter ~ 1.5 cm). In order to perform the calibration a well defined triangular wave of frequency 2 Hz, and amplitude ~ 180V was applied to the fiber piezo. This resulted in periodically varying the distance between the tip of the fiber and the mirror, and thus

in an interference pattern observed on the computer or on an oscilloscope. From the interference pattern the piezo calibration factor (in units of Å/V) was determined from equating the distance (in V) between two consecutive peaks to half the wavelength of the laser light used. The wavelength of the laser used was 1310 nm. In figure 4.4.1, typical plots related to calibration factor of the piezo are shown.

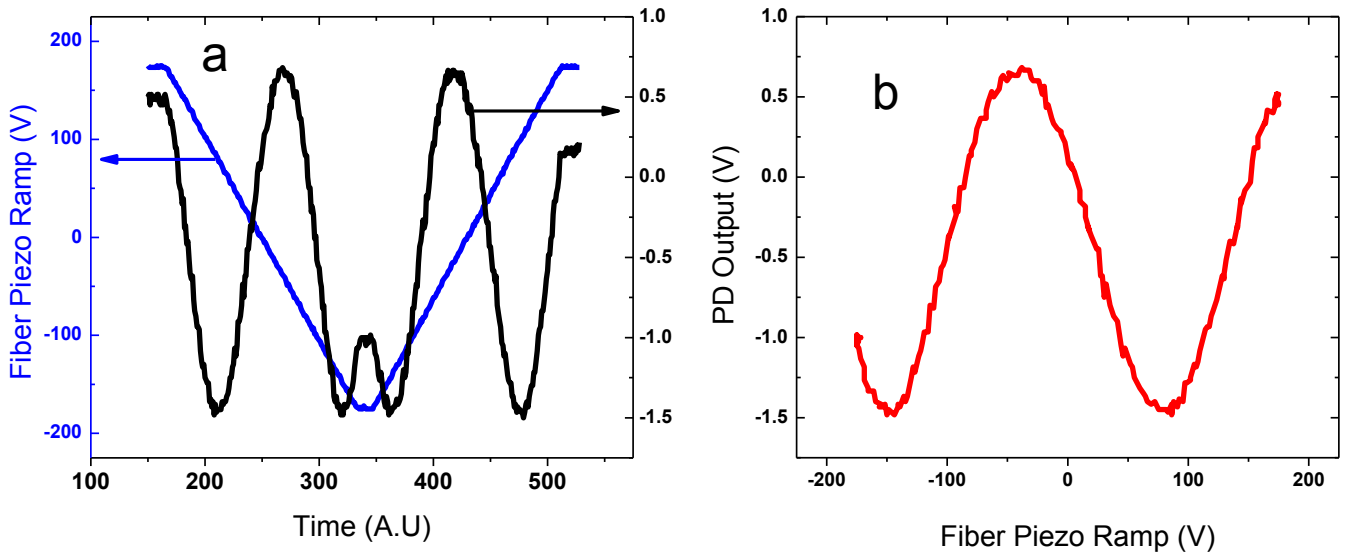

Figure 4.4.1: Fiber piezo calibration. (a) Photo diode (PD) output monitored in time upon driving the fiber piezo with a ramp; (b) PD output vs ramp voltage to obtain fiber piezo calibration constant by equating the peak to peak separation to λ/2, where λ =1310 nm is the wavelength of laser used in the interferometric detection system.

Next a similar procedure was used to calibrate the vertical scan piezo, which is used to move the cantilever of the AFM towards the sample. In the case of the vertical scanner, a mirror was placed on the sample cell and the fiber was aligned to it in the absence of any cantilever. Then the above mentioned triangular wave was applied to the piezo and the calibration factor

was determined. In Figure 4.4.2, the graphs corresponding to the vertical scanner calibration are presented.

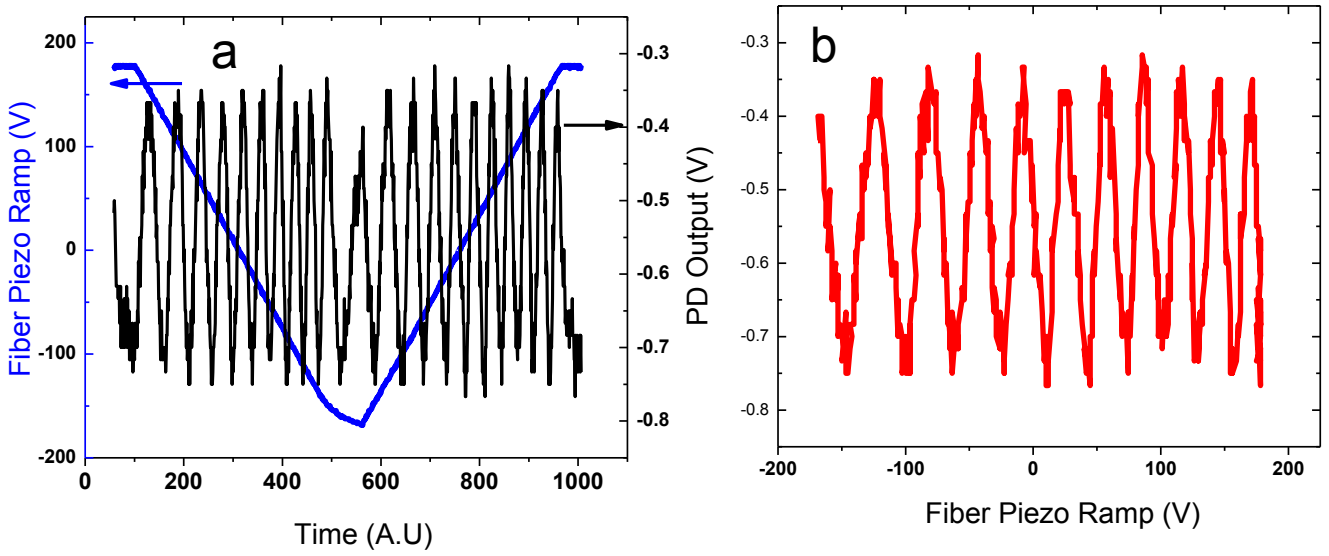

Figure 4.4.2: Calibration of vertical scan piezo. (a) Photo diode (PD) output monitored in time upon driving the fiber piezo with a ramp; (b) PD output vs ramp voltage to obtain fiber piezo calibration constant by equating the peak to peak separation to λ/2, where λ =1310nm is the wavelength of laser used in the interferometric detection system.

Finally, the dither piezo, which vibrates the cantilever for amplitude modulation measurements of the interaction stiffness, needs to be calibrated. The calibration factor was obtained by varying the voltage applied (from the output of a lock-in amplifier) to the dither piezo and measuring the corresponding free amplitude of the cantilever. To measure the cantilever amplitude the fiber is first aligned, and the interferometer is locked at the quadrature

point, where the interference pattern has maximum slope. To obtain the correct value for slope (expressed in V/Å) the calibration of fiber piezo mentioned is essential. The signal from interferometer is fed to lock-in to measure the voltage at the oscillation frequency. Dividing the voltage by the slope we obtain the amplitude of the cantilever vibration. The graph of amplitude versus voltage is linear and the slope of the line gives the calibration (see Figure 4.4.3). The frequency response of the cantilever and the cantilever holder assembly is determined from varying the frequency of the sine wave (from lock-in), which is presented in Figure 4.4.4. Such a response function is needed to avoid any instrumental resonances while performing AFM experiments. The various peaks seen in the frequency response corresponds to the resonant frequency of various parts of the cantilever holder assembly.

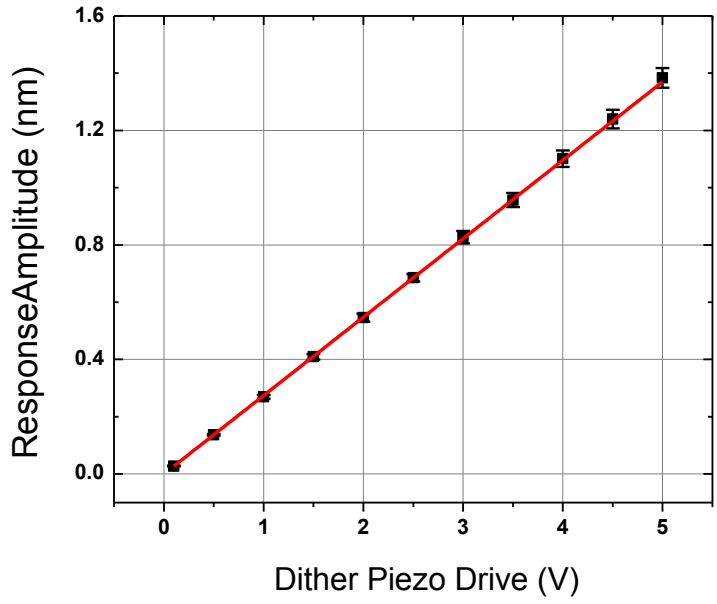

Figure 4.4.3: Dither piezo calibration. As a function of drive voltage, the piezo response with error bars (square) along with a linear fit (line) are plotted.

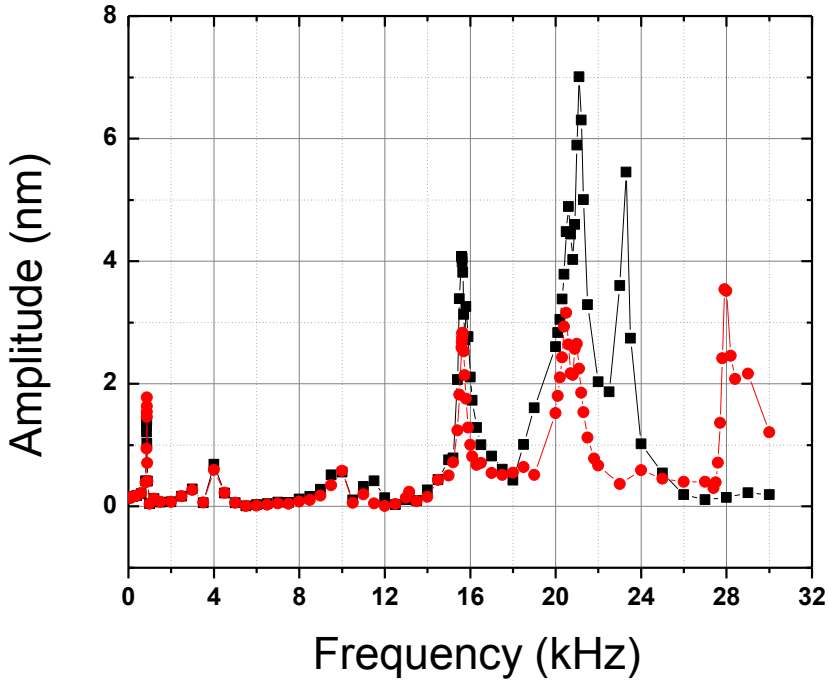

Figure 4.4.4: Frequency response of the cantilever holder assembly. For a fixed drive amplitude of 300 mV, the response of the cantilever measured as a function of oscillation frequency of the dither piezo. Data was obtained for both water (square) and in air (circle). Various peaks in plot correspond to the natural frequency of the different parts of the cantilever holder assembly. While performing SA-AFM, care should be taken to avoid any of the peaks.

4.5 CHALLENGES AND EXPERIMENTAL PROCEDURES

4.5.1 CHALLENGES

Some challenges were encountered during the design, implementation and experimentation with the new integrated platform. Most of these issues were successfully solved. Few major challenges that were solved are:

1) Rigid coupling of AFM with the FCS microscope
2) Visualization of AFM tip, and its alignment with FCS laser focus
3) Course and fine approaches of AFM cantilever towards the substrate

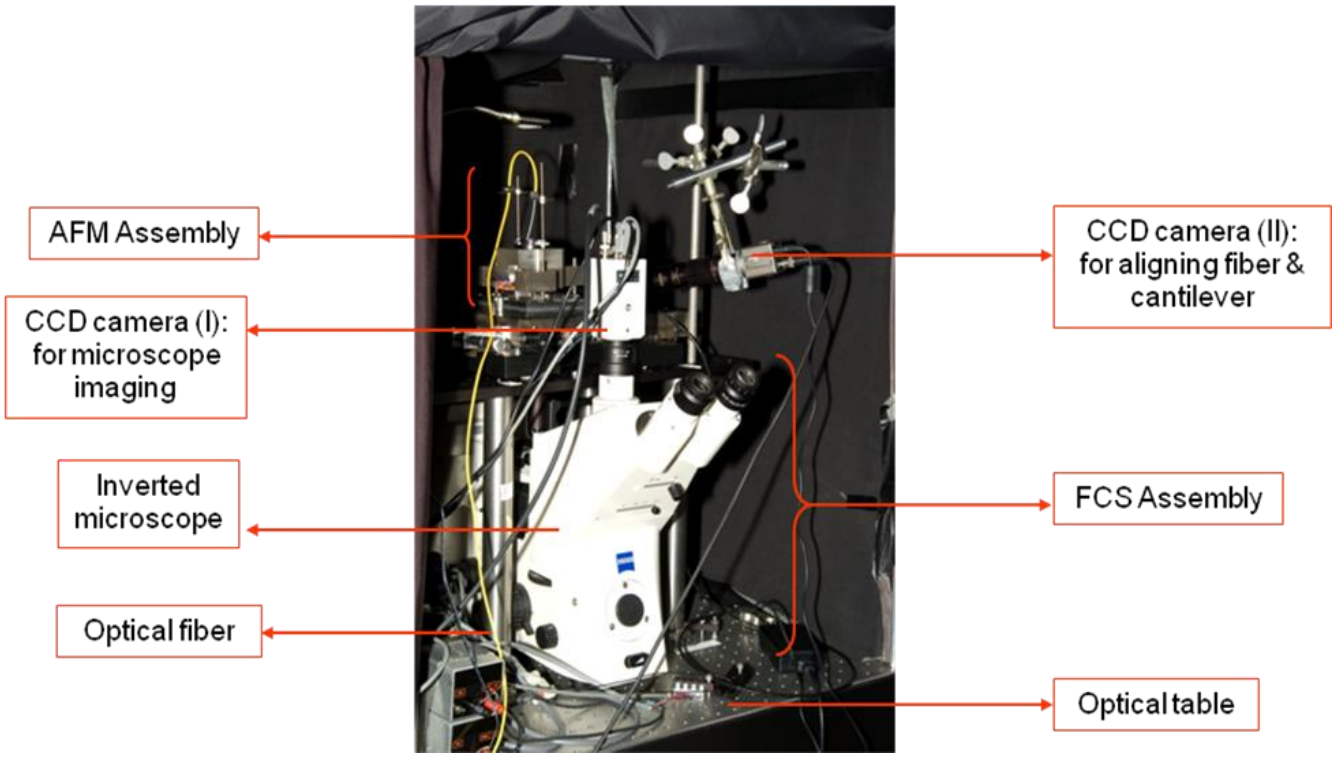

Figure 4.5.1: Picture of the AFM/FCS platform with all the accessories mounted just before the start of any experiment.

In order to rigidly couple AFM with the microscope, a new platform was used in the place of the microscope's sample stage. The platform was made from ¼" aluminum with a center hole (~10" diameter) for the microscope objective to pass through. The platform was rigidly screwed to the body of microscope. The two-axis manual translation station that forms the base of the AFM is rigidly mounted on top of the plate. The head of the AFM and the sample stage are rigidly coupled to the base by a 1'' thick stainless steel base plate (Figure 4.2.1.2), as described above. Due to this arrangement an objective extender was employed in order to increase the height of the objective to reach the object plane.

Visualization and alignment of AFM cantilever was achieved with the help of an external LED based light source that was placed on the plate. The position and orientation of illumination was optimized by trial and error. A CCD camera (#2) mounted for a sideways view of the AFM cantilever aided in visualization and alignment of the tip. The three micrometer screws, which form legs of the AFM head, are used to bring AFM cantilever close. The CCD camera was also used to bring the AFM cantilever close (within a distance of hundreds of microns) to the substrate by observing the cantilever and its image reflected from the substrate, which is made of either mica or glass. Once the cantilever is brought close to the sample, the lateral position was changed to make it visible through the inverted microscope. At this stage the sample liquid is introduced and the AFM cantilever was further lowered slowing and gently while observing the interference pattern from the fiber for deviation from the stable sinusoidal pattern. The moment the tip contacts the substrate the interference pattern will be distorted. When this happens, the AFM cantilever will be raised by turning back the micrometer screw by a very small amount (less ¼ turn). From this point onwards the closed loop stage can be used to move the substrate up and down in a well defined and controlled manner. The stage has a vertical range of 10 microns.

To bring the tip-substrate distance within the range, the above action may have to be iterated few times.

4.5.2 PROCEDURE

Due to the modular nature of the design, initial preparation of AFM and FCS setups can be performed independently. The preparation of FCS platform involves the following steps:

1) Disassembling the microscope stage.
2) Assembling the stage which houses the AFM setup.
3) Rigidly mounting the base of the AFM (needs care while handling since it's a heavy piece).
4) Adding the extender to the microscope objective and mounting it on the microscope (make sure that the top of the objective is below the closed loop scanner).
5) Rigidly mounting the sample plate onto the scanner.

In order to reduce the use of the FCS laser, it can be turned on only after completing the mounting of the AFM head on the base-plate. When not in use, the AFM head is placed on a stand in the inverted position, which gives easy access to the cantilever holder and slider assembly. Initial preparation of AFM is performed in the inverted position and it involves the following steps:

1) Mounting the appropriate cantilever chip (tip facing up) near the center of the spring clip (before mounting make sure that the fiber is moved as for as possible away and down from the clip).

2) Aligning the fiber to the cantilever with the help of a joystick and CCD camera until a satisfactory interference pattern is obtained.
3) Disconnecting the electrical connection to the head after alignment and placing the head on the base-plate (this is very critical step, and utmost care needs to be taken in order not to damage the fiber or cantilever, or at least knocking it out of alignment).
4) If need be, realigning the fiber to get satisfactory interference pattern.
5) Lowering of the head with help of micrometer screws such that the cantilever and its reflection from the substrate overlap (needs to be done slowly and carefully to avoid crashing the tip and/or fiber onto the substrate).
6) Visualization of the cantilever through the microscope and positioning (with help of the translation stage) the cantilever tip near the center of the field of view.

Once the cantilever is positioned near the center and the fiber alignment is satisfactory, the instrument is ready for the introduction of the sample (liquid). Using a pipette (200 µl at a time) the sample is injected slowly and steadily from the side. After injecting 200 µl check for the interference pattern and for the position of the cantilever in the eye piece and realign if needed. Once realigned continue to inject more liquid. Repeat the process until the entire sample cell is filled with the liquid. After this point, the AFM head is lowered again very slowly (~ ¼ turn at a time) while simultaneously monitoring the interference pattern for any deviation from a sinusoidal pattern. After few turns if there are no deviations, check for the position of the cantilever in the microscope and if need be reposition. Repeat the process until the cantilever barely touches the substrate, at which point the interference pattern will get distorted (it typically becomes flattened on the top). Once that point is reached, immediately lift the head up slowly by

turning the screw in the opposite direction, ~ ½ turn. Now the tip-substrate distance will be approximately within the vertical range (10 μm) of the closed loop scanner. Repeat the process to bring the tip exactly within the range. Realign the fiber to maximize the sensitivity. Once the tip-substrate distance is within 10 microns, the closed loop scanner can be used to change the distances. A LabVIEW routine (National Instruments) is used to operate the electronics that control the scanner. The distance to move and the speed of motion is keyed in by the user, and can be changed at will.

4.6 LIMITATIONS

Our new instrument, despite solving several major challenges, has some limitations when performing FCS experiments when the tip-substrate distance is less than a few microns. The first issue is the inability to obtain clean auto-correlation data, which may be due to the increase in the scattered light coming from the AFM colloidal probe. Different materials (borosilicate, alumina, quartz) were tried for the spherical tip that forms the colloidal probe to decrease scattering. Quartz tips were the most promising, but still the scattering issue persisted. We also tried to sputter-coat quartz spheres with other materials like graphite, TiO_2, and Al_2O_3. Despite obtaining successfully good quality coatings, the issue of backscatter could not be eliminated. The second limitation was an unexpected and fully unexplained artifact that is present in the form of oscillations in the auto-correlation. Figure 4.4.1 shows a typical FCS auto-correlation plot that shows the artifact, which is seen in the form of oscillations in the plot. Such oscillations are seen when the laser is focused on the tip or the substrate, or in-between when the tip-substrate distance is less than few microns. Before the rigid clamping of AFM and FCS stages such oscillations were seen even at larger (tens of microns) separation. In addition,

qualitatively similar oscillations are observed in the auto-correlation function when the entire optic bench is deliberately set into oscillation, see Figure 4.4.1 (open circle). These oscillations occurred at very low frequency (~2 Hz), which corresponds to the resonant frequency of the optic bench. We speculate that the oscillations may be due to a relative a motion of laser focus with respect to the liquid-substrate interface. Similar oscillations in auto-correlation function are also present in scanning-FCS (SFCS), where the laser beam is scanned across the sample[114,115]. The focal volume is non-stationary in SFCS, and this result in oscillations in the auto-correlation function. We tried fitting our data with an expression similar to the ones used in SFCS. However, the parameters obtained from such fits were not realistic. More investigations are needed to identify the source of oscillation, and ways to eliminate them.

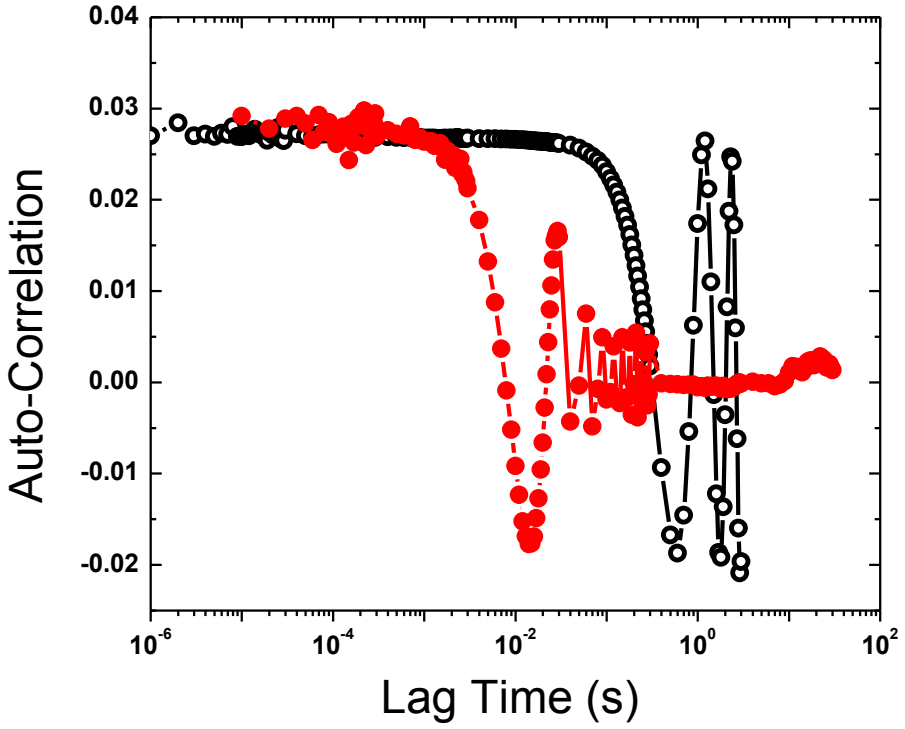

Figure 4.6.1: Oscillations in FCS data when laser focused near sample-substrate interface. High frequency oscillation observed with stationary optic bench (filled circle) and low frequency oscillations seen when the optic bench was oscillated at the resonant frequency (open circle).

Chapter 5

EXPERIMENTS AND RESULTS

In this chapter I describe the different experiments that were performed, and their respective results. This chapter is divided into three sections. The first two sections pertain to nanofluid properties, in bulk and under confinement. The last section describes preliminary experiments and results for an antigen-antibody system.

5.1 BULK DIFFUSION IN NANOFLUIDS

Nanofluids are colloidal dispersion systems, which consists of particles from 1 to 100 nm in size suspended in a base liquid. The term 'Nanofluid' was first coined for a nanoparticle colloidal suspension by Choi in 1995[116-118]. It was originally used in the context of new heat transfer fluids that exhibit superior thermal properties compared to conventional heat transfer fluids with or without particle suspensions. These nanofluids exhibit some intriguing thermal properties [116-123]: They have anomalously high and strongly temperature dependent thermal conductivity. Since heat transfer and mass transfer are analogous, diffusion studies on the nanofluids systems have been undertaken by various groups[117,122,124-129]. However, unlike for thermal properties, the results for mass transport measurements obtained by different groups have been inconsistent. Some groups have reported an enhancement in diffusional motion[122,125,126]. In one experiment more than an order of increase in the diffusion coefficient was observed with the addition of a small amount (< 1% by volume) of nanoparticles in an

aqueous liquid in comparison with pure liquid[125]. The results from reference [10] are shown in Figure 5.1.1.Other groups, however, have reported very less or no enhancement in diffusion for a similar range of volume fraction[127,129,130].

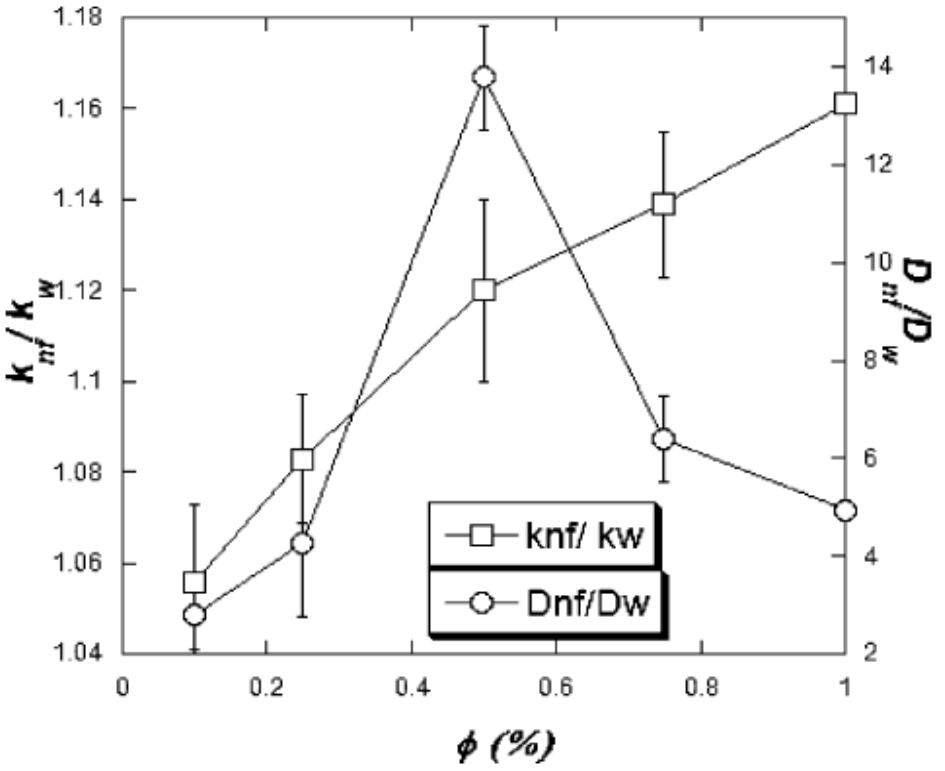

Figure 5.1.1: Normalized diffusion coeeficients and thermal conductivity of 20nm Al_2O_3 nanopartilce based nanofluid from figure 6 of reference [125].

For example, in reference [129], which employed a novel micro-fluidic approach, the results showed no enhancement in diffusion. Figure 5.1.2 and Figure 5.1.3, show the experimental approach and results from reference [129]. In most of the studies mentioned above, except [8,10], the chemical diffusion coefficient[131] of a dye dissolved in the nanofluids was measured using different optical techniques. In one case the concentration profile of a diffusing dye drop

was observed[125,126], and in another, a novel micro fluidic approach was employed where the diffusion of dye from one channel to another was observed[129]. Apart from optical techniques, nuclear magnetic resonance (NMR) was utilized to measure self-diffusion coefficient[127,130,131] in nanofluids[127,130].

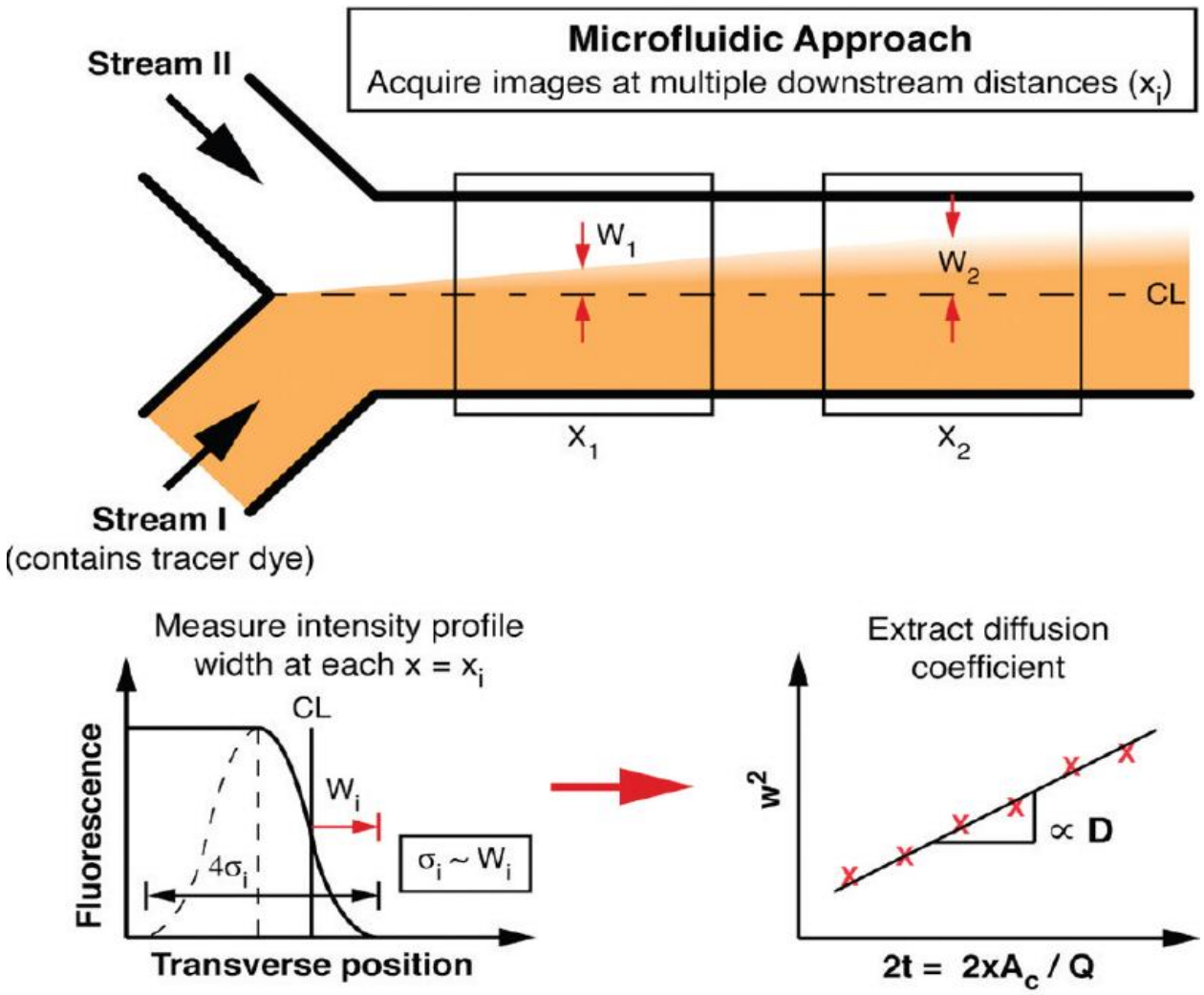

Figure 5.1.2: Experimental schematic of a novel micro-fluid approach to measure diffusion in nanofluid from Figure 1a of reference [129].

Tracer diffusion[131] can be considered similar to self-diffusion provided the tracer particles are similar to the particles that constitute the medium, and there is no strong interaction between the tracer and the surrounding medium. A fluorescent dye or tracer particle is employed in the measurement of both chemical and tracer diffusion.

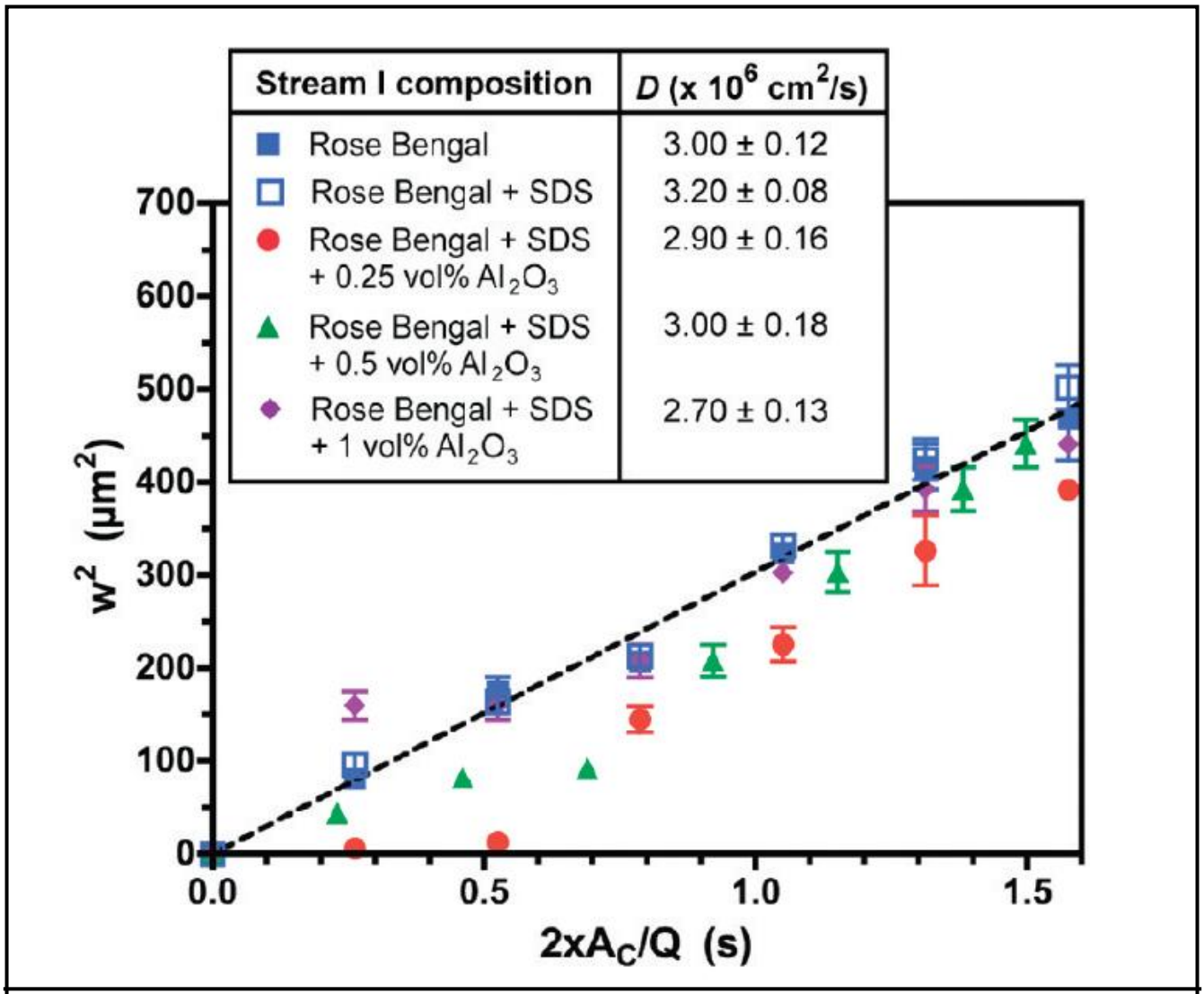

Figure 5.1.3: Results from the micro-fluid approach from Figure 4a of reference [129]. No significant changes in D was noticed (inset table) in the presence of Al_2O_3 nanoparticle.

Due to the presence of a tracer particle in the measurements of both chemical and tracer diffusion, sometimes both tracer and chemical diffusion are interchangeably used in literature, which is inappropriate. The phenomena behind theses two processes are distinct. Chemical diffusion occurs in the presence of a concentration gradient; hence it is essentially a non-equilibrium phenomenon. Both tracer and self-diffusion take place under thermodynamic equilibrium. In this case, the concentration of the tracer is very small, and they are distributed uniformly. The diffusion is due to thermal motion (Brownian motion). Thus a direct measurement of the tracer diffusion coefficient of a dye in nanofluids will enhance our understanding of the mass transfer in nanofluids, because they directly probe local fluctuations which cause diffusional transport in the liquid. However, studies on tracer diffusion in nanofluids are lacking. In this section, I report direct measurements of tracer diffusion in suspensions of two different oxide nanoparticles. Unlike the studies on chemical diffusion, which probe predominantly diffusion in the presence of a chemical gradient, the tracer diffusion studies using the novel FCS technique probe the Brownian motion of a tracer particle. To the best of our knowledge, this is first time fluorescence correlation spectroscopy (FCS) has been applied in this area of research.

Two different nanofluids were studied, each containing a small quantity (~nM) of fluorescent dyes. For both systems, a set of different nanoparticle (NP) concentrations were used. First we report the results of an aqueous colloidal suspension of silica NP (Ludox TM-50, Sigma Aldrich) that contained a small amount of Alexa-488 (Molecular Probes). The second system was an aqueous suspension of alumina NP (Sigma Aldrich) with rhodamine-6G. Since both silica and alumina are charged (negative and positive, respectively), we used different dyes to prevent them from getting adsorbed onto the NPs. If the dyes adsorb to NPs, FCS will probe the

diffusion of the NP rather than the dyes. Dynamic light scattering (DLS) measurement showed no sign of aggregation of the particles. A typical correlation function shown in Figure 5.1.5a fitted well with a single diffusion model. In addition, the particle size distribution shown in Figure 5.1.5b, which was obtained from DLS, was unimodal in nature - indicating the absence any agglomeration. The size of the NP, estimated from transmission electron microscopy (TEM) was found to be consistent with the values provided by the supplier (Figure 5.1.4).

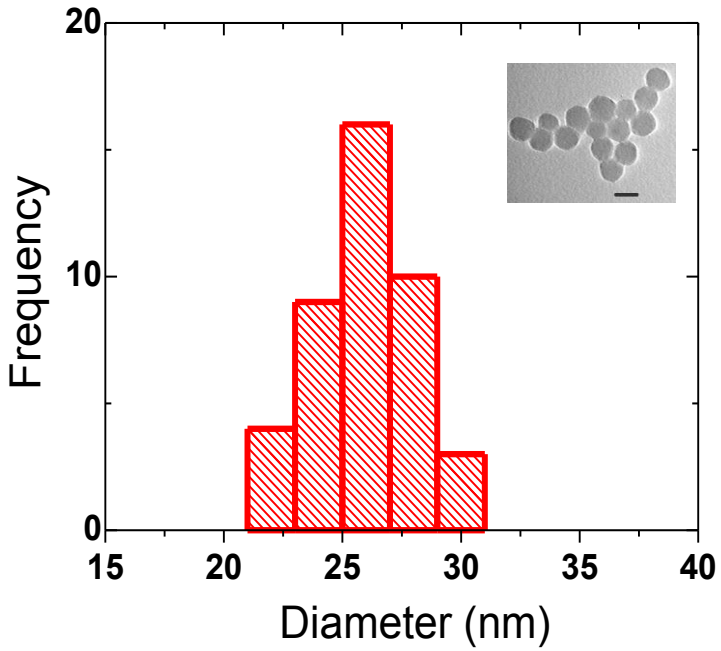

Figure 5.1.4: Size of silica nanoparticle. Histogram of size distribution obtained from TEM with mean diameter of 26 nm. The inset shows a representative TEM micrograph with 20nm scale bar.

The different volume fractions were obtained by diluting the concentrated solution we obtained from the manufacturer. The range of volume fractions was chosen similar to the range

reported by other groups[125,126,129]. In the case of silica-based nanofluids we performed experiments up to a volume fraction of ~ 1.7%. However, in the case of the alumina nanofluid, the volume fraction of the solution obtained from the manufacturer was ~ 1%.

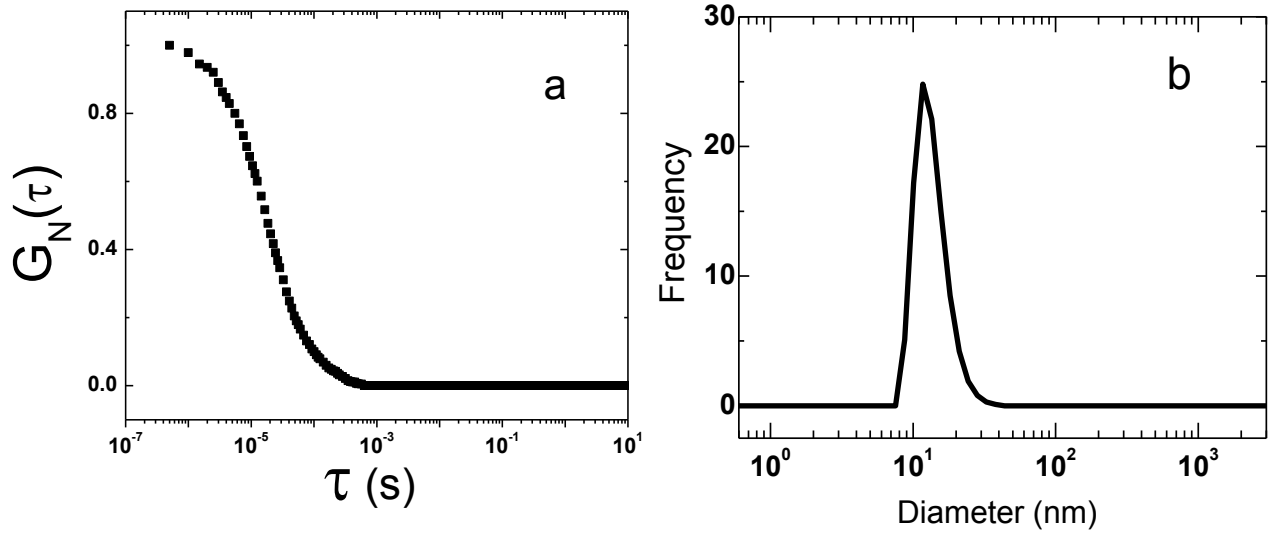

Figure 5.1.5: DLS measurements; (a) A typical correlation function from DLS, which fitted well with single diffusion; (b) Size distribution obtained from DLS measurement (mean diameter 24 nm). The average size provided by the manufacturer was 22 nm.

Both nanofluids showed similar results. A typical normalized autocorrelation, $G_N(\tau)$, curve obtained for Alexa-488 (A488) in pure water and in 0.83 % (by volume) silica nanofluids is shown in Figure 5.1.6. The tracer diffusion coefficient (D) for different concentrations was obtained by fitting the autocorrelation function with a 2d diffusion equation. For the optical setup the length of the laser focus in vertical direction is much more than the width. Hence the fluctuation in the intensity is mainly due the lateral diffusion. This was the rationale for using a 2d model to fit the auto-correlation data. The values of D for different nanoparticle

concentrations were very close to the diffusion coefficient (D_0=458 μm^2/s) of A488 in pure water (Figure 5.1.7a).

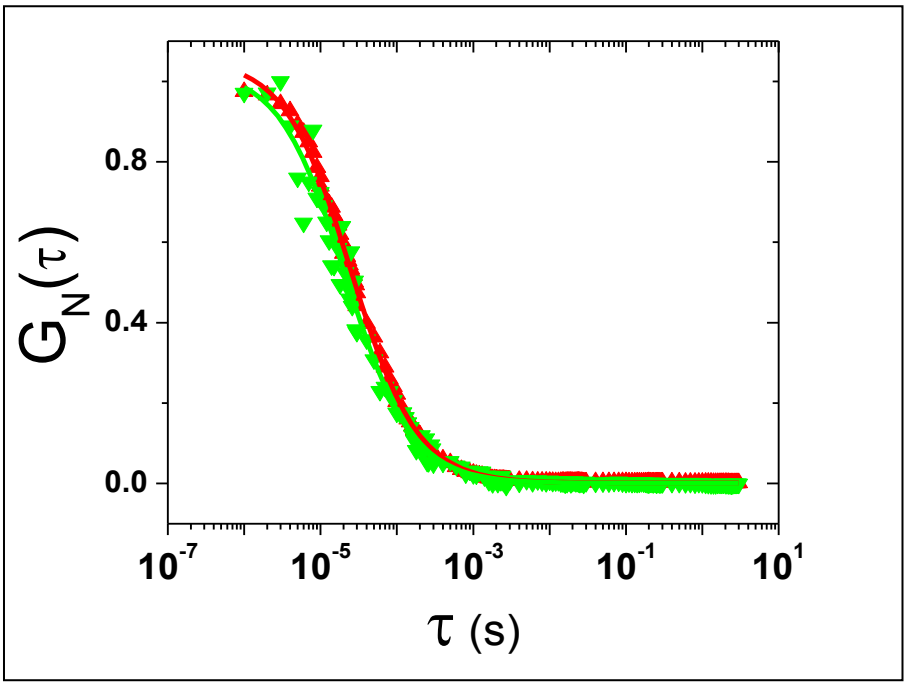

Figure 5.1.6: Normalized intensity – intensity auto-correlation function [$G_N(\tau)$] of A488 in pure water (red triangle) and in 0.83 % (by volume) of silica based nanofluid (green triangle). The solid lines were obtained by fitting the respective data with a model for 2d diffusion. From the fit we obtain the diffusion coefficient (D) for the dye. A488 in Pure Water D= 445 μm^2/s and in 0.83% silica nanofluid D= 470μm^2/s.

Figure 5.1.8a shows a typical normalized auto-correlation function for 0.54% alumina nanofluid and pure water. Similar to the silica nanofluid, we found that values of D for Rh6G at different nanoparticle concentrations were very close to the diffusion coefficient (D_0=280 μm^2/s)

in pure water (Figure 5.1.8b). In order to observe dye-nanoparticle complexes, we used A488 dye with alumina NP based nanofluid since the dye and NPs have opposite charges.

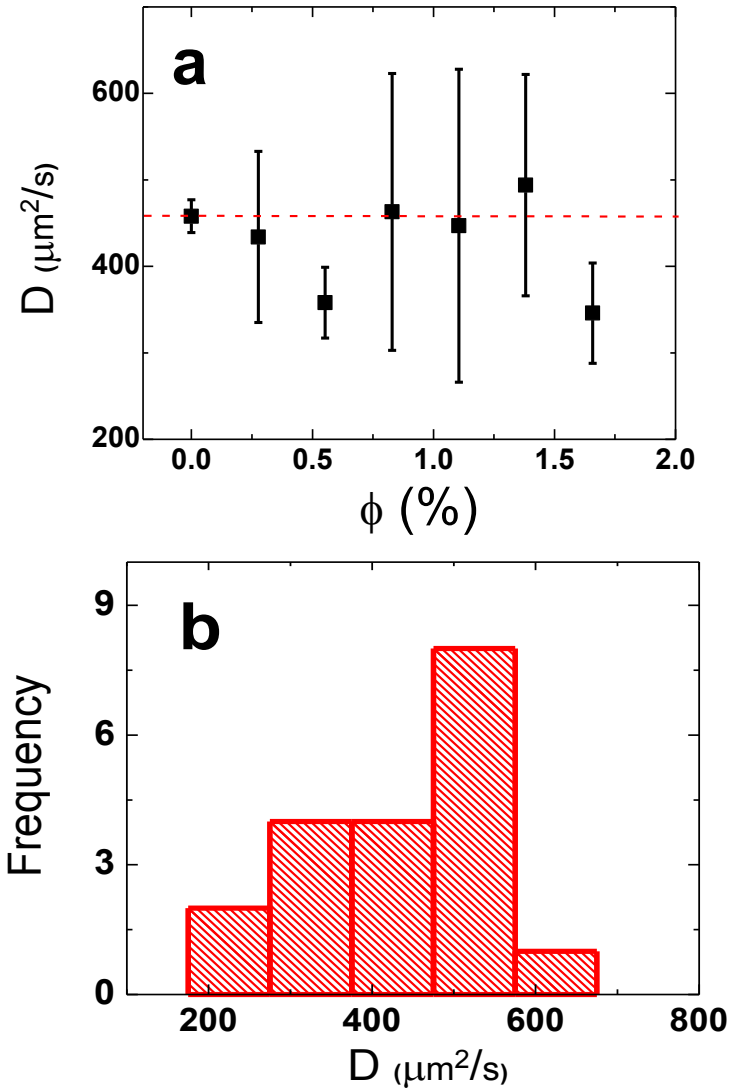

Figure 5.1.7: (a) Distribution of measured diffusion coefficients of A488 in silica based nanofluid for different volume fractions. The error bars are standard deviation obtained from many trials. The dotted line (red) denotes the diffusion coefficient of A488 in pure water, which is 458μm^2/s; (b) Histogram of D obtained from different trials for a nanofluid with volume fraction of 0.83%.

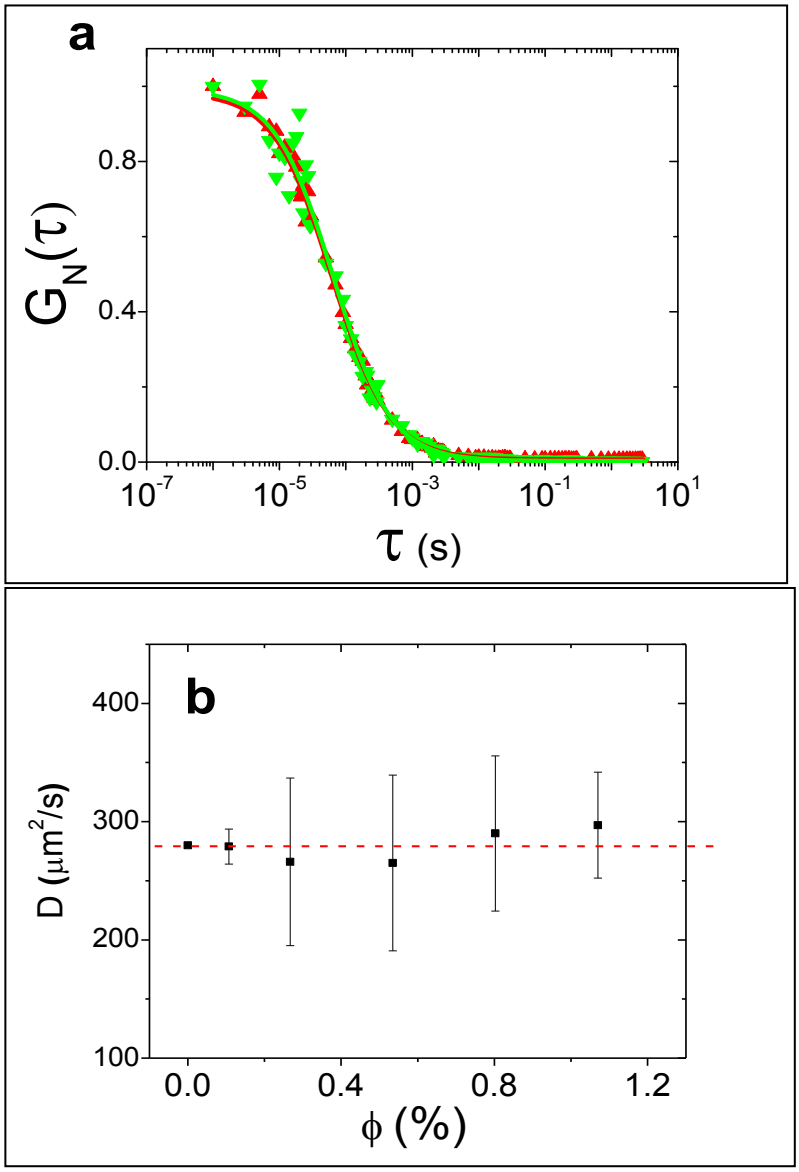

Figure 5.1.8: (a) Normalized intensity – intensity auto-correlation function of Rh6G in pure water (red triangle) and in 0.54 % (by volume) of alumina based nanofluid (green triangle). The solid lines were obtained by fitting the respective data with a model for 2d diffusion. From the fit we obtain the diffusion coefficient (D) for the dye. Rh6G in Pure Water D= 280 mm^2/s and in 0.54% alumina nanofluid D= 268μm^2/s. (b)The distribution of D of Rh6G in silica based nanofluid for different volume fractions. The error bars are standard deviation obtained from many trials. The dotted line (red) denotes the diffusion coefficient of Rh6G in pure water, which is 280μm^2/s.

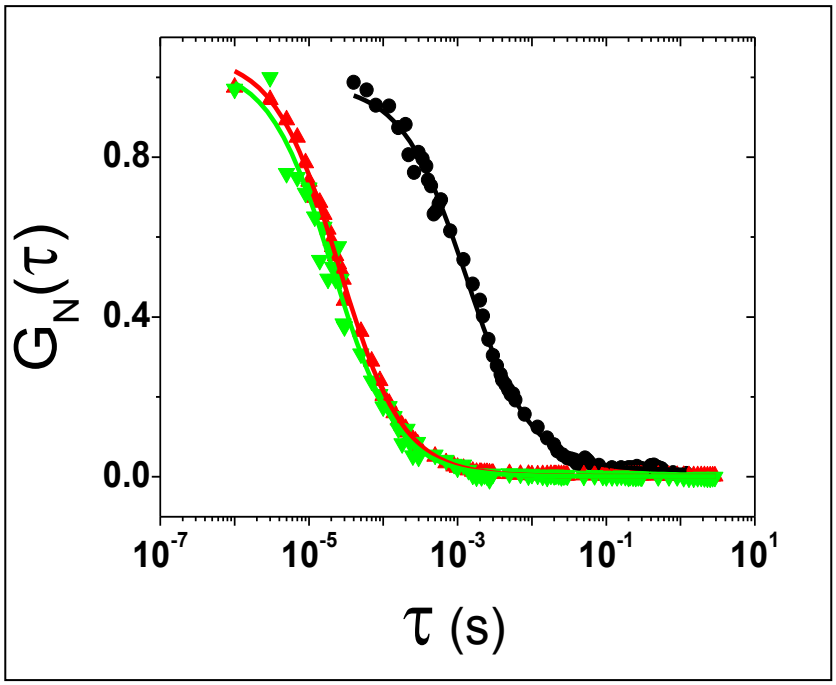

Figure 5.1.9: Normalized intensity–intensity auto-correlation function of A488 in pure water (red triangle), in 0.83 % (by volume) of silica based nanofluid (green triangle) and in 0.54% (by volume) alumina-based nanofluid (black circle). As expected, plot clearly demonstrated that A488 became adsorbed to alumina particle (opposite charge), while the dye freely diffuses in the case of silica particles. This is evident from the shift (towards longer time) of the auto-correlation curve for the alumina based nanofluid with respected to the silica based nanofluid. D's for all the three cases are shown in the inset.

As expected, we observed the diffusion of the dye-nanoparticle complex (see Figure 5.1.9). Moreover, this was the case even after the longest possible averaging time (~45 mins) was used, and was observed at different locations. This shows that there were no freely diffusing dyes. To compare the two different nanofluids with different dyes, we normalized D by dividing by the respective value of the diffusion coefficient, $D_{0,}$ in pure water (280 $\mu m^2/s$ for Rh6G; 458 $\mu m^2/s$ for A488). In Figure 5.1.10 we have plotted the ratios, which clearly demonstrate that the

results for the two different systems were similar in the range of volume fraction we had employed in this study. This trend is consistent with a very recent publication on similar systems, which employed a micro-fluidic setup[129]. However, it is not consistent with some earlier reports, where an enhancement of the diffusion was observed[122,125,126]. The anomalous enhancement was explained on the basis of formation of dye-nanoparticle complex[129]. All the reports on determining the diffusion in nanofluids are based on measuring chemical diffusion. In such measurements, the formation of dye-nanoparticle complexes cannot be directly observed as the measurement is based on observing the spreading of dyes. However, FCS has the specificity, and the required sensitivity, to distinguish the diffusion between free dye and the dye-nanoparticle complex (Figure 5.1.8) as we have demonstrated in this research. This is rendered possible due the large difference (more than an order) between the diffusion of the free dye and the dye-nanoparticle complex. In our results we do not see any enhancement in the diffusion or the presence of the combination of free dyes and dye-nanoparticle complex. If the later was present in the system FCS measurements would have clearly shown the two distinctly diffusion species since the D for the free dye is an order of magnitude more than the dye-nanoparticle complex. However, in our results showed the presence of either free dye or dye-nanoparticle complex, and there was no indication for the presence of two different species (Figure 5.1.9). In addition, for the nanofluids considered in this study there is no significant contribution on the diffusion from sedimentation of the particle due to gravity. The effect of sedimentation, if present, would result in superimposing on the random diffusion a drift velocity in the downward direction. The effect of sedimentation would come in play for colloidal particles of the order of 1 μm in radius (for silica particle in water at room temperature), as calculated from Equation 5, which was obtained by equating the thermal energy (k_BT) with the gravitational potential energy.

$$R^4 = \frac{3k_B T}{4\pi g(\zeta - \zeta_0)} \tag{5.1.1}$$

Here, g is the acceleration due to gravity; ζ and ζ_0 are the density of the colloidal particle (radius R) and the fluid in which the particles are suspended, respectively.

The trend reported here is expected when we consider the fact the volume fraction of the NP was too small to change the dynamics of dye. For the volume fraction we used, the excluded volume model for the diffusion does not predict any significant change in the diffusion coefficient as seen from the equation given below[132]:

$$D = \frac{D_0}{(1 + 2.5\Phi)} \tag{5.1.2}$$

Here, D is the effective diffusion in a concentrated solution with volume fraction Φ, and D_0 is the diffusion coefficient in ultra dilute solution. Equation 5.1.2 is applicable for rigid spherical particles (neutral), with no-slip boundary condition, and when the total volume of the particles is small compared to the volume of the medium[132]. The range of volume fractions in our study is very small, and not expected to significantly alter the value for D in that range as shown in Figure 5.1.10.

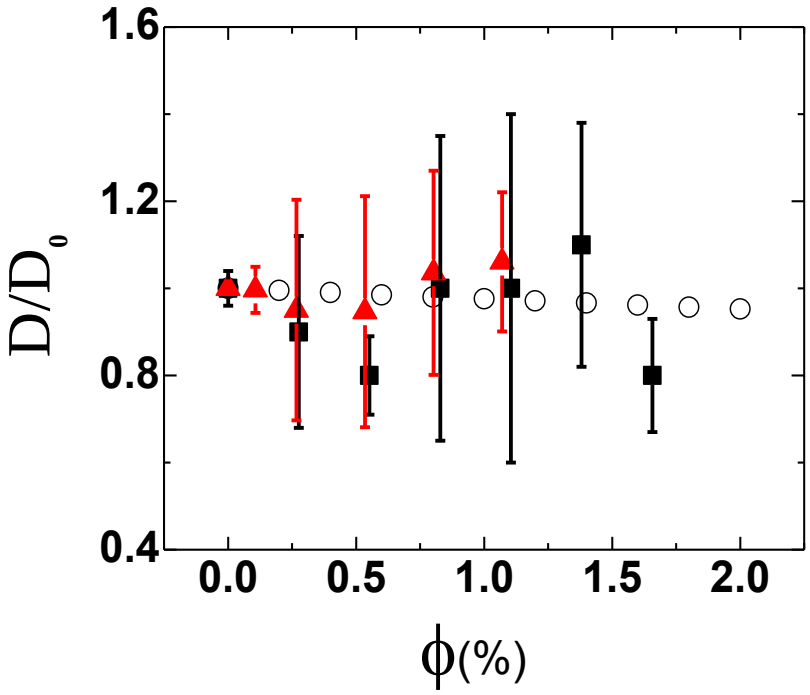

Figure 5.1.10: Distribution of normalized diffusion coefficient (D/D_0) as a function of the volume fractions. Both silica based nanofluid (squares) and alumina based nanofluid (triangles) did not show any significant change in the diffusion coefficient when the volume fraction of the NP was increased. For easy comparison, the prediction of the excluded volume model is shown (circles).

In this section, I have presented results on the direct measurements of the tracer diffusion coefficient of fluorescent dye in different nanofluids using FCS technique. For the two nanofluid systems employed in this study there was no effect of sedimentation on the tracer diffusion owing to the small size of the nanoparticle. In addition, the colloidal suspension is stable and free of any aggregation, which in principle can alter the dynamics of the system. The novel technique employed in our study has the required specificity to distinguish the dynamics of free dyes from

that of the dye-nanoparticle complex. Unlike the measurement of chemical diffusion, our measurements were performed under thermodynamic equilibrium, and hence the Brownian motion in the fluid alone is observed. There is no influence of concentration gradient (of tracer) on these measurements. In the volume fraction range used, we did not observe any significant change in the tracer diffusion coefficient in the nanofluids, and the value of D was very close that of the dye in pure water. Our results indicate that there is no enhancement in the diffusion coefficient in the nanofluid. The trend presented in this section is consistence with the prediction of the excluded volume model. The trend is consistent with a recent paper in which a novel microfluidic approach was employed to study the diffusion in nanofluid [129]. In this paper, the anomalous enhancement observed in earlier works was explained based on possible formation of the dye-nanoparticle complex, which was not directly observed in that work. However, despite the power of FCS to observe directly the presence of any dye-nanoparticle complex, our results showed no indication for the presence of the complex with the free dyes. In addition, we have successfully demonstrated for the first time the application of FCS in understanding the properties of nanofluids.

5.2 NANOFLUID UNDER MICRO-CONFINEMENT

The structure and dynamics of fluids near a solid interface is thought to be different from what we would observe in a bulk system[133]. Studies performed on a wide range of fluid systems, starting from water to bigger organic molecules, and to colloidal systems made up of nanoparticle to micron- size particle, have concluded that the structure and dynamics at a liquid-solid interface is influenced by the discrete nature of the system, and hence the breakdown of

continuum approximation. Thus understanding interfacial properties is important for the advancement of science and technology.

Similar to a fluid close to a single liquid-solid interface, a fluid sandwiched or confined between *two* solid surfaces also behaves significantly different from bulk fluid[3,133]. In particular, unlike in the bulk, liquid near a solid interface has layered structure, which is parallel to the confining surface. This structure dictates the properties of the system. Thus mechanics and dynamics of fluid near the interface are altered from that of bulk behavior. SFA and AFM are two commonly employed techniques to study the structure and mechanics of confined liquid[18,134]. In addition, neutron and X-ray scattering, optics and spectroscopy based experimental studies and theoretical simulations are also performed to understand the structure or dynamics of fluids under confinement[135-139]. Experimentally, confinement-induced ordering in various molecular liquids have been demonstrated for almost three decades[133,134]. Layering has been observed in both polar liquids (water, alcohol) and non polar/inert liquids (OMCTS, TEHOS)[4,18,19,134,140-142]. In addition to molecular liquids, colloidal liquids are found to acquire a structure upon confinement[143].

Colloids are found everywhere in nature (blood, milk), and synthetic colloids are employed practically in all industries, from food industry to semiconductor manufacturing technology. In addition due to their mesoscopic length scales, colloidal systems constitute an ideal model system to study problems in statistical and condensed matter physics[144,145]. Experimental and theoretical studies on colloids under confinement have revealed interesting properties like confinement induced freezing and unusual layered crystalline structures[145-147]. Such layered structures are observed from colloidal particles whose size ranging from tens of nanometer to tens of microns[145]. Thus a colloidal liquid is an ideal system that can be employed

as a test system for our integrated AFM/FCS systems, which will simultaneously probe structure and dynamic of fluid under confinement.

5.2.1 FCS Results

Using a relatively concentrated (compared to the previous section) silica-based nanofluid, FCS experiments under confinement were performed. The operation of the new integrated platform of AFM and FCS was tested to study a nanoparticle colloidal solution under confinement. To the best of our knowledge, this is the first time AFM and FCS had been successfully integrated to perform simultaneous and complementary measurements on liquids under confinement. The FCS measurements were performed while the confinement was simultaneously provided by the colloidal probe attached to the AFM cantilever. A colloidal suspension of silica nanoparticles at volume fraction ~7.3% was used in all the experiments reported in this article/letter. The suspension contained a small amount of labeled silica particles (<0.005% by volume). The solution was prepared from concentrated stock solution obtained from Sigma-Aldrich (Ludox TM-50), which contained spherical silica nanoparticle of ~27.6% by volume. The fluorescently labeled silica particle (Corpuscular, green 20 nm) were obtained from Microspheres-Nanospheres. Dynamic light scattering (DLS) measurement showed no sign of aggregation of the particles (Figure 5.1.5). The size of the NP from transmission electron microscopy and from DLS was found to be consistent with the value provided by the supplier (Figure 5.1.4).

The schematic for the measurement geometry is presented in Figure 5.2.1.1. The vertical confinement was in the order of a few microns, and achieved by precisely controlling the distance between colloidal probe and the sample substrate with the help of the closed loop scanning stage (section 4.1), which has a 10 μm range in the vertical direction.

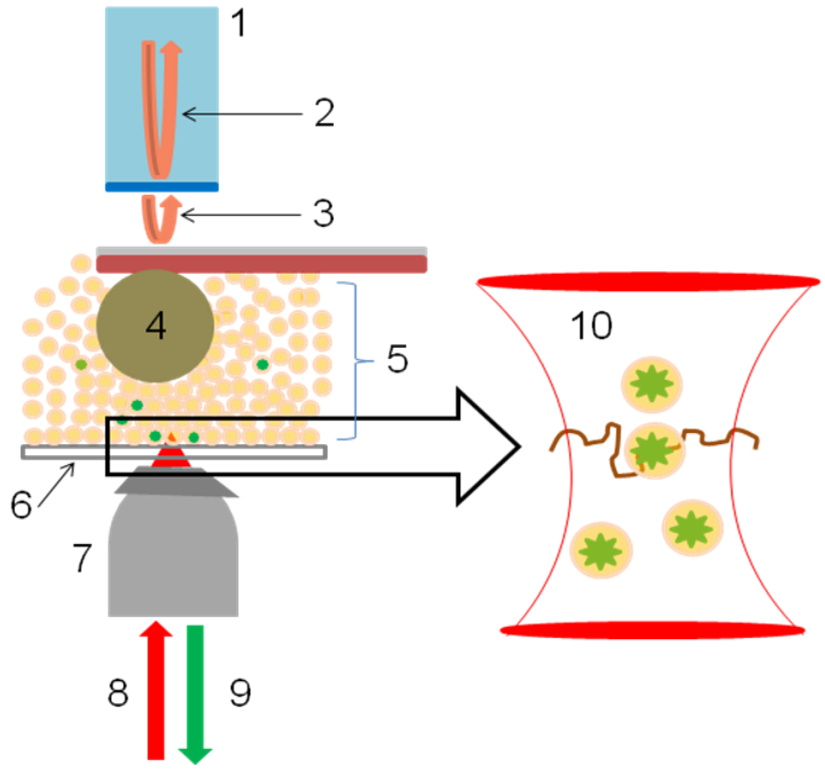

Figure 5.2.1.1: Schematic of our combined AFM-FCS set-up. 1: Single mode optical fiber for interferometric detector, 2: 1310 nm reference laser reflected from TiO_2 coating (blue) at the end of the fiber, 3: Laser reflected from top of the cantilever coated with reflective film (Au or Al) that interferes with the reference beam, 4: Colloidal probe (~25 µm silica), 5: Nanofluid composed of spherical silica nanoparticle, 6: Closed loop scanning stage with sample cell, 7: Objective 63X with NA 0.75, 8: Red laser light for excitation (800 nm), 9: Green light from fluorescence emission, 10: Schematic representation of the laser (800 nm) focus showing the trace of a fluorescently labeled silica nanoparticle.

The results from FCS experiments are presented in Figure 5.2.1.2. The normalized auto-correlation functions, $G_N(\tau)$, for various tip-substrate distances are shown. The diffusion coefficient (D) of the labeled silica nanoparticle was obtained by fitting the auto-correlation data

with equation 3. This plot clearly demonstrates a decrease in D as the tip-substrate distance was reduced. This is evident from the shift (towards longer time) of the autocorrelation curve for smaller tip-substrate distances. For comparison with bulk diffusion coefficient (D_∞ = 6.1 $\mu m^2/s$), a plot of normalized diffusion coefficient (D/D_∞) for various tip-substrate distances is shown in Figure 5.2.1.2 (inset). The error bars are the standard deviation obtained from many trials.

The trend presented in Figure 5.2.1.2 is surprising given the fact that the confinement scale is orders of magnitude larger than the size of the particles, i.e. the confinement is in the micron scale, while the particles are in the nanoscale. In order to find plausible reasons for the intriguing trend reported in Figure 5.2.1.2, different control measurements were undertaken to check for the following:

(i) Effect of particle sedimentation near the substrate.

(ii) Effect of possible charges on either or both of the solid interfaces,
which are employed to confine the nanofluid (single-surface effect).

FCS measurements were performed by focusing the laser near either one of the solid surfaces (colloidal probe and the substrate), while a large separation between the two confining surfaces was maintained. For these experiments the separation was chosen such that the diffusion coefficient of the labeled nanoparticle obtained in the gap was similar to the bulk diffusion coefficient. If sedimentation or the surface effect were responsible for the reduction in the D, presented in Figure 5.2.1.2, then one would expect to observe a reduction in D when only one surface is present. However, no appreciable change in the diffusion coefficient was observed when the laser was focused near either one of the two confining surfaces. In addition, the effect

of sedimentation would come in play for colloidal particles of the order of 1 μm in radius (see §5.1.1 for discussion) Therefore, the sedimentation or the single-surface effect cannot explain the observed change in the D. Hence, it can be concluded that the observed change in the D is most likely due to the confinement of the nanofluid.

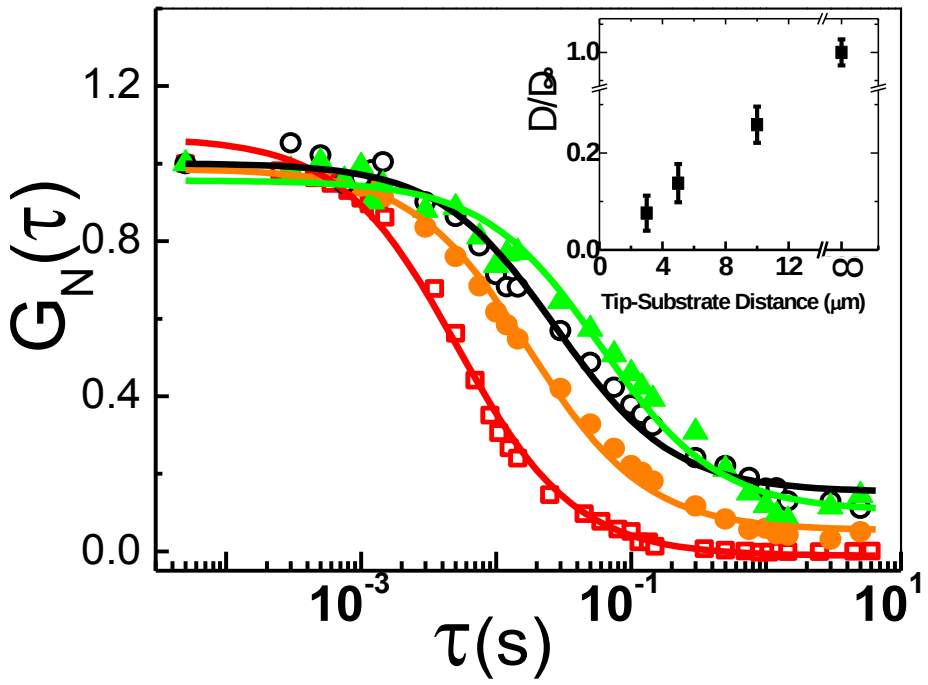

Figure 5.2.1.2: Normalized autocorrelation function of labeled 20nm silica particle in nanofluid in bulk (squares) and for various tip-substrate distances; 10 μm (filled circles), 5 μm (open circles), and 3 μm (triangles). The solid lines were obtained by fitting the respective data with a model for 2d diffusion. This plot clearly demonstrates the decrease in the diffusion coefficient as the tip-substrate distance was reduced. This is evident from the shift (towards longer time) of the autocorrelation curve for smaller tip-substrate distance. Inset shows the plot of normalized diffusion coefficient (D/D_∞) for various tip-substrate distances.

Next, we studied the effect of nanoparticle concentration on the diffusion coefficient using FCS. The volume fraction of the nanoparticle in the dispersion was increased from ~7.3% to ~27.6%, and the diffusion coefficient was measured in bulk solution. The results of the experiments are shown in Figure 5.2.1.3. For easy comparison, diffusion coefficient is normalized with the value obtained for volume fraction 7.3% (corresponds to 17% by mass), which was employed for our micro-confinement experiment.

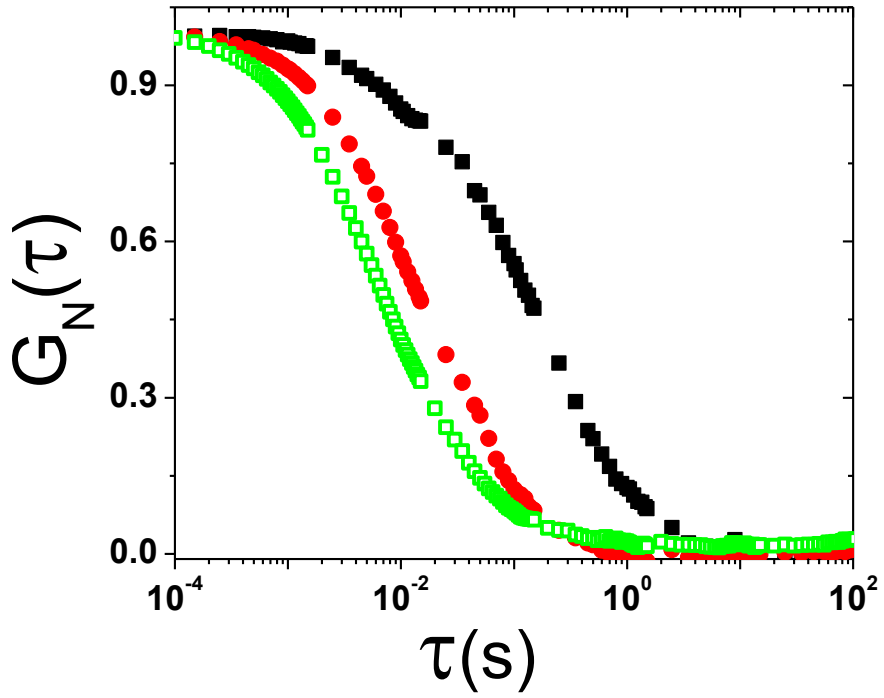

Figure 5.2.1.3: Normalized autocorrelation function of labeled 20nm silica particle in high concentration colloidal dispersion for different mass fractions; 17% (open square), 22% (solid circle) and 50% (solid square).

Figure 5.2.1.4 shows that the changes in the normalized diffusion coefficients are similar for micro-confinement experiments and bulk experiments with higher concentration of the

colloidal dispersion. This suggests that the confinement may result in an increase in the density of the nanoparticles. As mentioned in the introduction, it is well known that confinement induces ordering in liquids, which in turn will result in a reduction in diffusion. However, this cannot explain our data because the scale of confinement should be commensurate with the size of the particles. This is demonstrated in the results from force spectroscopy data obtained from AFM measurements, which are presented in the next section.

Stability of colloidal dispersions, which are made up of charged particles, is explained by well know DLVO theory, which is named after Derjaguin, Landau, Verwey and Overbeek[148]. The theory takes into consideration the electrostatic double layer force and van der Waals force to explain the colloidal stability and phenomenon like flocculation in dispersions. The theory assumes pair-wise interactions between particles. The interactions that the theory considers are (1) long range electrostatic repulsion and (2) short range attraction due to van der Waals force. Since 1940's, DLVO has been successfully applied to explain colloidal phenomena[149]. However, from late 1990's some experimental and theoretical studies on confined or concentrated charged colloidal dispersion have demonstrated the presence of attraction between charged particles, contrary to intuition[150-153]. Such long range attraction is attributed to the breakdown of linearity assumed by DLVO theory, and also due the effect of confinement[151]. The presence of long range attraction between charged particle may lead to an increase in density of particles under confinement, thus resulting in the reduction of the diffusion coefficient. Such an effect may qualitatively explain our results. However, in our experiments the reduction in diffusion occurs at microns scale, where as the effects mentioned occur at the scale of the nanoparticle size. Clearly, more research is needed to fully understand the observation since it is not clear why the confinement at a scale of microns can affect the density of nanoparticles in colloidal dispersion.

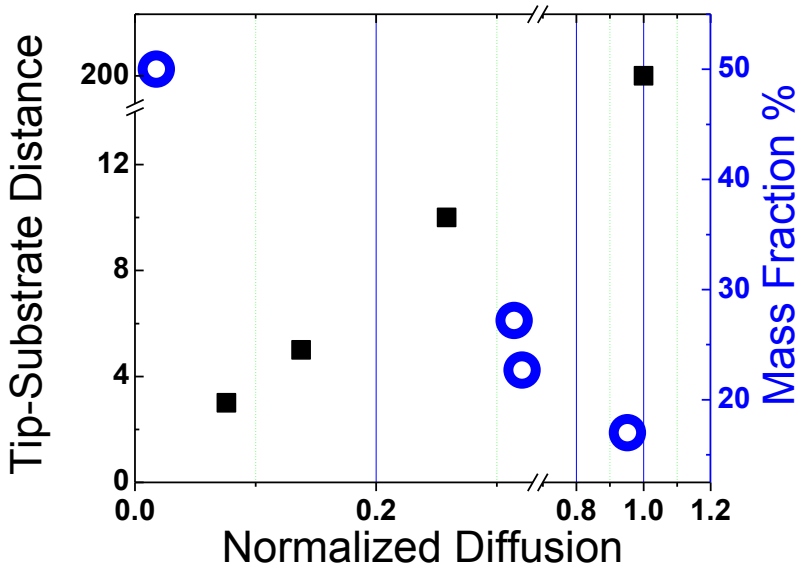

Figure 5.2.1.4: Plot of normalized shows the normalized (with respect to the value for 17%) diffusion coefficient for different mass fractions (blue). Also plotted is the result from the diffusion coefficient measurements for under micro-confinement for comparison.

5.2.2 AFM Results

Our group has a long history of performing force spectroscopy studies using a home-built AFM on various confined liquids [OMCTS, water, TEHOS]. The results from these studies show the presence of oscillations in the stiffness and damping coefficient as the scale of confinement approaches the molecular level. The period of these oscillations in both stiffness and damping coefficients were commensurate with the size of the molecules that constitutes the particular liquid under study. For example, in the case of OMCTS an average peak to peak separation in stiffness or damping coefficient was ~0.9 nm, which is comparable to the diameter of OMCTS

molecules[1]. In recent AFM studies on nano-confined water, the average peak to peak separation obtained was comparable to 0.25 nm, which is the hydrogen bonding distance of water molecules[154,155]. In all these studies, the phase relation between oscillations in stiffness and damping coefficient depended on the rate of confinement. For approach rates below a critical value the stiffness and damping were found to be in-phase, which means the maxima of the stiffness aligned with maxima of the damping coefficients. Such an in-phase behavior implied that the confined liquid behaved like a liquid. The critical speed for OMCTS and water was found to be 0.4 nm/s and 0.6 nm/s[1], respectively. Above the critical speed the oscillations in stiffness becomes out-of-phase, which implies a solid- like mechanical behavior. It will be interesting to study if such properties are exhibited by colloidal liquids as well.

AFM measurements in force spectroscopy mode were undertaken for the concentrated nanofluid system discussed in the previous section. Figure 5.1.3.1 shows the measurement geometry. Figure 5.2.2.1 and 5.2.2.2 show the results for approach speeds of 50 nm/s and 20 nm/s. For both speeds, oscillations in stiffness and damping coefficients were seen. The non-monotonous oscillatory trend presented in these the figures indicates the formation of structure in the colloidal suspension under confinement. However, the phase relation between stiffness and damping was opposite for the two speeds. For an approach speed of 20 nm/s, the stiffness was in-phase with damping, and for 50 nm/s it was out-of-phase. A phenomenological relaxation time (τ) can be calculated from stiffness and damping coefficient, which is given in the following equation:

$$\tau = \frac{C_{ts}}{k_{ts}} \tag{5.2.1}$$

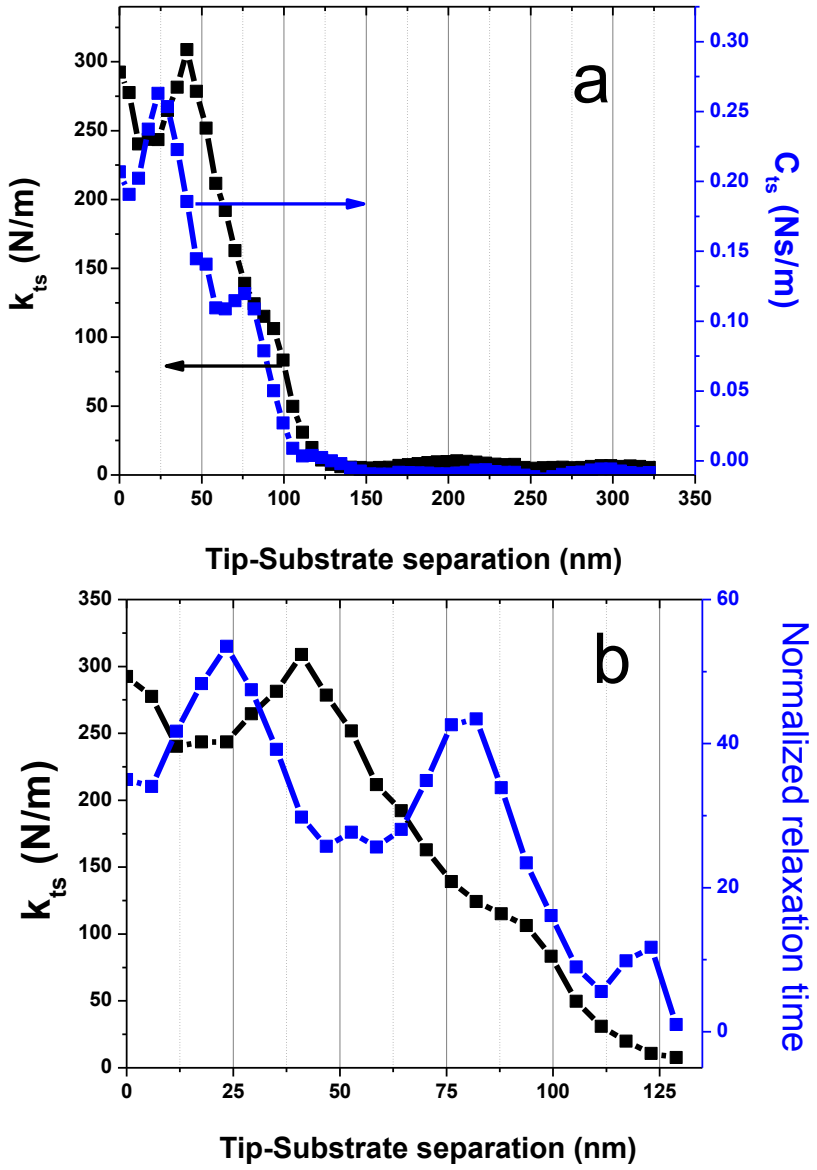

Figure 5.2.2.1: (a) Typical stiffness (K_{ts}) and damping coefficient (C_{ts}) plots from AFM measurement for an approach speed of 50 nm/s. Equation 2.2.6 is used to calculate K_{ts} and C_{ts}, respectively from the amplitude and phase of the cantilever oscillation, which are directly acquired from the AFM, as it approaches substrate. The cantilever stiffness (K_L) used for the above data was 63 N/m. (b) Stiffness and normalized relaxation time as a function of tip-substrate distance. The relaxation time is phenomenologically defined as the ration of C_{ts} and K_{ts}.

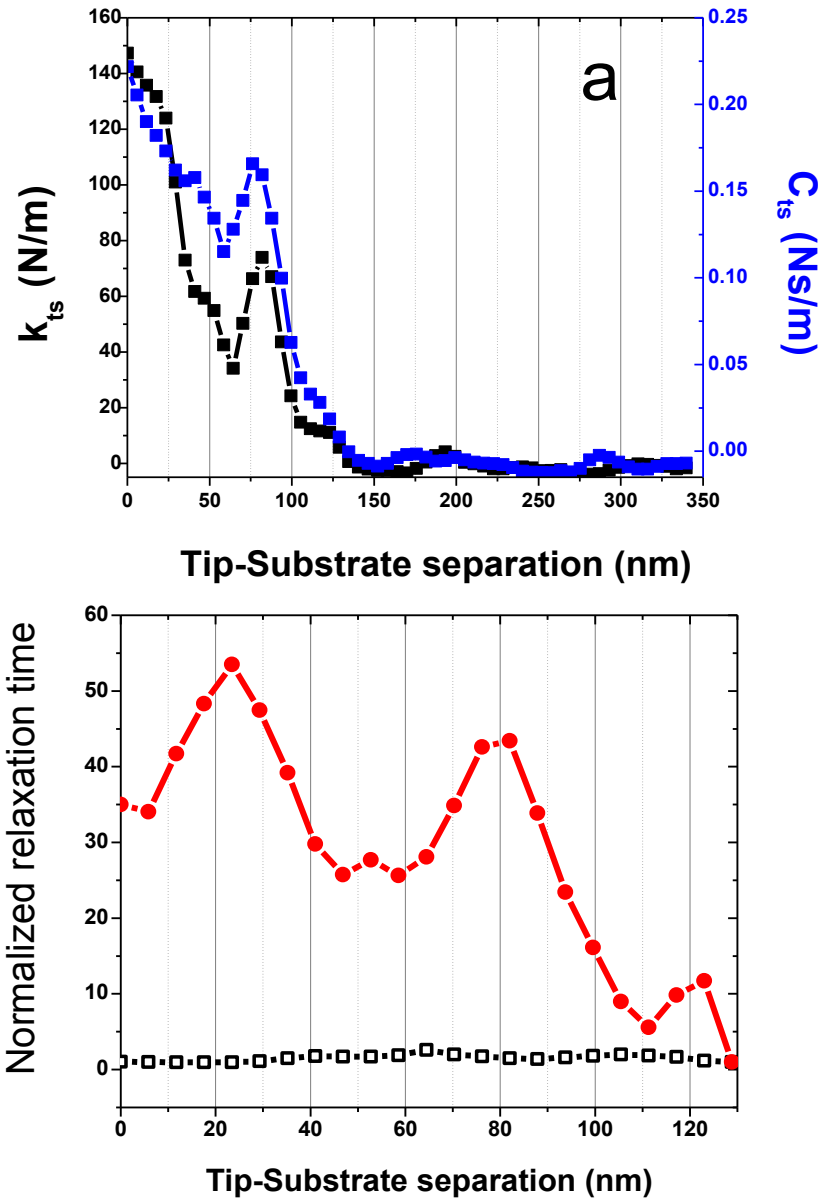

Figure 5.2.2.2: (a) Typical stiffness (K_{ts}) and damping coefficient (C_{ts}) plots from AFM measurement for an approach speed of 20 nm/s. Equation 2.2.6 is used to calculate K_{ts} and C_{ts}, respectively from the amplitude and phase of the cantilever oscillation, which are directly acquired from the AFM, as the tip approaches the substrate. The cantilever stiffness (K_L) used for the above data was 63 N/m. (b) Normalized relaxation time as a function of tip-substrate distance for two different approach speeds; 50nm/s (filled circle) and 20nm/s (open square).

Figure 5.2.2.2b shows that the relaxation time is depended on the approach speed. For high speed, the relaxation time shows oscillations similar to those observed in molecular liquids [water, OMCTS][1,156]. The relative increase in the relaxation time above the bulk value for the confined colloidal liquid is comparable with the value for OMCTS, which in turn was found to be an order greater than water[156]. In reference [136], the significant difference in the relaxation time between OMCTS and water was attributed to the fact that OMCTS is larger and thus more "sluggish", and may order better than water. A similar reasoning may be applicable to the colloidal dispersion, which also show an order of magnitude greater relaxation time compared to water. Surprisingly, unlike the results for molecular liquids, the peak to peak distance for the colloid was ~ 50nm. This distance is approximately *twice* the size of the nanoparticles, which is ~24 nm.

Experimental and theoretical studies on confined charged colloidal dispersion have demonstrated the presence of attraction between charged particles, contrary to intuition. Qualitatively, presence of such an attraction may explain the trend observed in FCS results. However, this notion does not support larger spacing seen in the AFM experiments. It may be possible that the force between particles is repulsive at this length scale, leading to spacing of particles that is *twice* the particle diameter. The layering observed in the AFM results occurs when the tip-substrate distance is of the order of a few particle diameters. However, the reduction in the diffusion observed from FCS experiments occurred at micrometer scale. Thus layering observed in AFM results cannot be responsible for the reduction in diffusion and moreover, the long range attraction that is used to explain the FCS results may not be applicable to the AFM results.

From the nanoparticle volume fraction, the mean inter-particle distance can be estimated using equation:

$$L = 2\left[\sqrt[3]{\frac{\Phi_p}{\Phi}} - 1\right]R \qquad 5.2.2$$

Here, R is the radius of the nanoparticle, L is the average inter-particle distance and Φ_p is the maximum random packing fraction, which 0.638.

The layering indicated by the AFM results is only in the vertical direction and the structural information in the two lateral dimensions cannot be deduced from the results. Nevertheless as a first approximation, the mean inter-particle distance could be assumed to be same as the layer thickness. In this approximation, the volume fraction under confinement estimated from Equation 5.2.2 was found to be 7.9 %, which is close to the bulk volume fraction (7%). This contradicts the results of FCS measurement, which suggest that the confinement may have resulted in an increase in the density of the nanoparticles. Despite these inconsistencies, in principle the results presented demonstrated the successful operation of the novel integrated platform. In Chapter 6, we will suggest future experiments that may help resolve this contradiction.

5.3 DIFFUSION OF LABELED ANTIBODIES

The integrated platform of AFM and FCS is a versatile instrument that can be used to study biological systems at the single molecular level. Recently, in our group a new method was developed to understand the dissociation kinetics of protein-protein interactions measured using AFM single molecule dissociation measurements[157]. With the new platform such AFM

measurements can be combined with FCS to study the dynamics of bio-macromolecules. Some preliminary FCS experiments were performed on an antigen-antibody system, which may be used to label target proteins. Antigen-antibody system is a well known model biological system used to study bio-kinetics, and in addition, it is employed in fields like immunology and enzymology.

FCS measurements to study the diffusion of bio-molecules and their complexes with other molecules are generally performed by labeling the molecule of interest with fluorescence markers. For our studies, two sets of secondary antibody, labeled with different fluorescent dyes [Texas Red and Fluorescein isothiocyanate (FITC)], were employed. All the samples were obtained from WSU medical school. Figure 5.3.1 is a plot of the fluorescent intensity auto-correlation function (ACF) obtained from one of the FCS measurements on secondary AB labeled with FITC in solution.

To obtain the diffusion coefficient (D) the ACF is fitted with a model for 2d diffusion using the following equation.

$$G(\tau) = \frac{G(0)}{\left(1 + 8D\tau / \omega_0^{\,2}\right)} \tag{5.3.1}$$

Results from all the experiments are presented in Figures 5.3.2 and 5.3.3 in the form of histograms. For both types of systems, we observed that D decreases for the complex containing primary and secondary AB. This is expected as D inversely depends on the size of diffusing entity, according to the Stokes-Einstein relation. Using the relation the following expression can be derived:

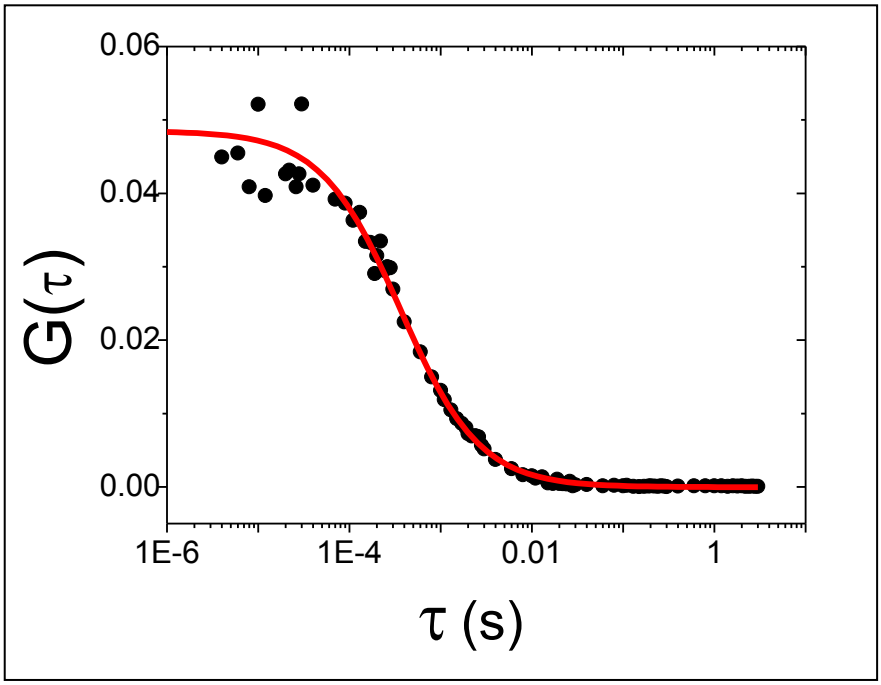

Figure 5.3.1: ACF obtained for FITC labeled secondary AB in solution. The solid line (red) is the fit (using equation 5.3.1) to the data.

Results from all the experiments are presented in Figures 5.3.2 and 5.3.3, respectively, in the form of histograms. For both types of systems, we observed that D decreases for the complex containing primary and secondary AB. This is expected as D inversely depends on the size of diffusing entity, according to the Stokes-Einstein relation. Using the relation the following expression can be derived:

$$R_{unknown} = \frac{R_{FITC} D_{FITC}}{D_{unknown}} \qquad (5.3.2)$$

In the case of FITC labeled system, the D for free FITC in same buffer and size of FITC molecule (0.6 nm) are known. Using these values, from Equation 5.3.2 we obtained the hydrodynamic of radii of secondary AB and complex of primary and secondary AB. The radius for the complex was 13 nm, an increase by a factor ~2 from 7.3 nm for the secondary AB, clearly indicating the formation of the complex. These preliminary experiments were performed to check applicability of our FCS setup to study bio-systems.

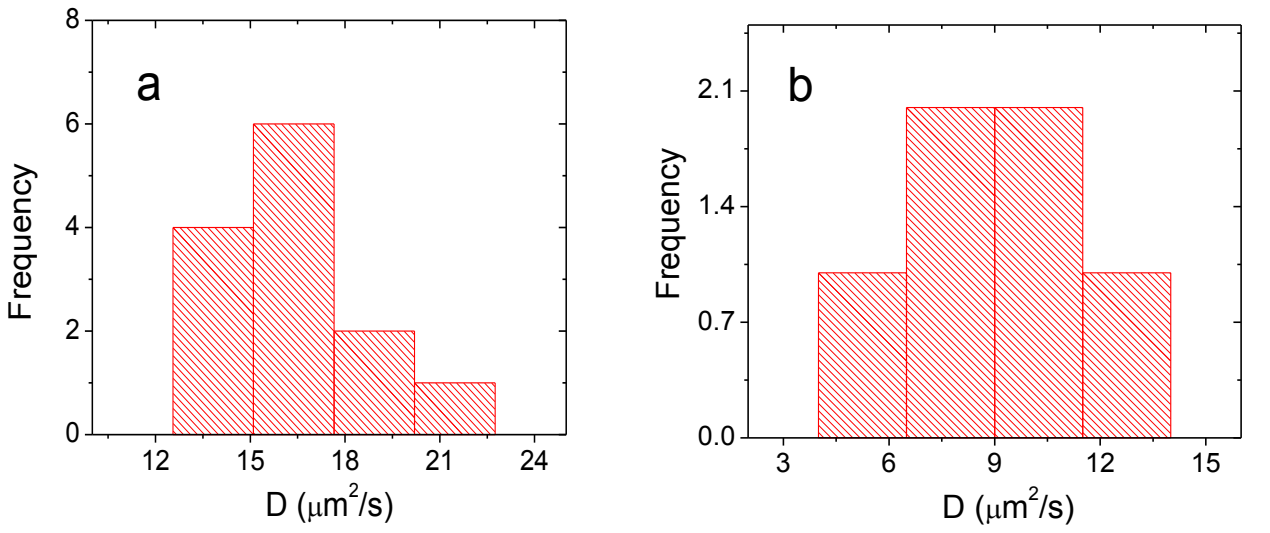

Figure 5.3.2: Histogram showing the distribution of diffusion coefficient (D) obtained from FCS experiment with FITC labeled system. (a) Secondary anti-body, mean D=16.1 μm^2/s; (b) Complex of primary and secondary anti-body, mean D=8.8 μm^2/s.

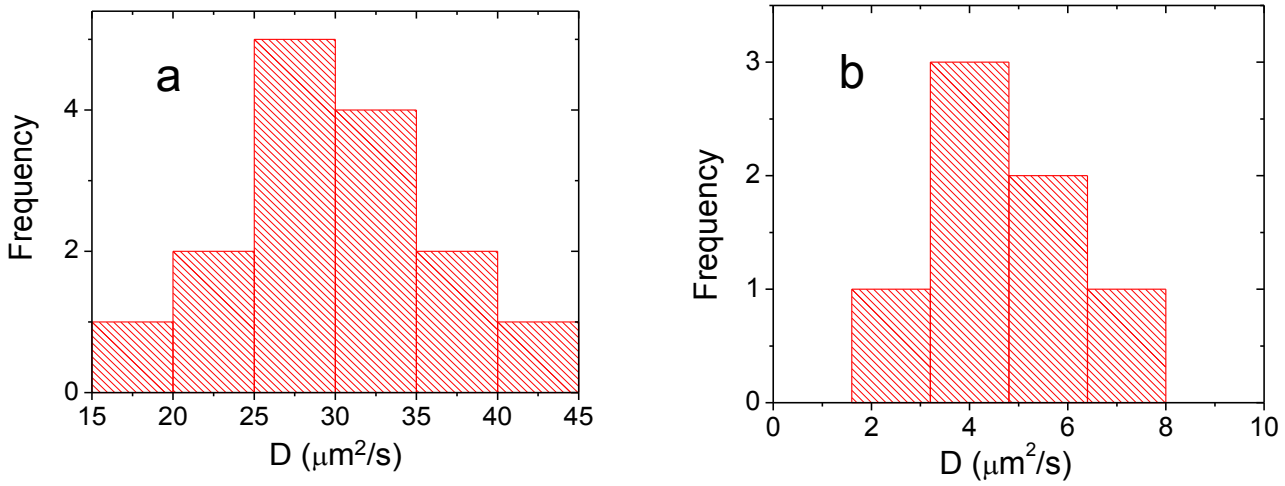

Figure 5.3.3: Histogram showing the distribution of diffusion coefficient (D) obtained from FCS experiment with Texas Red labeled system. (a) Secondary anti-body, mean D=28.8 μm^2/s; (b) Complex of primary and secondary anti-body, mean D=4.8 μm^2/s.

Chapter 6

SUMMARY AND FUTURE DIRECTION

In this final chapter, I present a brief summary of my thesis work, and describe directions for future research with the novel integrated platform constructed during this thesis work. Some of the proposed future experiments need to be performed to fully understand and explain the intriguing results presented in the previous chapter.

6.1 SUMMARY

A new fiber interferometric detection based AFM was constructed, and was successfully integrated with an existing custom-made FCS setup based on an inverted microscope. The main design of this new AFM is similar to the high sensitive AFM instrument previously built in our group. In order to integrate the AFM with an inverted optical stage, significant modifications to the design and implementation were needed. With the novel integrated platform, mechanics and dynamics of liquids can be studied simultaneously. In our setup, the confinement of liquid on a glass substrate is achieved by the colloidal probe of the AFM, and a thin substrate made up of mica (0.15mm think) or silica (#1 microscope slide). Some of the newer features of the new AFM are listed below:

3) A closed loop scanning stage (from Physik Instrumente) is used for lateral motion of the sample and its coarse approach toward the tip.
4) The fine approach is performed by a tube piezo (ID 1”) to which the AFM is attached.
5) Both the cantilever and the fiber positioner are attached to the fine approach piezo, and

thus the fine approach of the tip can be achieved without loss of fiber alignment.

6) The fiber employed in the AFM was coated with TiO_2 using the novel process developed based on MOD.

The novel coating method was based on metal-organic decomposition (MOD) technique, which is a well-known method in solid-state thin film technology. A thin film of TiO_2 deposited at the end of the fiber helps to improve the resolution of the detection system. We found that TiO_2 may provide a better choice as the optical reflectivity of TiO_2 is similar to that of Si in the wavelength range we employ, and as an oxide it is not prone to undergo further oxidation in liquids. The quality and robustness of TiO_2 coated fibers were tested by immersing them in various liquids, while their reflectivity was monitored. Unlike the Au/Si coated fibers, which we used previously, the TiO_2 coated fibers showed no change in the reflectivity even for prolonged immersion (24 hours). The thin film coating using the new method was found to be of sufficient quality to be employed for high resolution fiber-optic interferometry. The AFM results presented in this work were obtained using the fiber coated by this method. This coating technique is much faster and easier than conventional thin film coating techniques, and yields results that are comparable or better than can be achieved with sputtering or thermal evaporation.

The functionality of the integrated platform was demonstrated by studying a silica nanoparticle (~20 nm diameter) based colloidal liquid. The dynamics and structure of the dispersion under confinement were studied using FCS and AFM. Results from the two instruments showed the effect of confinement. However, the results were different and

unexpected. While AFM results indicated the influence of confinement at nanoscale, the FCS results showed that the dynamics was affected at micro-scale. Diffusion coefficient (D) of nanoparticle measured by FCS decreased by more than 3X from the bulk value even at a tip-substrate distance of 10 micron, and decreased further with the reduction of the tip-substrate distance. More than an order decrease in the D was observed at a tip-substrate distance of 3 micron. Due to experimental difficulties that created artifacts, reliable FCS data could not be obtained for confinement of less than 3 micron. Stiffness and damping coefficient were measured by AFM on the confined colloidal for two different approach speeds of the tip towards the surface. For both speeds, oscillations in stiffness and damping coefficients were seen when the tip-substrate distance was less than 100 nm. However, the phase relation between stiffness and damping was opposite for the two speeds. For an approach speed of 20nm/s the stiffness was in-phase with damping, and for 50nm/s it was out-of-phase. At high speed, the relaxation time calculated from stiffness and damping showed oscillations, which were absent for the slower approach speed. These observations indicate the presence of structure in the dispersion under confinement, which is similar to the trend noticed from previous AFM studies on various molecular liquids. However, unlike the results from molecular liquids, for the colloidal dispersion the peak-to-peak distance is ~ 50nm, which is *twice* the size of the particles, which is ~24 nm. More experiments are needed to confirm and fully understand these results. Nevertheless, these results successfully demonstrate the functionality of the newly built integrated platform of AFM and FCS.

During the course of the research, application of FCS to study the dynamics of nanofluids was successfully demonstrated. To the best of our knowledge, this is the first time FCS was

employed to study nanofluids. Nanofluids exhibit some intriguing thermal properties, and have great potential to increase the efficiency in various heat technological applications in micro- and nano- technology. Recent studies on the mass transport behavior in nanofluids have yielded some interesting but controversial results. Two different nanofluids containing a small quantity (~nM) of fluorescent dyes were studied by employing two-photon FCS. Direct measurements of the tracer diffusion coefficient of the fluorescent dye in different nanofluids were obtained using FCS technique. The experiments were performed under thermodynamic equilibrium, and hence the Brownian motion in the fluid alone was observed. A silica nanoparticle based nanofluid containing fluorescent dye Alexa488 in nanomolar concentration, and an alumina nanoparticle containing nanomolar concentration of fluorescent dye rhodamine 6G were the two dispersions used. In the volume fraction range we used, we did not observe any significant change in the tracer diffusion coefficient in the nanofluids, and the value of D was very close that of the dye in pure water. Our results indicate that there is no enhancement in the diffusion coefficient in the nanofluid. The trend presented in this thesis is consistent with the prediction of the excluded volume model. The trend is consistent with a recent paper in which a novel microfluidic approach was employed to study the diffusion in nanofluid [129]. In this paper, the anomalous enhancement observed in earlier works was explained by the authors based on possible formation of the dye-nanoparticle complex, which was not directly observed in that work. However, despite the power of FCS to observe directly the presence of any dye-nanoparticle complex, our results showed no indication for the presence of the complex with the free dyes. In the case where the dye-nanoparticle complex was observed, we did not find any indication for the presence of free dyes. In other words, in the concentration range (of both dye and nanoparticle) employed in this work we observed that the presence of free dyes and the complex

was mutually exclusive. In addition, the application of FCS in understanding the dynamics of nanofluids was successfully demonstrated.

6.2 FUTURE DIRECTION

The novel combined AFM and FCS platform we successfully constructed has great potential to study various soft matter systems, like colloidal dispersions. In addition, because of the inverted geometry of the microscope platform and the ease of AFM use in liquid environment the new platform is attractive for studying biological systems. In this section, I present some possible future directions for the research that could be pursued.

6.2.1 CONFINED COLLOIDAL DISPERSIONS

The colloidal dispersion employed in this research displayed some intriguing behavior under confinement. AFM results demonstrated the presence of layered structure of the colloid under nano-scale confinement. On the other hand, FCS results on the dynamics of the colloidal systems showed significant reduction of the diffusion coefficient even at micro-scale confinement. Moreover, FCS results seemed to indicate that the slow-down of the diffusional dynamics was due to an increase in particle concentration, which may be a result of the micro-confinement. However, in our AFM measurements, which were performed at nanoconfinement, we found that the concentration of the colloid did not differ much from the bulk concentration. Thus the AFM results seem to contradict the notion that an increase in particle concentration was responsible for the diffusional slow-down seen in the FCS results. In order to solve this puzzle, we need to alter the bulk concentration and the interparticle forces, and repeat the FCS and AFM measurements for a reasonable range of these parameters. In particular, some of the future experiments needed are:

1) In this thesis work, AFM experiments were preformed with only two different approach speeds, and hence in order to establish the generality, studies need to performed for a larger range of speeds.
2) Another parameter to vary is the concentration of the colloidal liquid. In the present study only one concentration was employed in both AFM and FCS experiments. In future experiments (both AFM and FCS) the concentration can be varied, and AFM experiments can be performed for different speeds for each concentration. Such experiments needed to be performed to check for the effect of concentration on the behavior of the colloidal suspension under confinement.
3) The properties of colloids are affected by pH and ionic strength of the dispersion. These parameters were not varied in the present study. In order to investigate the influence of ionic strength or pH on the colloids under confinement, experiments need to be performed by varying these parameters.
4) To check for the universality, all the above mentioned variations needs be performed with colloidal dispersions made up of particles of different sizes, and made of different materials.
5) Influence of AFM tip size on the mechanics of confined liquid was recently investigated in our group[155]. The stiffness and damping coefficient appeared to depend linearly on tip size. Such a linear dependency of damping on tip radius indicated a deviation from squeeze damping model, which predicts a quadratic dependency. Similar studies can be undertaken in future on colloidal system to investigate the effect of tip size on the mechanical properties of colloids under confinement.

6) Eventually, experimental studies on more complex colloids, which are heterogeneous or polydispersed, can be undertaken in future.

6.2.1 OTHER SOFT MATTER SYSTEMS

The new integrated platform can be employed to study the structure, dynamics and kinetics of various soft matter systems, such as polymers and biological systems. Unlike the particles, polymers are flexible and hence their confirmation depends strongly on the environment. Similar to the experiments mentioned in the previous section, studies on polymers dissolved in a solvent can be undertaken to understand their structure and dynamics near solid interface. Force spectroscopy and diffusion studies can be performed on bio-molecules, and their complexes that are present on the membranes on living cells in physiological state. For example, there are domains (like lipid rafts) present in the membrane whose structure and mobility are different from other regions of the cell membrane. The mechanics and dynamics of domains can be investigated using the novel integrated platform. Such studies will enhance our understanding of the structure, and function of different parts of the cellular membrane, which play an important role in varied processes, like endocytosis, exocytosis, and antigen recognition.

REFERENCES

(1) Matei, G., Wayne State University, 2007.

(2) Feynman, R. P. *Six Easy Pieces: Essentials of Physics Explained by Its Most Brilliant Teacher*; Perseus Books, : Reading, Massachusetts, U.S.A., 1994.

(3) Bhushan, B.; Israelachvili, J. N.; Landman, U. *Nature* **1995**, *374*, 607-616.

(4) Patil, S.; Matei, G.; Grabowski, C. A.; Hoffmann, P. M.; Mukhopadhyay, A. *Langmuir* **2007**, *23*, 4988-4992.

(5) Magde, D.; Elson, E. L.; Webb, W. W. *Biopolymers* **1974**, *13*, 1-28.

(6) Magde, D.; Elson, E. L.; Webb, W. W. *Biopolymers* **1974**, *13*, 29-61.

(7) Burns, A. R. *Langmuir* **2003**, *19*, 8358-8363.

(8) Burns, A. R.; Frankel, D. J.; Buranda, T. *Biophysical Journal* **2005**, *89*, 1081-1093.

(9) Micic, M.; Hu, D. H.; Suh, Y. D.; Newton, G.; Romine, M.; Lu, H. P. *Colloids and Surfaces B-Biointerfaces* **2004**, *34*, 205-212.

(10) Peng, L.; Stephens, B. J.; Bonin, K.; Cubicciotti, R.; Guthold, M. *Microscopy Research and Technique* **2007**, *70*, 372-381.

(11) Shaw, J. E.; Oreopoulos, J.; Wong, D.; Hsu, J. C. Y.; Yip, C. M. *Surface and Interface Analysis* **2006**, *38*, 1459-1471.

(12) Salvatore Chiantia, N. K., Jonas Ries, and Petra Schwille *Biophysical Journal* **2006**, *90*, 4500–4508. .

(13) Demirel, A. L.; Granick, S. *Journal of Chemical Physics* **2001**, *115*, 1498-1512.

(14) Granick, S. *Physics Today* **1999**, *52*, 26-31.

(15) Israelachvili, J. N. *Intermolecular and surface forces*; Academic Press London, 1991.

(16) Mukhopadhyay, A.; Zhao, J.; Bae, S. C.; Granick, S. *Review of Scientific Instruments* **2003**, *74*, 3067-3072.

(17) Mukhopadhyay, A.; Zhao, J.; Bae, S. C.; Granick, S. *Physical Review Letters* **2002**, *89*, -.

(18) Patil, S.; Matei, G.; Oral, A.; Hoffmann, P. M. *Langmuir* **2006**, *22*, 6485-6488.

(19) Patil, S.; Matei, G.; Dong, H.; Hoffmann, P. M.; Karakose, M.; Oral, A. *Review of Scientific Instruments* **2005**, *76*, -.

(20) Mukhopadhyay, A.; Bae, S. C.; Zhao, J.; Granick, S. *Physical Review Letters* **2004**, *93*, -.

(21) Mukhopadhyay, A.; Zhao, J.; Bae, S. C.; Granick, S. *Phys. Rev. Lett.* **2002**, *89*, 136103.

(22) Matei, G.; Jeffery, S.; Patil, S.; Khan, S. H.; Pantea, M.; Pethica, J. B.; Hoffmann, P. M. *Review of Scientific Instruments* **2008**, *79*, -.

(23) Subba-Rao, V.; Sudakar, C.; Esmacher, J.; Pantea, M.; Naik, R.; Hoffmann, P. M. *Rev Sci Instrum.* **2009**, *80*, 115104.

(24) Binnig, G.; Rohrer, H. *Helvetica Physica Acta* **1982**, *55*, 726-735.

(25) Binnig, G.; Quate, C. F.; Gerber, C. *Physical Review Letters* **1986**, *56*, 930-933.

(26) Sarid, D. *Scanning Force Microscopy: With Applications to Electric, Magnetic, and Atomic Forces*; Revised Edition ed.; Oxford University Press: New York, 1994.

(27) Rugar, D.; Mamin, H. J.; Guethner, P. *Applied Physics Letters* **1989**, *55*, 2588-

2590.

(28) Patil, S. V.; Hoffmann, P. M. *Adv. Eng. Mater.* **2005**, *7*, 707-712.

(29) Hoffmann, P. M. *Appl. Surf. Sci.* **2003**, *210*, 140-145.

(30) Mate, C. M. *Wear* **1993**, *168*, 17-20.

(31) Marti, O. *Microscopy Microanalysis Microstructures* **1993**, *4*, 429-440.

(32) Gould, S. A. C.; Drake, B.; Prater, C. B.; Weisenhorn, A. L.; Manne, S.; Kelderman, G. L.; Butt, H. J.; Hansma, H.; Hansma, P. K.; Magonov, S.; Cantow, H. J. *Ultramicroscopy* **1990**, *33*, 93-98.

(33) Terris, B. D.; Stern, J. E.; Rugar, D.; Mamin, H. J. *Physical Review Letters* **1989**, *63*, 2669.

(34) Martin, Y. A., David W.; Wickramasinghe, H. Kumar; *Applied Physics Letters* **1988**, *52*, 1103 - 1105

(35) Terris, B. D. S., J. E.; Rugar, D.; Mamin, H. J.; *Journal of Vaccum Science and Technology* **1990**, *8*, 374-377.

(36) Stern, J. E. T., B. D.; Mamin, H. J.; Rugar, D.; *Applied Physics Letters* **1988**, *53*, 2717 - 2719

(37) Saurenbach, F. T., B. D.; *Applied Physics Letters* **1990**, *56*, 1703 - 1705

(38) Takeshi Tsuyuguchi, T. U., Takahiro Okusako, Yasuhiro Sugawara, Seizo Morita, Yoshiki Yamanishi and Takahiko Oasa *Japanese Journal of Applied Physics* **1994**, *33*, L1046-L1048.

(39) Franke, K.; Besold, J.; Haessler, W.; Seegebarth, C. *Surface Science* **1994**, *302*, L283-L288.

(40) Takayuki Uchihashi, Y. F., Yasuhiro Sugawara, Seizo Morita, Akihiko Nakano1, Tohru Ida and Takao Okada *Japanese Journal of Applied Physics* **1994**, *33*, L1562-L1564.

(41) Weaver, J. M. R. W., H. K.; *Journal of Vaccum Science and Technology* **1991**, *9*, 1562-1565.

(42) Weaver, J. M. R. A., David W.; *Journal of Vaccum Science and Technology* **1991**, *9*, 1559 - 1561

(43) Nonnenmacher, M.; O'Boyle, M.; Wickramasinghe, H. K. *Ultramicroscopy* **1992**, *42-44*, 268-273.

(44) Seizo Morita, T. I., Yasuhiro Sugawara, Takao Okada, Syuzo Mishima, Syozo Imai and Nobuo Mikoshiba *Japanese Journal of Applied Physics* **1989**, *28*, L1634-L1636.

(45) Huang, Y. J.; Slinkman, J.; Williams, C. C. *Ultramicroscopy* **1992**, *42-44*, 298-303.

(46) Yasutake, M.; Aoki, D.; Fujihira, M. *Thin Solid Films* **1996**, *273*, 279-283.

(47) Ebert, P.; Urban, K. *Ultramicroscopy* **1993**, *49*, 344-353.

(48) Martin, Y. R., D.; Wickramasinghe, H. K.; *Applied Physics Letters* **1988**, *52*, 244-246.

(49) Martin, Y. W., C. C.; Wickramasinghe, H. K.; *Journal of Applied Physics* **1987**, *61*, 4723 - 4729

(50) Martin, Y. W., H. K.; *Applied Physics Letters* **1987**, *50*, 1455 - 1457

(51) Mate, C. M.; McClelland, G. M.; Erlandsson, R.; Chiang, S. *Physical Review Letters* **1987**, *59*, 1942.

(52) García, R.; Pérez, R. *Surface Science Reports* **2002**, *47*, 197-301.

(53) Giessibl, F. J. *Reviews of Modern Physics* **2003**, *75*, 949.

(54) Gratz, A. J.; Hillner, P. E. *Journal of Crystal Growth* **1993**, *129*, 789-793.

(55) Farquhar, M. L.; Wincott, P. L.; Wogelius, R. A.; Vaughan, D. J. *Applied Surface Science* **2003**, *218*, 34-43.

(56) Kleber, C.; Hilfrich, U.; Schreiner, M. *Applied Surface Science* **2007**, *253*, 3712-3721.

(57) Do, L. M. H., E. M.; Niidome, Y.; Fujihira, M.; Kanno, T.; Yoshida, S.; Maeda, A.; Ikushima, A. J.; *Journal of Applied Physics* **1994**, *76*, 5118 - 5121

(58) Ikemiya, N.; Kubo, T.; Hara, S. *Surface Science* **1995**, *323*, 81-90.

(59) Yamaguchi, Y.; Shiota, M.; Nakayama, Y.; Hirai, N.; Hara, S. *Journal of Power Sources* **2000**, *85*, 22-28.

(60) Mao, G.; Lobo, L.; Scaringe, R.; Ward, M. D. *Chemistry of Materials* **1997**, *9*, 773-783.

(61) Dove, P. M.; Platt, F. M. *Chemical Geology* **1996**, *127*, 331-338.

(62) Morita, S.; Komeda, T.; Tanaka, S.; Yamada, H. In *Roadmap of Scanning Probe Microscopy*; Springer Berlin Heidelberg: 2007, p 85-94.

(63) Joachim, J. K. G. a. C. *Science* **1999**, *283*, 1683-1688

(64) Ruiz-Agudo, E.; Putnis, C. V.; Jiménez-López, C.; Rodriguez-Navarro, C. *Geochimica et Cosmochimica Acta* **2009**, *73*, 3201-3217.

(65) Maurice, P. A.; Lower, S. K.; Donald, L. S. In *Advances in Agronomy*; Academic Press: 1997; Vol. Volume 62, p 1-43.

(66) Bose, S.; Hu, X.; Higgins, S. R. *Geochimica et Cosmochimica Acta* **2008**, *72*, 759-770.

(67) Bosbach, D.; Hall, C.; Putnis, A. *Chemical Geology* **1998**, *151*, 143-160.

(68) Maurice, P. A. *Colloids and Surfaces A: Physicochemical and Engineering Aspects* **1996**, *107*, 57-75.

(69) Tao, N. *Spectroscopic Applications of STM and AFM in Electrochemistry*; Wiley-VCH Verlag GmbH & Co. KGaA, 2007.

(70) Hamers, R. J. *Journal of Physical Chemistry* **1996**, *100*, 13103-13120.

(71) Jalili, N.; Laxminarayana, K. *Mechatronics* **2004**, *14*, 907-945.

(72) Li, H.; Mao, G.; Simon Ng, K. Y. *Thin Solid Films* **2000**, *358*, 62-72.

(73) Henderson, E. *Progress in Surface Science* **1994**, *46*, 39-60.

(74) Li, M. Q. *Scanning* **1999**, *68*, 255-258.

(75) Le Grimellec, C.; Lesniewska, E.; Cachia, C.; Schreiber, J. P.; de Fornel, F.; Goudonnet, J. P. *Biophysical journal* **1994**, *67*, 36-41.

(76) Le Grimellec, C.; Lesniewska, E.; Giocondi, M.-C.; Finot, E.; Vié, V.; Goudonnet, J.-P. *Biophysical journal* **1998**, *75*, 695-703.

(77) P Perfetti, A. C., R Generosi *Surface Review and Letters* **2000**, *7*, 411-422.

(78) You, H. X.; Yu, L. *Methods in Cell Science* **1999**, *21*, 1-17.

(79) *Atomic Force Microscopy in Cell Biology*; 1st ed.; Bhanu P. Jena, a. J. K. H. H., Ed.; Academic Press: San Diego, CA, 2002; Vol. 68.

(80) *Force Microscopy: Applications in Biology and Medicine*; Bhanu P. Jena, a. J. K. H. H., Ed.; John Wiley and Sons: New Jersey, 2006.

(81) Muller, D. J. *Biochemistry* **2008**, *47*, 7986-7998.

(82) Cai, X.; Yang, X.; Cai, J.; Wu, S.; Chen, Q. *The Journal of Physical Chemistry B* **2009**, *114*, 3833-3839.

(83) Sturgis, J. N.; Tucker, J. D.; Olsen, J. D.; Hunter, C. N.; Niederman, R. A. *Biochemistry* **2009**, *48*, 3679-3698.

(84) Braet; Seynaeve; De, Z.; Wisse *Journal of Microscopy* **1998**, *190*, 328-338.

(85) Carvalho, F. A.; Connell, S.; Miltenberger-Miltenyi, G.; Pereira, S. n. V.; Tavares, A.; Arielˆns, R. A. S.; Santos, N. C. *ACS Nano* **2010**, *4*, 4609-4620.

(86) Henderson, R. M.; Oberleithner, H. *American Journal of Physiology - Renal Physiology* **2000**, *278*, F689-F701.

(87) Wu, H. W.; Kuhn, T.; Moy, V. T. *Scanning* **1998**, *20*, 389-397.

(88) A-Hassan, E.; Heinz, W. F.; Antonik, M. D.; D Costa, N. P.; Nageswaran, S.; Schoenenberger, C.-A.; Hoh, J. H. *Biophysical journal* **1998**, *74*, 1564-1578.

(89) Hategan, A.; Law, R.; Kahn, S.; Discher, D. E. *Biophysical journal* **2003**, *85*, 2746-2759.

(90) Lekka, M.; Laidler, P.; Gil, D.; Lekki, J.; Stachura, Z.; Hrynkiewicz, A. Z. *European Biophysics Journal* **1999**, *28*, 312-316.

(91) Rotsch, C.; Radmacher, M. *Biophysical journal* **2000**, *78*, 520-535.

(92) Rotsch, C.; Braet, F.; Wisse, E.; Radmacher, M. *Cell Biology International* **1997**, *21*, 685-696.

(93) Radmacher, M.; Fritz, M.; Kacher, C. M.; Cleveland, J. P.; Hansma, P. K. *Biophysical journal* **1996**, *70*, 556-567.

(94) Radmacher, M.; Bhanu P. Jena, H. J. K. H. In *Methods in Cell Biology*; Academic Press: 2002; Vol. Volume 68, p 67-90.

(95) Ludwig, M.; Dettmann, W.; Gaub, H. E. *Biophysical journal* **1997**, *72*, 445-448.

(96) Fotiadis, D.; Scheuring, S.; Müller, S. A.; Engel, A.; Müller, D. J. *Micron* **2002**, *33*, 385-397.

(97) Stroh, C.; Wang, H.; Bash, R.; Ashcroft, B.; Nelson, J.; Gruber, H.; Lohr, D.; Lindsay, S. M.; Hinterdorfer, P. *Proceedings of the National Academy of Sciences of the United States of America* **2004**, *101*, 12503-12507.

(98) Hinterdorfer, P.; Dufrene, Y. F. *Nat Meth* **2006**, *3*, 347-355.

(99) Douglas Magde, E. E., and W. W. Webb *Physical Review Letters* **1972**, *29*, 705–708.

(100) Elliot L. Elson, D. M. *Biopolymers* **1974**, *13*, 1-27.

(101) Douglas Magde, E. L. E., Watt W.Webb *Biopolymers* **1974**, *13*, 29-61.

(102) Haustein, E.; Schwille, P. *Annual Review of Biophysics and Biomolecular Structure* **2007**, *36*, 151-169.

(103) Schwille, P.; Korlach, J.; Webb, W. W. *Cytometry* **1999**, *36*, 176-182.

(104) Schwille, P.; Haupts, U.; Maiti, S.; Webb, W. W. *Biophys. J.* **1999**, *77*, 2251-2265.

(105) Berland, K. M.; So, P. T. C.; Gratton, E. *Biophys. J.* **1995**, *68*, 694-701.

(106) Berland, K. M.; So, P. T. C.; Gratton, E. *Biophysical Journal* **1995**, *68*, 694-701.

(107) Zhao, M.; Jin, L.; Chen, B.; Ding, Y.; Ma, H.; Chen, D. *Appl. Opt.* **2003**, *42*, 4031-4036.

(108) Coates, P. B. *Journal of Physics D: Applied Physics* **1973**, *6*, 1159.

(109) Mukhopadhyay, A.; Bae, S. C.; Zhao, J.; Granick, S. *Phys. Rev. Lett.* **2004**, *93*, 236105.

(110) Mukhopadhyay, A.; Granick, S. *Current Opinion in Colloid & Interface Science* **2001**, *6*, 423-429.

(111) Oral, A.; Grimble, R. A.; Ozer, H. O.; Pethica, J. B. *Review of Scientific Instruments* **2003**, *74*, 3656-3663.

(112) Sudakar, C.; Kharel, P.; Suryanarayanan, R.; Thakur, J. S.; Naik, V. M.; Naik, R.; Lawes, G. *Journal of Magnetism and Magnetic Materials* **2008**, *320*, L31-L36.

(113) Sudakar, C.; Kharel, P.; Lawes, G.; Suryanarayanan, R.; Naik, R.; Naik, V. M. *Journal of Physics-Condensed Matter* **2007**, *19*, -.

(114) Skinner, J. P.; Chen, Y.; Müller, J. D. *Biophysical journal* **2005**, *89*, 1288-1301.

(115) Petersen, N. O. *Biophysical journal* **1986**, *49*, 809-815.

(116) Choi, S. U. S., and Eastman, J. A. In *ASME International Mechanical Engineering Congress and Exposition* San Francisco, CA., 1995.

(117) Sarita K. Das, S. U. S. C., Wenhua Yu, T. Pradeep *Nanofluids: Science and Technology*; John Wiley & Sons: Hoboken, NJ, 2008.

(118) Eastman, J. A., Choi, S. U. S., Li, S., Thompson, L. J., and Lee, S. In *Fall Meeting of the Materials Research Society* Boston, MA, 1996.

(119) Eastman, J. A., Choi, U. S., Li, S., Soyez, G., Thompson, L. J., and DiMelfi, R. J. *Mater. Sci. Forum* **1999**, *312-314*, 629-634.

(120) Eastman, J. A.; Choi, S. U. S.; Li, S.; Yu, W.; Thompson, L. J. *Appl. Phys. Lett.* **2001**, *78*, 718-720.

(121) Lee, S.; Choi, S. U. S.; Li, S.; Eastman, J. A. *J. Heat Trans-T ASME* **1999**, *121*, 280-289.

(122) Xuan, Y. M. *Heat Mass Transfer* **2009**, *46*, 277-279.

(123) Keblinski, P.; Phillpot, S. R.; Choi, S. U. S.; Eastman, J. A. *Int. J. Heat Mass Tran.* **2002**, *45*, 855-863.

(124) Eastman, J. A.; Phillpot, S. R.; Choi, S. U. S.; Keblinski, P. *Ann. Rev. Mater. Res* **2004**, *34*, 219-246.

(125) Krishnamurthy, S.; Lhattacharya, P.; Phelan, P. E.; Prasher, R. S. *Nano Lett.* **2006**, *6*, 419-423.

(126) Fang, X. P.; Xuan, Y. M.; Li, Q. *Appl. Phys. Lett.* **2009**, *95*, 203108.

(127) Turanov, A. N.; Tolmachev, Y. V. *Heat Mass Transfer* **2009**, *45*, 1583-1588.

(128) Bocquet, L.; Charlaix, E. *Chem. Soc. Rev.* **2010**, *39*, 1073-1095.

(129) Ozturk, S.; Hassan, Y. A.; Ugaz, V. M. *Nano Lett.* **2010**, *10*, 665-671.

(130) Gerardi, C. C., D. Buongiorno, J. Hu, L. W. *T. Am. Nucl. Soc.* **2007**, *96*, 485-486.

(131) E.L.Cussler *Diffusion: Mass Transfer in Fluid Systems*; Cambridge University Press: New York, NY, 1984.

(132) Einstein, A. *Investigations on the Theory of the Brownian Movement*; Dover Publications: New York, NY, 1956.

(133) J. N. Israelachvili *Intermolecular and Surface Forces*; 2nd ed.; Wiley: New York, 1990.

(134) Israelachvili, J. N.; Pashley, R. M. *Nature* **1983**, *306*, 249-250.

(135) Bunk, O.; Diaz, A.; Pfeiffer, F.; David, C.; Padeste, C.; Keymeulen, H.; Willmott, P. R.; Patterson, B. D.; Schmitt, B.; Satapathy, D. K.; van der Veen, J. F.; Guo, H.; Wegdam, G. H. *Physical Review E* **2007**, *75*, 021501.

(136) Nygard, K.; Satapathy, D. K.; Bunk, O.; Diaz, A.; Perret, E.; Buitenhuis, J.; Pfeiffer, F.; David, C.; van der Veen, F. *Opt. Express* **2008**, *16*, 20522-20529.

(137) Wiener, M. C.; White, S. H. *Biophysical journal* **1991**, *59*, 162-173.

(138) Das, S. K.; Sharma, M. M.; Schechter, R. S. *The Journal of Physical Chemistry* **1996**, *100*, 7122-7129.

(139) Gruhn, T.; Schoen, M. *Physical Review E* **1997**, *55*, 2861.

(140) Head-Gordon, T.; Hura, G. *Chemical Reviews* **2002**, *102*, 2651-2670.

(141) Gao, J. P.; Luedtke, W. D.; Landman, U. *J. Phys. Chem. B* **1997**, *101*, 4013-4023.

(142) Denis Morineau, R. G., Yongde Xia, and Christiane Alba-Simionesco *Journal of Chemical Physics* **2004**, *121*, 1466-1474.

(143) Löwen, H. *Journal of Physics: Condensed Matter Volume 21 Number 47* **2009**, *21*

(144) D. Babič, C. S., and C. Bechinger *Chaos* **2005**, *15*.

(145) Dieter M Herlach, I. K., Patrick Wette and Dirk Holland-Moritz *journal of physics: Condensed Matter* **2010**, *22*, 153101.

(146) Tata, B. V. R.; Boda, D.; ouml; Henderson, D.; Nikolov, A.; Wasan, D. T. *Physical Review E* **2000**, *62*, 3875.

(147) Trokhymchuk, A.; Henderson, D.; Nikolov, A.; Wasan, D. T. *Langmuir* **2005**, *21*, 10240-10250.

(148) Ohshima, H. *Theory of Colloid and Interfacial Electric Phenomena* Academic Press: Amsterdam, 2006; Vol. 12.

(149) Liang, Y.; Hilal, N.; Langston, P.; Starov, V. *Advances in Colloid and Interface Science* **2007**, *134-135*, 151-166.

(150) Han, Y.; Grier, D. G. *Physical Review Letters* **2003**, *91*, 038302.

(151) Grier, D. G. *Nature* **1998**, *393*, 621-623.

(152) Larsen, A. E.; Grier, D. G. *Nature* **1997**, *385*, 230-233.

(153) Linse, P.; Lobaskin, V. *Physical Review Letters* **1999**, *83*, 4208.

(154) Khan, S. H.; Matei, G.; Patil, S.; Hoffmann, P. M. *Phys. Rev. Lett.* **2010**, *105*, 106101.

(155) Khan, S. H., Wayne State University, 2010.

(156) Khan, S. H.; Matei, G.; Patil, S.; Hoffmann, P. M. *Physical Review Letters*, *105*, 106101.

(157) Mayyas, E.; Bernardo, M.; Runyan, L.; Sohail, A.; Subba-Rao, V.; Pantea, M.; Fridman, R.; Hoffmann, P. M. *Biomacromolecules*, *11*, 3352-3358.

ABSTRACT

A NOVEL INTEGRATED PLATFORM COMBINING ATOMIC FORCE MICROSCOPY AND FLUORESCENCE CORRELATION SPECTROSCOPY

by

VENKATESH SUBBA RAO

AUGUST 2011

Advisor: Prof. Peter M. Hoffmann

Major: Physics

Degree: Doctor of Philosophy

At the nanoscale near an interface, the discrete nature of liquids is expected to influence various properties, such as density, viscosity or diffusion constants. Understanding interfacial properties of liquids is important for the development of nanotechnology, especially for the fields of nano-rheology and nano-tribology, and also for understanding various mechanisms in biological systems at the molecular level, such as protein folding or the self-assembly of lipid vesicles, which invariably involve liquids. Atomic force microscope (AFM) and fluorescence correlation spectroscope (FCS) are two complimentary techniques that are commonly employed investigate mechanics and dynamics of liquids at interfaces. In this thesis, the design and construction of a novel integrated platform combining AFM and FCS is presented. The platform consists of a newly built high sensitive AFM on top of an existing custom-made FCS setup. The design is modular in nature, can be easily assembled or disassembled and thus both AFM and FCS can be used independently. The successful operation was the platform was demonstrated by employing a colloidal liquid as a test system. Results of

AFM experiments indicated the presence of structure to the colloidal dispersion under confinement, similar to the behavior of molecular liquids reported in the literature, at length scales of a few 10 nm. However, FCS results showed considerable decrease in the diffusion of colloidal particle even when the confinement was of the order of microns. The design, construction and the testing of the new platform along with the intriguing results will be presented.

AUTOBIOGRAPHICAL STATEMENT

Venkatesh Subba Rao

Education:

- 2006-2011, PhD (Physics), Wayne State University, Detroit, MI.
- 2000-2006, MS (Physics), Clarkson University, Potsdam, NY.
- 1996-1998, MSc (Physics), The American College, Madurai, India.
- 1993-1996, BSc (Special Physics), The American College, Madurai, India.

Fellowships and Honors:

- **WSU-Physics Knoller Endowment Fellowship**, WSU, Winter 2011
- **Competitive Thomas C. Rumble Fellowship,** WSU, 2009-2010
- **Summer Dissertation Fellowship,** WSU, 2009
- Recipient of prestigious **Thomas C. Rumble Fellowship,** WSU, 2006-2007
- **Outstanding Teaching Assistant Award**, American Association of Physics Teachers, 2006
- **Commendable Service Award** for teaching, given by Phalanx Senior Honorary Leadership Society at Clarkson University, 2005

Recent Publications:

- Mayyas, E., Bernardo, M., Runyan, L., Sohail, A., **Subba-Rao, V.,** Pantea, M., Fridman, R., Hoffmann, P. M.," Dissociation Kinetics of an Enzyme-Inhibitor System Using Single-Molecule Force Measurements", ***Biomacromolecules,*** 11, 3352, **2010**
- **Venkatesh Subba-Rao,** Chandran Sudakar, Jason Esmacher, Mircea Pantea, Ratna Naik and Peter M. Hoffmann, "Improving a high-resolution fiber optic interferometer by simple dip coating of TiO_2 at the end of fiber", ***Review Scientific Instruments***, **80,** 115104, **2009**
- Iyer, S., R.M. Gaikwad, **V. Subba-Rao**, C.D. Woodworth, and I. Sokolov, "AFM Detects Differences in the Surface Brush on Normal and Cancerous Cervical Cells", ***Nature Nanotechnology***, 4, pp 389-393, **2009**
- Igor Sokolov, Swaminathan Iyer, **Venkatesh Subba-Rao,** Ravi M. Gaikwad and Craig D. Woodworth, "Detection of surface brush on biological cells *in vitro* with atomic force microscopy", ***Applied Physics Letters***, 91, pp 023902, , **2007**
- Igor Sokolov, **Venkatesh Subba-Rao**, and Linda A. Luck, "Change in Rigidity in the Activated Form of the Glucose/Galactose Receptor from E.coli: A phenomenon that will be key to the development of Biosensors," ***Biophysical Journal***, 90, pp 1-9, **2006.**